

ABSTRACT

SMITH, JAMES EDISON. Lab in a Brick: an Unobtrusive Unattended Sensor for Urban Environments. (Under the direction of Prof. John F. Muth, PhD).

An unobtrusive environmental monitoring platform is developed utilizing commercial off-the-shelf components combining power generation, energy storage, gas and particle sensing, and wireless communication. Solar and thermal power generation schemes are compared, and battery and supercapacitor energy storage mediums are combined. Energy use is evaluated on a per sensing event basis. Emphasis is placed on environmental sensing for contaminants detrimental to health. Conclusions are drawn regarding possible deployment of arrays of sensors and further research areas concerning individual health monitoring are proposed.

© Copyright 2014 by James Edison Smith, Jr.

All Rights Reserved

Lab in a Brick: an Unobtrusive Unattended Sensor for Urban Environments

by
James Edison Smith, Jr.

A thesis submitted to the Graduate Faculty of
North Carolina State University
in partial fulfillment of the
requirements for the degree of
Master of Science

Electrical Engineering

Raleigh, North Carolina

2014

APPROVED BY:

John F. Muth, PhD
Committee Chair

Veena Misra, PhD

Edward Grant, PhD

DEDICATION

I dedicate this thesis to my wife, Michelle. Without you, I would have depleted what little sanity I have left long ago. You kept on moving forward no matter what, and encouraged me to do the same.

For you, I am forever grateful.

BIOGRAPHY

LT James E. Smith, Jr., CEC, USN, was born in Huntsville, Alabama. He attended high school in the tiny town of Laurel Hill, Florida, as one of thirty in his graduating class. He began his naval career immediately after high school by accepting an appointment to the United States Naval Academy as part of the class of 2004. While at the academy, he majored in Electrical Engineering, with an emphasis in computer engineering. Following graduation and commissioning, Ensign Smith began NFO flight training but soon lateral transferred to the Civil Engineer Corps. His jobs have included:

Assistant Public Works Officer at Marine Corps Air Station, Beaufort, South Carolina

Assistant Officer in Charge of the US Army Corps of Engineers camp at Forward Operating Base Loyalty in Baghdad, Iraq

Officer in Charge of Detail Dwyer, Assistant Operations Officer, and both Bravo and Charlie Company Commanders for Naval Mobile Construction Battalion 74 in Gulfport, Mississippi; Camp Dwyer, Helmand Province, Afghanistan; and Camp Mitchell, Naval Station Rota, Spain.

LT Smith is currently an instructor in the Electrical and Computer Engineering Department at the US Naval Academy in Annapolis, Maryland.

ACKNOWLEDGMENTS

First and foremost, I would like to thank Dr. Muth for taking me on as an advisee. I'm sure you regret that now, but I am in your debt. Your constant optimism and guidance to just keep moving forward are the two primary driving forces that allowed this thesis to be constructed.

TABLE OF CONTENTS

LIST OF TABLES	vi
LIST OF FIGURES	viii
Chapter 1 – Introduction	1
1.1 Goals.....	1
1.2 Description and Overview of the System.....	5
Chapter 2 – Literature Review	20
2.1 Overview	20
2.3 Air Quality Sensors	29
2.4 Energy Harvesting & Storage	46
Chapter 3 – Experimental Procedure	65
3.1 Component Selection and Testing.....	67
3.2 Wireless Data Transmission.....	69
3.3 Energy Storage	71
3.4 Energy Harvesting.....	75
3.5 Sensors	98
3.6 Experimental Procedure and Assembly	104
3.7 Coding.....	106
Chapter 4 – Conclusions	107
Chapter 5 – Future Research.....	110
REFERENCES	112
APPENDIX.....	118
Appendix A – End Device Source Code.....	119

LIST OF TABLES

Table 1- Thermal resistance and thermal conductivity data for extruded house bricks (230x110x76mm) [12].	8
Table 2- Thermal resistance and thermal conductivity data for pressed house bricks (230x110x76mm) [12].	8
Table 3- National Ambient Air Quality Standards (NAAQS) table of pollutants and allowable maximum levels as of October 2011 [28].	30
Table 4- Commercial gas sensors with varying heater voltages, costs, and selectivity. Energy requirements are approximated based on minimum listed settling times. Information compiled from publicly available datasheets.	31
Table 5- Commercially available dust and particle counters. ¹ Requires additional 18" vacuum source.	42
Table 6- Comparison of currently available bulk Bismuth Telluride Thermoelectric Generators listing the surface area of one side, power output at various temperature differentials, cost, power per unit area, cost per power, and power per unit area per temperature differential. All data gathered from datasheets.	52
Table 7- Comparison of currently available Thermoelectric Generators built from a superlattice of Bismuth Telluride and Antimony Telluride listing the surface area of one side, power output at various temperature differentials, cost, power per unit area, cost per power, and power per unit area per temperature differential. All data gathered from datasheets.	53
Table 8 - Solar Radiation for Flat-Plate Collectors Facing South at a Fixed Tilt (kWh/m ² /day), Uncertainty ±9%. [16]	77
Table 9 – Monthly average, minimum, and maximum energy produced per day by the CBC-PV-01 in Raleigh, NC, when placed vertically and facing south in Wh/day and kJ/day.	78
Table 10 - Listing of the Specific Thermal Resistances for each of the elements in series with the 40mmx40mm CustomThermoelectric TEGs. Component values were taken from datasheets where available and measured or approximated when necessary.	87
Table 11 - Listing of the Specific Thermal Resistances for each of the elements in series with the 2mmx2mm HV37 TEGs from Nextreme. Component values were taken from datasheets where available and measured or approximated when necessary.	87

Table 12 - List of sensors, minimum and maximum sensing resistances, and load resistors
chosen to maximize the voltage swing as gas concentration changes.101

LIST OF FIGURES

- Figure 1- 2005 NATA Estimated Tract Level Total Respiratory Hazard Index [2]. Data from sensors placed throughout the country are combined to create broad hazard maps such as this. Overall sensor coverage is high, but density is low. These hazard maps are useful for determining the statistical likelihood of a population experiencing health effects, but very little correlation can be drawn between respiratory irritants and individual's response.2
- Figure 2- "Lab in a Brick" Functional Block Diagram showing two energy scavenging sources, solar and thermal, a Texas Instruments ultralow power controller with integrated radio. A variety of sensors can be powered by the sensor voltage banks, with sensor input digitized by the ADC inputs of the microcontroller or serial input of the microcontroller depending on the sensor type.6
- Figure 3- Effective thermal conductivity for composites and bricks as a function of porosity [13].9
- Figure 4- Experimental data of the thermal conductivity of adobe bricks as a function of porosity and materials used [14].9
- Figure 5- Thermal conductivity versus bulk density values for various clay bricks [10].10
- Figure 6- Calculated instant thermal conductivity for a 110mm brick layer using the finite volume method in December, 2003 on the campus of the University of Newcastle [15].10
- Figure 7- Solar Radiation for Flat-Plate Collectors Facing South at a Fixed Tilt ($\text{kWh/m}^2/\text{day}$) [16]. The station for these measurements was located in Raleigh, NC.12
- Figure 8- Insulated Cavity Brick Summer Cycle Temperature Profile [18]. The wall was constructed with internal and external brickwork separated by a polystyrene foam sheet and an air cavity.13
- Figure 9- Comparative presentation of the calculated heat fluxes for the lightweight panel WB1 (solid line 1) and the progressively heavier brick walls WB2 to WB6 (solid lines 2–6), for a succession of five sequential winter days. In the same plot, the harmonically varying ambient temperature and the time varying solar insolation are also shown with broken and dotted lines, respectively [17].13
- Figure 10- Comparative presentation of the calculated heat fluxes for the lightweight panel WB1 (solid line 1) and the progressively heavier brick walls WB2 to WB6 (solid lines 2–6), for a succession of five sequential summer days. In the same

plot, the harmonically varying ambient temperature and the time varying solar insolation are also shown with broken and dotted lines, respectively [17].	14
Figure 11- Paired with Figure 12, a resistor network representative of the thermal resistances present in a modern wood or metal frame wall with exterior brick veneer in a configuration in which the internal wall and vapor barrier remain intact. This configuration does not exploit the temperature sink internal to the building.	16
Figure 12- Paired with Figure 11, a vertical slice of a modern wood or metal frame wall with exterior brick veneer in a configuration in which the internal wall and vapor barrier remain intact. This configuration does not exploit the temperature sink internal to the building.	16
Figure 13- Paired with Figure 14, a resistor network representative of the thermal resistances present in a modern wood or metal frame wall with exterior brick veneer in a configuration in which the thermal short pierces the interior wall and vapor barrier. This configuration best exploits the temperature sink internal to the building.	17
Figure 14- Paired with Figure 13, a vertical slice of a modern wood or metal frame wall with exterior brick veneer in a configuration in which the thermal short pierces the interior wall and vapor barrier. This configuration best exploits the temperature sink internal to the building.	17
Figure 15- Millbrook NCore Monitoring Site [6].	22
Figure 16- Aeroqual AQM 60 Air Quality Station [4].	23
Figure 17- Indoor Air Quality transceiver implementing sensors for dust, VOC, humidity, temperature, and CO ₂ , and a ZigBee radio [25].	25
Figure 18- Wearable VOC sensor. (A) Sensor components, and pictures. It shows a person wearing the detection unit near the breathing zone while holding the phone that acts as user interface, as well as a view of both VOC sensor components. (B) User interface on the phone, displaying the data received from the monitor. (C) Robustness test: the plot shows the sensor response (at 1-Hz data resolution) during x-, y-, and z- acceleration events detected with an accelerometer attached to the VOC sensor [3].	26
Figure 19- Structure of the integrated multi-body sensor platform [26].	27
Figure 20- Prototype multi-body sensor platform [26].	28

Figure 21- Schematic diagram of the integrated self-powered system. a) An integrated system can be divided into five modules: energy harvester, energy storage, sensors, data processor & controller, and data transmitter & receiver. b) Prototype of an integrated self-powered system using a nanogenerator as the energy harvester [27].	29
Figure 22- Comparison of various sensing methods outlining their approximate power requirements versus functionality.	36
Figure 23- (A) The change in sensor resistances upon the exposure of different concentrations of NO _x , (B) and sensor response as a function of gas concentration [29].	37
Figure 24 - Carbon monoxide thin-film micro hot wire sensor in a. showing two parallel sensors consisting of a combination heater and sensor electrode in series with a load resistor. A blowup of the heater element in b. shows the thin-film metal-oxide gas sensitive layer applied across the top of the heater, with a partial cross-section and finer detail in c. D. shows the additional platinum catalyst beads added to the top of the metal oxide layer [30].	38
Figure 25- Shift in absorbed frequency from 520nm as a function of ozone concentration for 25nm gold nanoislands [33].	40
Figure 26- (A) Response of BP-MIP modified tuning fork to 40 ppmv toluene in air. Flow rate: 250 mL min ⁻¹ . (B) Mass normalized response and reciprocal of response for tuning forks modified with different polymers. Sample: 40ppmv toluene. Flow rate: 250mL/min. [34]	41
Figure 27- A comparison of three optical particle counters comparing counting efficiency (defined as the number of particles counted divided by the true number of particles passing through the sensing chamber) [35]. For the A10, two flow rates were tested.	43
Figure 28- A comparison of the Welas 2100 and Welas 2100 Digital (Promo) showing improvements in counting efficiency and a lower minimum particle diameter threshold [36].	44
Figure 29- Comparative graph of two sensors: the Airbot research prototype and a commercial HHPC-6 from MET ONE. For the Airbot, specific particulate counts are shown (top) as well as the integrated total (middle). For the HHPC-6, the output (bottom) is used to validate the Airbot's integrated graph and provide a laboratory-grade baseline. [37]	45
Figure 30 - Chart displaying the various types of photovoltaic technologies, peak research-cell efficiencies, responsible group, and date of achievement [38].	47

Figure 31 - Basic layout of a Thermoelectric Generator demonstrating the physical layout of n- and p-type legs placed between a heat source and heat sink with current flowing from the n-type leg to the p-type leg. [Enhancement of the].....	50
Figure 32- Comparison of figure of merit, ZT, for various temperatures and multiple thermoelectric materials. [42]	50
Figure 33 - Illustration of the principle of a TPV system in which a heated emitter creates photons that the photocell converts into electrical power. An optional filter removes photons that would otherwise be converted to heat in the photocell. [46]....	55
Figure 34 - A schematic representation of a solar powered thermionic electron source. The forest of nanotubes was grown on a highly doped silicon wafer and placed below a simple metallic anode. Focused sunlight directed at the side of the nanotube forest provided heating, which was further concentrated by the “heat island” effect of the nanotubes themselves. [47]	56
Figure 35 - Block diagrams representative of modern energy harvesting systems. The MPPT and battery management unit are left out of (a), with the diode serving as the simplest form of an energy extractor. With (b) and (c), various energy storage mediums can be tested allowing for simple comparison and evaluation. [48]	58
Figure 36 - CBC-EVAL-09 Energy Harvester block diagram. Five separate inputs are provided: DC in for a photovoltaic source, AC in for an electromagnetic or radio frequency source, HV DC in for a thermoelectric source, and two HV AC ins for piezoelectric or vibration sources. [49].....	59
Figure 37 - Circuit diagram for a simple supercapacitor charger. When SW1 and SW2 are closed, current through L increases, storing energy. When SW1 and SW2 open, D1 and D2 begin to conduct, charging the supercapacitor. [60].....	63
Figure 38 - Graph comparing the total number of charge and discharge cycles a Li-ion battery can be expected to be subjected to when combined with a supercapacitor of a certain size. Given the maximum number of cycles for a battery and the designed lifetime for this system, a supercapacitor can be chosen. [48]	64
Figure 39 - Oscilloscope display showing the voltage across a 1.067 Ω resistor placed in series with the eZ430 while transmitting a sample data set.....	70
Figure 40 – Representative comparison of Sensor Resistance versus time with 3V, 2V, and 1.35V across the heating element for the MQ-4 (Carbon Monoxide) sensor.	73
Figure 41 - Picture of the benchtop setup used to test the efficiency of the CBC-PV-01 solar panel. The panel is placed in series with a variable resistor box to allow for	

changing the load in order to track the non-linear current-voltage curve. A smartphone is used as a light meter to determine incident radiation.	79
Figure 42 - Graph of panel efficiency versus output voltage for the CBC-PV-01 for three desktop lux values (4.7 lux, 187 lux, and 315 lux).	80
Figure 43 – Expected hourly energy output through a day from the CBC-PV-01 oriented vertically and facing south in Raleigh, NC, for January through June.	82
Figure 44 - Expected hourly energy output through a day from the CBC-PV-01 oriented vertically and facing south in Raleigh, NC, for July through December.	82
Figure 45 - Picture of the benchtop testing setup used to validate the TEG datasheet values. The TEGs were sandwiched between a large copper heatsink and a hotplate with thermistors attached via PGS to both sides of the TEGs for the most accurate temperature readings. Voltage across the TEGs and current through a series potentiometer measurements were taken to determine power output.	88
Figure 46 - Graph of measured voltage and current at various load resistances for the 40mmx40mm TEG at 5°C and 10°C ΔT	89
Figure 47 - Graph of measured voltage and calculated power at various load resistances for the 40mmx40mm TEG at 5°C and 10°C ΔT	90
Figure 48 - Graph of measured voltage and current at various load resistances for the HV37 TEG at 5°C, 10°C, and 15°C ΔT	90
Figure 49 - Graph of measured voltage and calculated power at various load resistances for the HV37 TEG at 5°C, 10°C, and 15°C ΔT	91
Figure 50 - Experimental setup to test the real-world power generation available from the CBC-PV-01 solar module, 40mmx40mm TEGs, and HV37 TEGs.	92
Figure 51 - Experimentally measured current versus voltage plot for the CBC-PV-01 in real-world, bright sun conditions.	93
Figure 52 - Experimentally measured voltage and calculated power plot for the CBC-PV-01 in real-world, bright sun conditions.	93
Figure 53 - Experimentally measured current versus voltage plot for the 40mmx40mm TEG in real-world, bright sun conditions both with and without the Metal Velvet anti-reflective coating.	94

Figure 54 - Experimentally measured voltage and calculated power plot for the 40mmx40mm TEG in real-world, bright sun conditions both with and without the Metal Velvet anti-reflective coating.94

Figure 55 - Experimentally measured current versus voltage plot for the 2mmx2mm HV37 TEG with CPC in real-world, bright sun conditions both with and without the Metal Velvet anti-reflective coating.95

Figure 56 - Experimentally measured voltage and calculated power plot for the 2mmx2mm HV37 TEG with CPC in real-world, bright sun conditions both with and without the Metal Velvet anti-reflective coating.95

Figure 57 - Measured response from the MQ-4 sensor with varying heater voltages.100

Chapter 1 – Introduction

1.1 Goals

The goal of this project is to combine environmental sensing, energy generation, and wireless data transmission into a self-contained device within a brick form factor that can be placed in an urban environment. Through the mass deployment of such a device, measurements of gasses and particulates that impact human health could be accomplished with a physical resolution currently unavailable. To develop the device, a systems approach was used that included:

- Energy harvesters provide power through solar and thermal generation schemes.
- High efficiency boost converters condition the raw power and charged thin-film batteries and supercapacitors.
- Gas sensors and a dust counter periodically monitor atmospheric conditions.
- A low power microcontroller gathers the sensor readings and stores them for transmission.
- A low power radio relays the data to a microcomputer for display and interpretation.

The driving force behind this project was a desire to more precisely understand the world we live in and how the air we breathe affects our health. By having a small device that can be deployed cheaply and widely, a better understanding of how air quality varies throughout an urban environment can be obtained. Studies have been conducted investigating the effects of some gasses and particulates on individuals, but these have usually centered on laboratory analyses [1] or the EPA's single point monitoring stations [2]. Personal wearable environmental monitors are an active research area, but are limited [3].

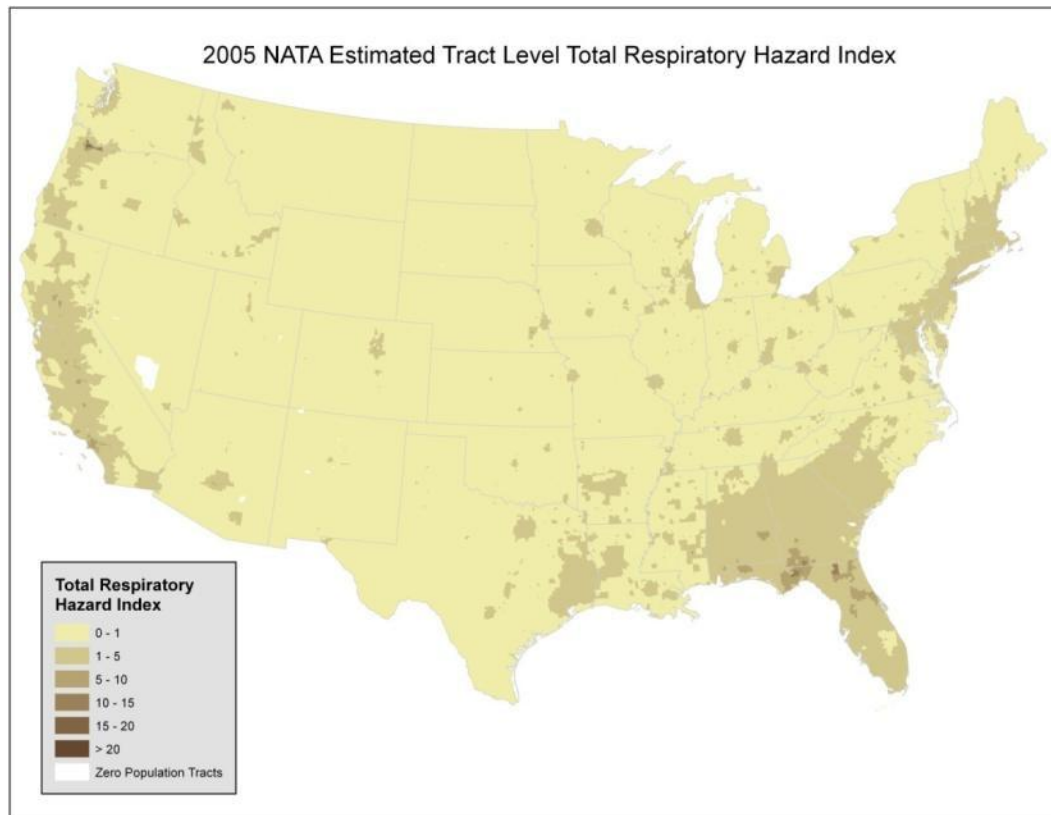


Figure 1- 2005 NATA Estimated Tract Level Total Respiratory Hazard Index [2]. Data from sensors placed throughout the country are combined to create broad hazard maps such as this. Overall sensor coverage is high, but density is low. These hazard maps are useful for determining the statistical likelihood of a population experiencing health effects, but very little correlation can be drawn between respiratory irritants and individual's response.

Current monitoring stations are large; expensive; and require grid electrical connections, constant maintenance, and calibration. As such, stations are limited in number and located in and around population centers [4]. Extensive modeling is required to predict the air quality between stations. Not only is the usefulness of the model results limited to basic statistical likelihoods in regards to determining health effects for an individual, the low sensor density completely overlooks significant amounts of data.

Advances in energy storage, increasing computational power per watt, and better sensors themselves, are slowly improving air quality systems. A few products have reached the market capable of being utilized wirelessly outside of a laboratory setting, but even these devices have limitations in their ability to sense multiple gasses and be deployed remotely. Also, the hobbyist and maker communities have recognized the current system shortfalls, and development is ongoing for distributed air quality and radiation sensors that collate their information via the internet [5].

This project was designed specifically to address the space sampling shortcomings of large expensive air quality monitoring stations. System attributes are to:

- Create a new platform for the detection of various gasses and particulates.
- Require little or no maintenance or user interaction (except data retrieval).
- Be able to be distributed in real-world locations outside of the laboratory.

The advantages of the “Lab in a Brick” platform include its compatibility with existing urban structures, low maintenance, and its ability to monitor its environment at regular intervals potentially for decades. Interfacing with existing urban structures is vital to the real-world use of any distributed platform. Given the ubiquitous nature of bricks in

modern construction, choosing this as the sensor housing ensured the maximum interoperability with existing buildings. Whereas current atmospheric sensor platforms targeting gasses impingent upon human health exist as a few per city and are located in out of the way places, such as 60 for the entire state of North Carolina [6], a sensor in a brick can be placed at the rate of a few per city block literally in the buildings in which people live, shop, and work.

Deploying large numbers of these sensors potentially allows for the tracking of gasses and particulates at a spatial resolution never before imagined. However, most particulate sensors require periodic filter changes, and almost every remote sensor currently requires battery replacement. While increasing the number of sensors improves the data's location resolution, maintenance could quickly become prohibitive. This project tries to reduce the need for any replacement parts. Incorporating internal power generation, duty cycling, maintenance free components, and wireless data transmission, this project anticipates that sensor platforms with an effective lifetime on the same order as the expected lifetimes of many newly constructed buildings can be achieved.

Multiple technological trends have converged to allow for the development of this sensor platform. Increases in computational power per watt and reductions in physical size have put the equivalent of a 1980 microcomputer into a chip smaller than a dime. Radio bandwidth has increased and antenna dimensions have decreased, drastically reducing the power necessary to transmit data. Advancements in supercapacitors have put hundreds of Farads in the physical size of a standard C battery. Environmental sensing benefited from many of the same improvements gained through chip manufacturing and energy storage –

namely miniaturization and a greater understanding of electro-chemical reactions – and with aggressive duty cycling has produced commercial sensors small and efficient enough to fit within this project’s size restraints and power budget. The most important piece of the puzzle has been power generation and energy harvesting. Photovoltaic electricity generation currently sits at around 12% efficient for whole systems [7]. Recent advancements in thermoelectric generation have placed this scheme on a comparable scale to solar when including the relatively consistent thermal gradient provided across a building’s brick wall and the ability to generate energy without direct lighting [8]. Both power generation schemes are investigated to see if a system that exploits the benefits of both, namely relatively efficient daytime energy production and small but appreciable evening and night production can be built.

1.2 Description and Overview of the System

A block diagram is provided by dividing the project into functional areas. The sensor platform is composed of one clay brick as the exterior veneer and thermal insulation, a solar panel, four thermoelectric generators, energy harvesting and control circuitry, energy storage, a high-efficiency boost converter, gas and particulate sensors, a microcontroller with attached radio, and a base station.

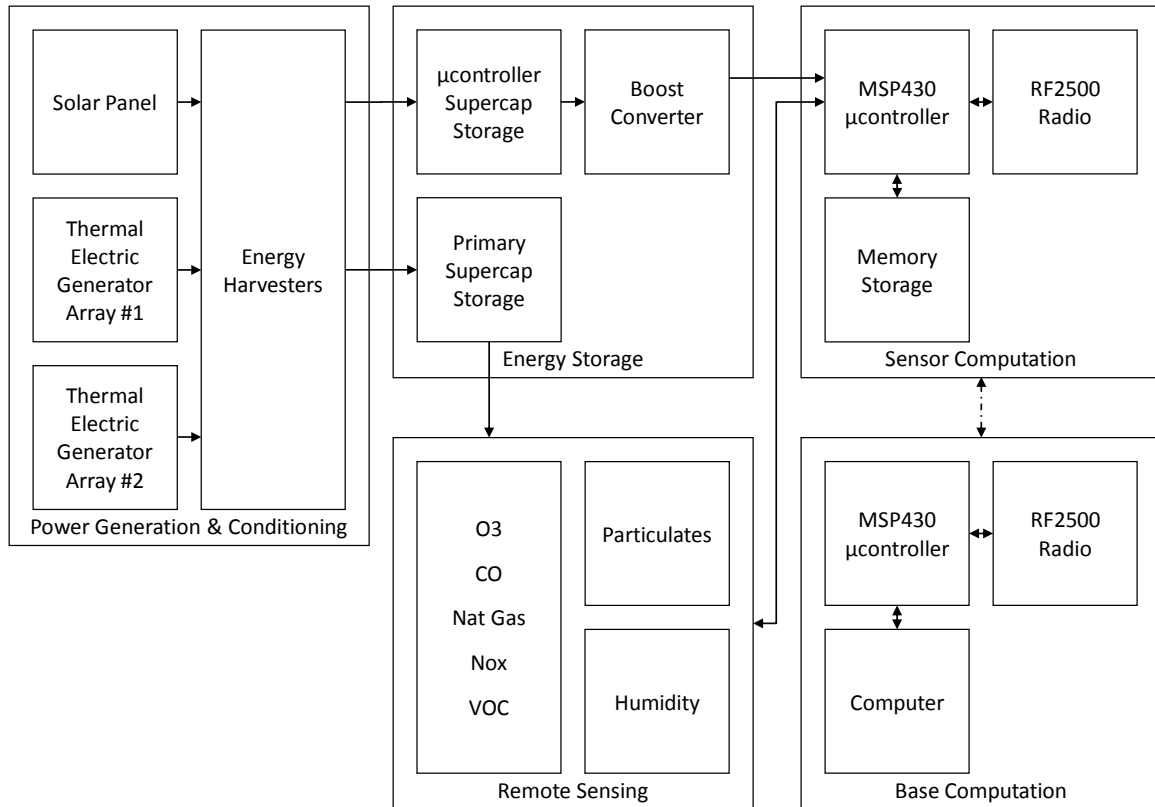


Figure 2- "Lab in a Brick" Functional Block Diagram showing two energy scavenging sources, solar and thermal, a Texas Instruments ultralow power controller with integrated radio. A variety of sensors can be powered by the sensor voltage banks, with sensor input digitized by the ADC inputs of the microcontroller or serial input of the microcontroller depending on the sensor type.

The most limiting stipulations set for this project were to incorporate the entire sensor platform within a US construction brick as well as to make use of the thermal gradient across a brick-veneered exterior wall. A quick study of bricks, in general, was performed to baseline the types, sizes, and thermal properties. In addition to construction bricks, there are a wide variety of bricks available for numerous uses: firebox brick, chemical resistant brick, sewer and manhole brick, and industrial floor bricks which were not considered, but suggest

other special applications where sensor bricks could potentially be used. Sizes for each of these bricks are not absolutely set, and are instead defined by the customer. Based on locally available bricks, an average size of 7.5"x3.5"x2.25" was chosen. The ASTM standards for construction bricks are described by the Brick Industry Association's document, "Technical Notes on Brick Construction," bulletin 9A [9]. Examining these standards provides physical parameters that a production version of the Lab-in-a-Brick will need to meet. For example, the compressive strength for an individual solid brick ranges from 1250 psi to 2500 psi and for a hollow brick ranges from 2200 to 2500 depending on the grade and weathering requirements for the brick.

The thermal conductivity, diffusivity, and heat capacity of brick are not specified by the standards, although building codes may specify R or U values to achieve a specified insulation value for the building envelope. Examining the literature, there are a wide range of thermal properties reported for bricks with several papers pointing out the relationship between density, porosity, water content, and the thermal properties [10, 11]. Nominally, one finds that depending on the type of brick, the thermal conductivity ranges between 0.1 W/mK for a very porous dry brick to slightly over 1 W/mK. As an example, consider the data from the Austral Brick Company, reproduced here in Table 1 and Table 2.

Table 1- Thermal resistance and thermal conductivity data for extruded house bricks (230x110x76mm) [12].

Brick Weight (kg)	Thermal Resistance R (m ² .K/W)	Thermal Conductivity k (W/m.K)
2.4	0.330	0.33
2.6	0.282	0.39
2.8	0.244	0.45
3.0	0.216	0.51
3.2	0.188	0.59
3.4	0.164	0.67
3.6	0.144	0.76
3.8	0.127	0.87
4.0	0.112	0.98

Table 2- Thermal resistance and thermal conductivity data for pressed house bricks (230x110x76mm) [12].

Brick Weight (kg)	Thermal Resistance R (m ² .K/W)	Thermal Conductivity k (W/m.K)
3.8	0.127	0.87
4.0	0.112	0.98
4.2	0.100	1.10

In general, studies in which the thermal coefficients are investigated as a function of material properties show correlations of thermal conductivity with density and porosity. Specifically as density increases or porosity decreases, conductivity increases.

As an example in the spread of data one can obtain when trying to calculate the thermal conductivity through a wall, consider Figure 6 which shows the thermal conductivity decreasing slowly over a about a month, likely due to a change in water content. This figure also illustrates the fact that measuring thermal conductivity can be challenging due to varying direct and indirect radiation, air temperature, wind speed, humidity, and other conditions.

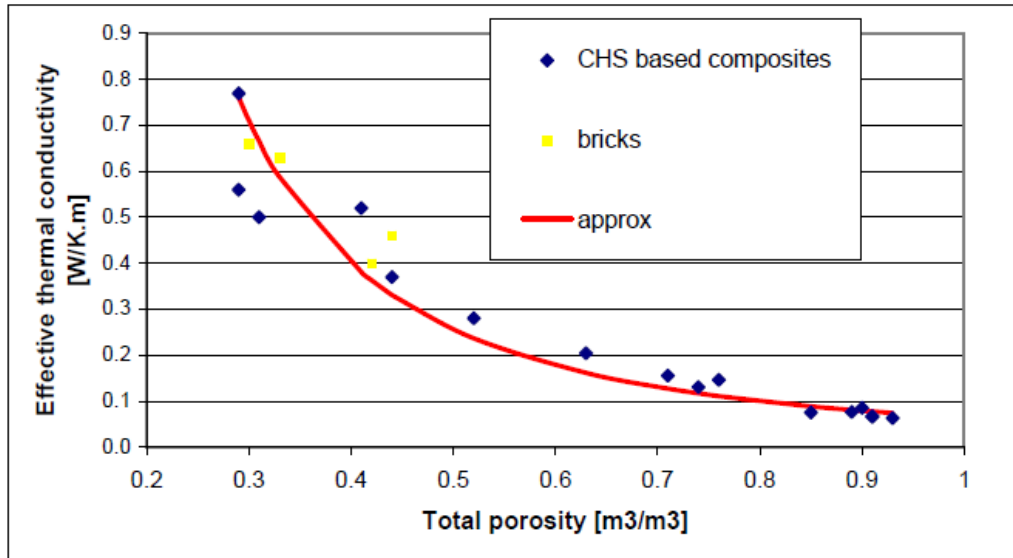


Figure 3- Effective thermal conductivity for composites and bricks as a function of porosity [13].

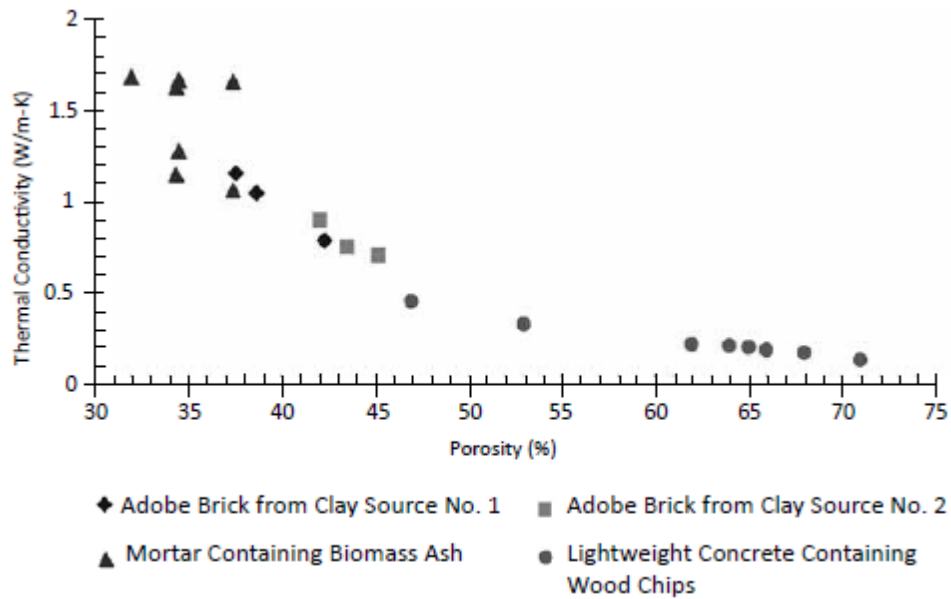


Figure 4- Experimental data of the thermal conductivity of adobe bricks as a function of porosity and materials used [14].

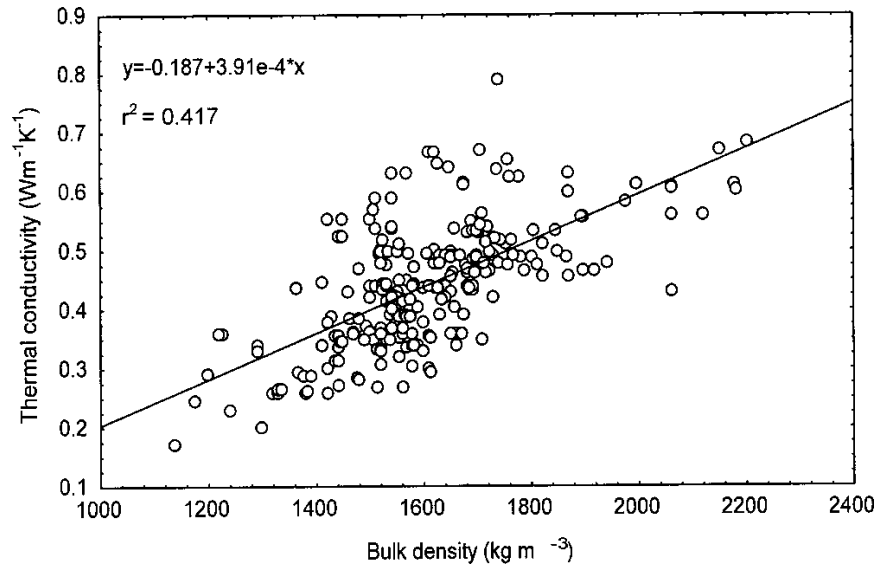


Figure 5- Thermal conductivity versus bulk density values for various clay bricks [10].

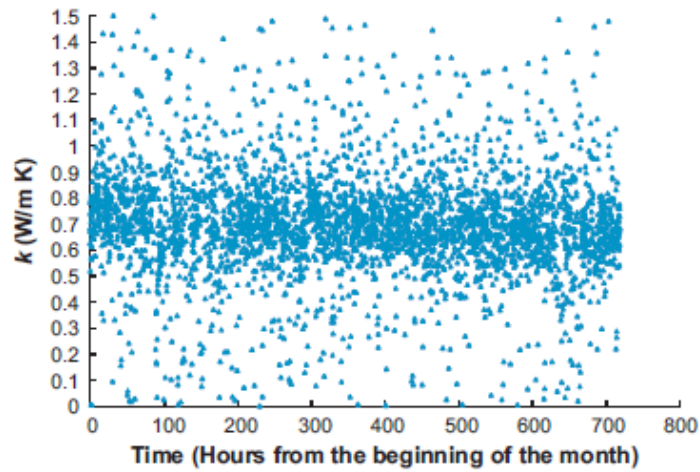


Figure 6- Calculated instant thermal conductivity for a 110mm brick layer using the finite volume method in December, 2003 on the campus of the University of Newcastle [15].

A production lab-in-a-brick will need to be tailored for the specific application, with dimensions, strength, and conductivity similar to the specific surrounding bricks. However for an initial demonstration, rather than molding and firing special hollow bricks, a hollow red clay brick was sliced to create $\frac{1}{4}$ " thick sheets which were then used as a veneer for the sensor platform. An additional 0.08" thick acrylic layer was incorporated to act as a vapor barrier, resulting in a void with interior dimensions of 6.84" x 2.84" x 1.59" in which all of the circuitry, energy storage mediums, and sensors must fit. For comparison, the final interior volume of 31 cubic inches was just over half the brick's initial 59 cubic inches.

The next major considerations were the limited area and temperature delta that are available for energy harvesting. The most prolific energy source for any sensor platform measuring the environment is the sun. Many simple procedures have already been developed by the solar power industry to approximate the amount of energy available per area at a given location. The National Renewable Energy Laboratory provides average insolation values throughout the year for various locations across the United States in kWh/m²/day [16]. Effects of north-south orientation, tilt, and one or two axis sun tracking can be approximated, however tracking schemes have been ignored for this project due to their need for additional mechanical hardware. Approximating temperature deltas across walls is more complicated.

For the vertical side of a brick on a south-facing wall, the maximum average energy available per day was 3.8kWh/m², and the minimum average was 2.3kWh/m². As a rule of thumb, 10% of this could be extracted, resulting in 380Wh/m² and 230Wh/m². The solar panel incorporated into this design was 2.25" x 2.25" and was expected to produce from 1.24Wh to 0.75Wh per day.

Tilt (°)		Jan	Feb	Mar	Apr	May	June	July	Aug	Sept	Oct	Nov	Dec	Year
0	Average	2.4	3.2	4.4	5.5	6.0	6.3	6.1	5.5	4.6	3.8	2.7	2.2	4.4
	Min/Max	2.0/2.8	2.5/3.8	3.6/5.1	4.8/6.4	5.1/6.6	5.7/7.1	5.2/6.8	4.3/6.1	3.8/5.3	3.2/4.4	2.0/3.0	1.6/2.6	4.0/4.6
Latitude -15	Average	3.4	4.1	5.0	5.8	6.0	6.2	6.0	5.7	5.1	4.6	3.7	3.1	4.9
	Min/Max	2.6/4.1	3.1/5.0	4.0/6.0	5.1/6.9	5.1/6.6	5.5/6.9	5.1/6.7	4.5/6.3	4.1/6.0	3.7/5.6	2.5/4.3	2.1/4.0	4.5/5.1
Latitude	Average	3.8	4.5	5.2	5.7	5.7	5.7	5.6	5.5	5.2	4.9	4.1	3.6	5.0
	Min/Max	2.8/4.8	3.3/5.6	4.1/6.2	5.0/6.8	4.8/6.2	5.1/6.4	4.7/6.2	4.3/6.1	4.1/6.1	3.9/6.0	2.7/4.8	2.3/4.6	4.5/5.2
Latitude +15	Average	4.1	4.6	5.1	5.3	5.0	4.9	4.9	5.0	5.0	5.0	4.3	3.8	4.8
	Min/Max	2.9/5.2	3.4/5.8	3.9/6.1	4.6/6.3	4.3/5.5	4.5/5.5	4.2/5.5	3.9/5.6	3.9/5.9	3.8/6.1	2.8/5.2	2.3/5.1	4.3/5.0
90	Average	3.6	3.8	3.6	3.1	2.5	2.3	2.4	2.8	3.3	3.8	3.7	3.5	3.2
	Min/Max	2.5/4.7	2.8/4.8	2.8/4.3	2.7/3.6	2.3/2.7	2.2/2.4	2.1/2.6	2.2/3.0	2.5/3.8	2.9/4.8	2.3/4.5	2.0/4.7	2.9/3.4

Figure 7- Solar Radiation for Flat-Plate Collectors Facing South at a Fixed Tilt (kWh/m²/day) [16]. The station for these measurements was located in Raleigh, NC.

Determining the approximate energy production from the thermoelectric generators (TEGs) is actually relatively complicated and depends strongly on the design of the TEG, the TEG materials, and heat sinks the TEG uses. Due to the time varying nature of the heat flux as the sun rises and sets, the thermal capacity of the wall, and emissivity of the bricks, calculating the thermal profile across a wall can be daunting. For example, consider the data and models developed by [17] and [18]. As shown in Figure 8, the time dependence is complex and follows a daily pattern with the temperature of the interior surface of a brick lagging the temperature of the exterior surface of the brick by approximately two hours. Wall construction materials, orientation, and thickness greatly influence not only the temperature profile through the wall, but also the time delay in the propagation of thermal energy through the wall. This is summarized by the data in Figures 9 and 10, where the lag between the solar insolation and ambient temperature is clearly seen for both winter and summer conditions, and the variations in heat flux through walls of different thicknesses can also be observed.

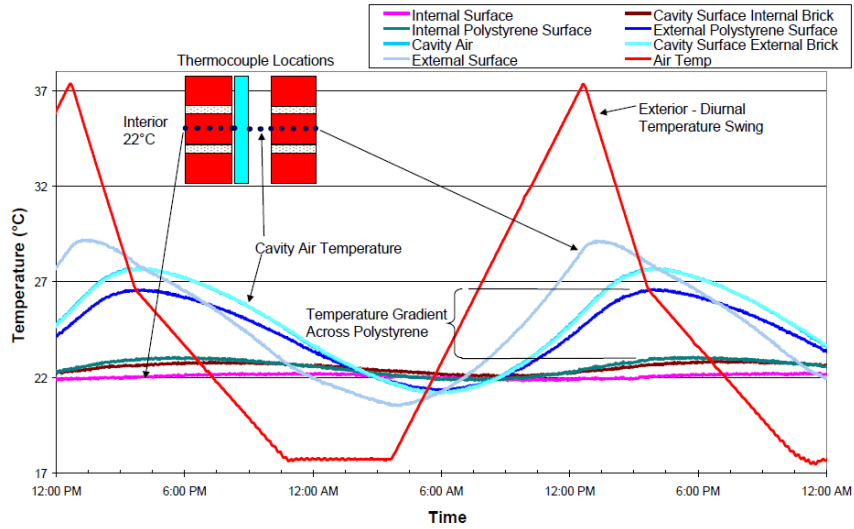


Figure 8- Insulated Cavity Brick Summer Cycle Temperature Profile [18]. The wall was constructed with internal and external brickwork separated by a polystyrene foam sheet and an air cavity.

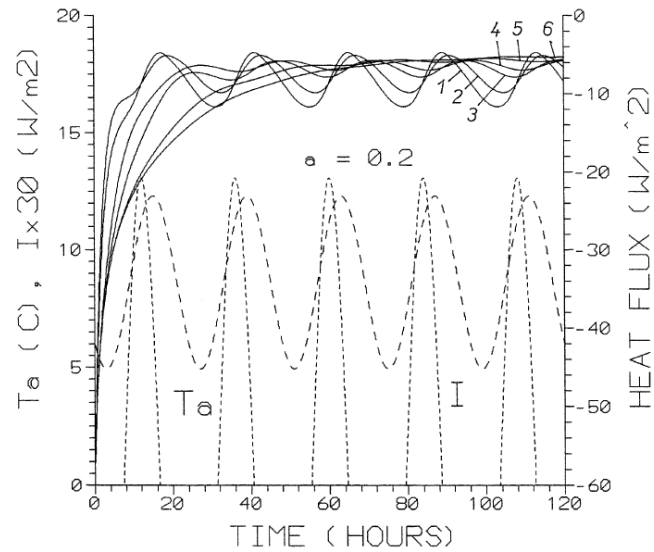


Figure 9- Comparative presentation of the calculated heat fluxes for the lightweight panel WB1 (solid line 1) and the progressively heavier brick walls WB2 to WB6 (solid lines 2-6), for a succession of five sequential winter days. In the same plot, the harmonically varying ambient temperature and the time varying solar insolation are also shown with broken and dotted lines, respectively [17].

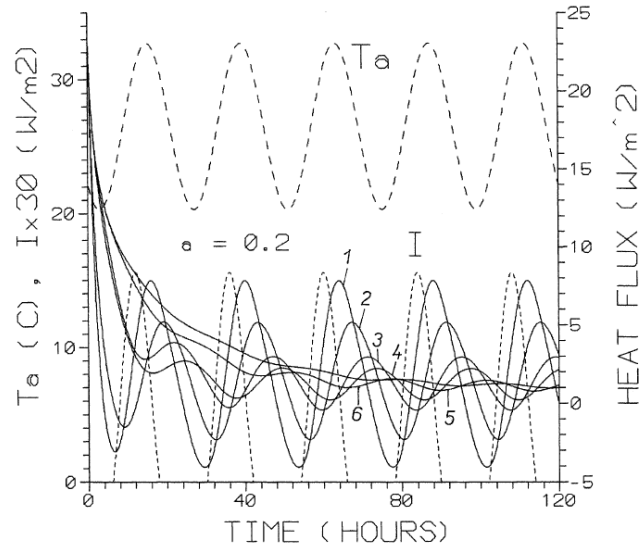


Figure 10- Comparative presentation of the calculated heat fluxes for the lightweight panel WB1 (solid line 1) and the progressively heavier brick walls WB2 to WB6 (solid lines 2–6), for a succession of five sequential summer days. In the same plot, the harmonically varying ambient temperature and the time varying solar insolation are also shown with broken and dotted lines, respectively [17].

There have been previous approaches to make solar thermoelectric modules [19, 20]. These approaches typically have used solar concentrators which are external to the thermoelectric to increase the energy density [21-23]. However, recently there has been an integrated module presented that operates on similar principles to the energy collecting bricks proposed in this paper [24]. This device uses an evacuated glass envelope with a light trapping layer to collect the solar energy, and heat conduction laterally effectively acts as a thermal concentrator with the concentration ratio equal to the ratio of the light collector and thermoelectric areas. While of high performance, due to the use of vacuum isolation, this approach would be substantially harder to integrate into building structures, both aesthetically and structurally.

From the previous figures, one sees that over $5\text{W}/\text{m}^2$ of heat flux is generally available. This suggests that the thermoelectric device will not be heat flux limited. The temperature gradient that is available will depend on the interior temperature of the living space, or in the case of bricks on the ground, by the mean annual soil temperature. The exterior temperature will be determined by the incident solar radiation, the emissivity of the wall, and convection.

Thus schematically we can consider a network of thermal resistors. Figures 11 through 14 below show networks appropriate for modern building construction consisting of an interior sheathing, wood or metal frame wall with fiberglass batting, exterior sheathing, a wrapped Styrofoam vapor barrier, and an exterior brick veneer. A parallel path is shown consisting of a heat collector, thermoelectric generator, and thermal short to the building's interior wall.

For the thermoelectric modules we are working with, the thermal resistance is about $69\text{m}^2\text{K}/\text{W}$. Thus to maximize the temperature difference across the thermoelectric the thermal resistance needs to be minimized from the heat collector to the thermoelectric junction and also minimized from the thermoelectric junction to the wall, air, or ground that is acting as the heat sink. These concerns will be discussed in more detail in the experimental results.

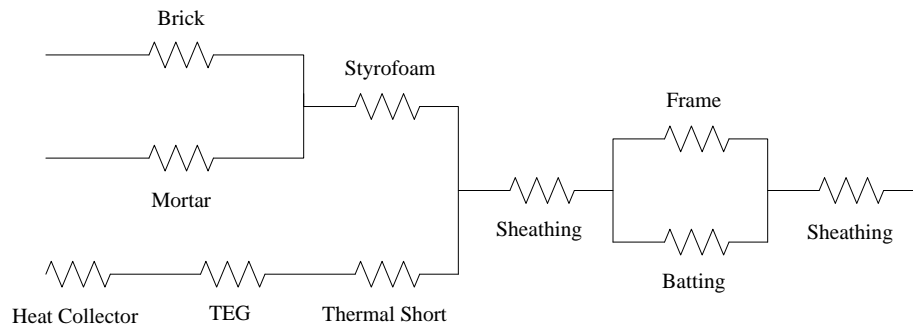


Figure 11- Paired with Figure 12, a resistor network representative of the thermal resistances present in a modern wood or metal frame wall with exterior brick veneer in a configuration in which the internal wall and vapor barrier remain intact. This configuration does not exploit the temperature sink internal to the building.

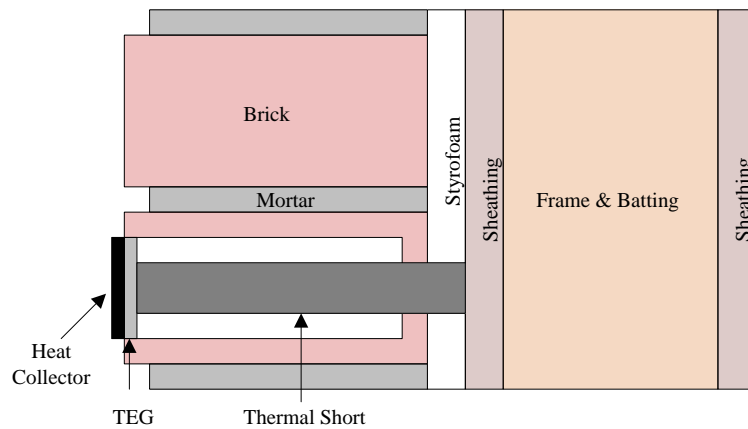


Figure 12- Paired with Figure 11, a vertical slice of a modern wood or metal frame wall with exterior brick veneer in a configuration in which the internal wall and vapor barrier remain intact. This configuration does not exploit the temperature sink internal to the building.

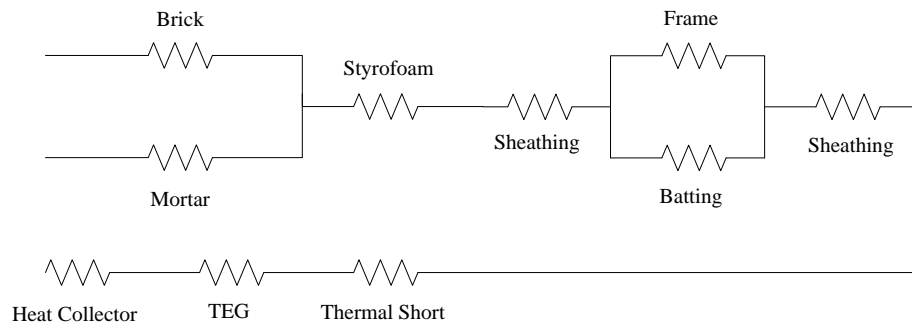


Figure 13- Paired with Figure 14, a resistor network representative of the thermal resistances present in a modern wood or metal frame wall with exterior brick veneer in a configuration in which the thermal short pierces the interior wall and vapor barrier. This configuration best exploits the temperature sink internal to the building.

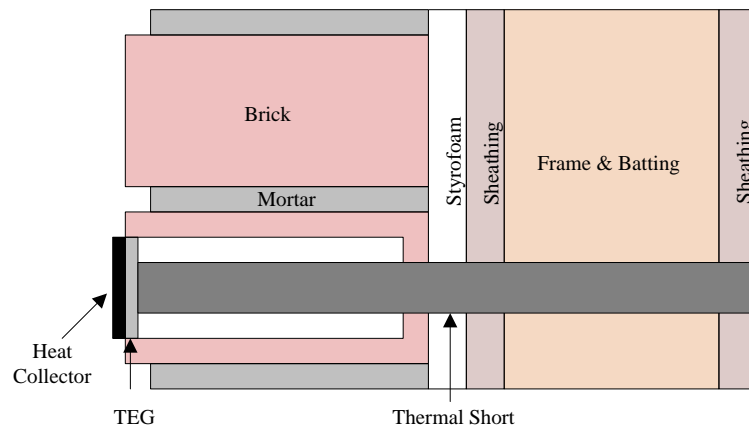


Figure 14- Paired with Figure 13, a vertical slice of a modern wood or metal frame wall with exterior brick veneer in a configuration in which the thermal short pierces the interior wall and vapor barrier. This configuration best exploits the temperature sink internal to the building.

Energy harvesting circuitry maintained the solar panel and thermal generators at their maximum power points. Energy storage was achieved through two batteries and a 1mF

capacitor integrated with the solar panel as well as a 10 Farad and 5 Farad supercapacitor for primary storage and microcontroller storage, respectively.

Sensor selection and their implementation are an important part of the project. Gasses and particulates affect human health in different ways, so a scheme was considered that would investigate the most likely common irritants. For gasses, the most common hazards are from Ozone, Nitrous Oxides, Sulfur Dioxide, and Carbon Monoxide [6]. However, as the selectivity of commercially available sensors is not absolute and can vary with temperature and humidity, additional sensors with known cross-sensitivities were incorporated to allow for primary component analysis, to try to use an electronic nose approach to improve sensor accuracy.

Almost all gas sensors incorporated a resistive filament combined with a sensitive element whose resistance changes in the presence of the test gas. The energy necessary to heat the sensitive element to its rated temperature limited the number of sensors that could be included in the design. Additionally, the heating time required to create a valid measurement severely limited the duty cycle of the entire sensor platform.

Very few particulate sensors fit within the size and system constraints of the lab-in-a-brick. High quality sensors are designed for laboratory environments in which power and maintenance are not significant issues. For this project, any sensor incorporating a vacuum pump or disposable filtration element was ignored, leaving infrared laser scattering counters. While the power requirements were within bounds, well below the gas sensors, the quality of the measurements leaves room for further research in both selectivity to particle sizes as well as accuracy in the particle count itself.

Finally, at the heart of the project was a simple low power microcontroller. The TI MSP430F2274 was chosen due to its low power requirements, ease of integration with the TI RF2500 radio, integrated 10 bit ADC, and multiple low power modes which fit with the sensor duty cycling. A kit was chosen which provided the microcontroller, radio, solar panel, and enough energy storage for 400 wireless transmissions. Modifications were applied to incorporate the additional energy production and storage, and to allow for more robust wireless data transfers.

Chapter 2 – Literature Review

2.1 Overview

Over the past 20 years, there has been extensive research in unattended sensors connected via wireless networks, energy harvesting, and environmental sensors, separately. We anticipate that, much like a residential water meter, the output of our “Lab-in-a-Brick” won’t be connected to a wireless network as a smart node, but only interrogated when the data is required. Therefore, to focus the scope of this review, literature focusing on sensor networks will be ignored. Instead, we will take a systematic approach in evaluating the current state of the art of commercially available sensors platforms and components, energy harvesters, energy storage, and research trends in each of these sections.

For the environmental sensing portion of the review, we will examine air quality and particulate sensor reports by the EPA and researchers who investigate portable air quality sensors for monitoring human health exposure.

For energy harvesting, only a brief overview of technology approaches – solar, RF, thermo, and piezo – and their relative limitations will be given, with more attention being

paid to commercial off the shelf chipsets and data sheets rather than fundamental materials advances or emerging technologies.

In energy storage, commercially available storage options will be listed and compared against system requirements to limit the overall scope.

2.2 Sensor Platforms

When reviewing sensor platforms, there is a vast collection of sensors of various sizes for a myriad of purposes. The Lab-in-a-Brick is designed for the express purpose of measuring air quality, therefore this review will begin with air quality sensors currently in use. However, even the more limited scope of commercially available sensors or currently deployed industrial sensors is overly wide. As a starting point, we will begin with the sensor systems utilized by the North Carolina Division of Air Quality.

The North Carolina Division of Air Quality operates 60 monitoring stations to measure the ambient concentrations of pollutants including ozone, lead, dust particles, nitrogen oxides, sulfur dioxide, and carbon monoxide. The monitoring site located at Millbrook Middle School in Raleigh can be taken as a representative site. As shown in Figure 15, this site contains many fine particle monitors, a sulfur dioxide monitor, a carbon monoxide monitor, and reactive oxides of nitrogen monitors [6]. These are by no means small or inexpensive sensors. In order to model how pollutant concentrations move throughout the state, the data from each of these sensor sites is combined into computationally expensive models utilizing known dispersal behaviours for each pollutant

with meteorological data to provide highly approximate concentration maps. Additionally, these sites require a grid power connection and routine maintenance to replace particulate filters and make repairs.



Figure 15- Millbrook NCore Monitoring Site [6].

In a step towards the Lab-in-a-Brick, there are commercially available sensor systems to replace the multitudes of individual sensors currently in use. One such example is the AQM 60 Air Quality Station from Aeroqual. Combining everything found at the Millbrook

site, this platform includes sensors for ozone, nitrogen dioxide, nitrogen oxides, carbon monoxide, sulphur dioxide, volatile organic compounds, hydrogen sulphide, non-methane hydrocarbons, carbon dioxide, PM₁₀ and PM_{2.5} particulates, noise, temperature, humidity, and wind speed and direction into a single box. Additionally, various wireless communications modules can be incorporated to allow for unattended operation. However, there are certain drawbacks. The platform requires 80 to 160W of power, depending on sensor configuration [4]. Also, one of the goals is to have unobtrusive sensors that blend in with standard building construction materials, which this system does not.



Figure 16- Aeroqual AQM 60 Air Quality Station [4].

There are no smaller air quality monitoring platforms available commercially that incorporate anything even remotely close to the range of gasses and particulates that these two systems include. Portable particulate monitors and specific gas monitors are available, but these start in the hundreds of dollars for the gas monitors and thousands of dollars for the particulate counters. Transitioning from commercial products to research prototypes yields smaller, more advanced sensors.

Researchers at the University of Michigan have created a simple wireless indoor air quality monitoring sensor network utilizing a dust counter and gas detectors tuned for carbon dioxide, carbon monoxide, ozone, volatile organic compounds, temperature, and humidity. Energy is provided by two AA batteries. Networking is provided through a ZigBee radio. This research is motivated by a need to understand the indoor environment. Buildings themselves often give off gasses that in high concentrations can be harmful to people. By incorporating air quality sensors with a wireless transceiver, eliminating the need for wires to network the sensors together, controls can be implemented in virtually any building with an air handling system that adjust the indoor environment based on these sensors' input. While it was realized that both maintenance for the sensor system as well as wiring for permanent power were to be avoided, no attempt was made to incorporate internal energy harvesting.

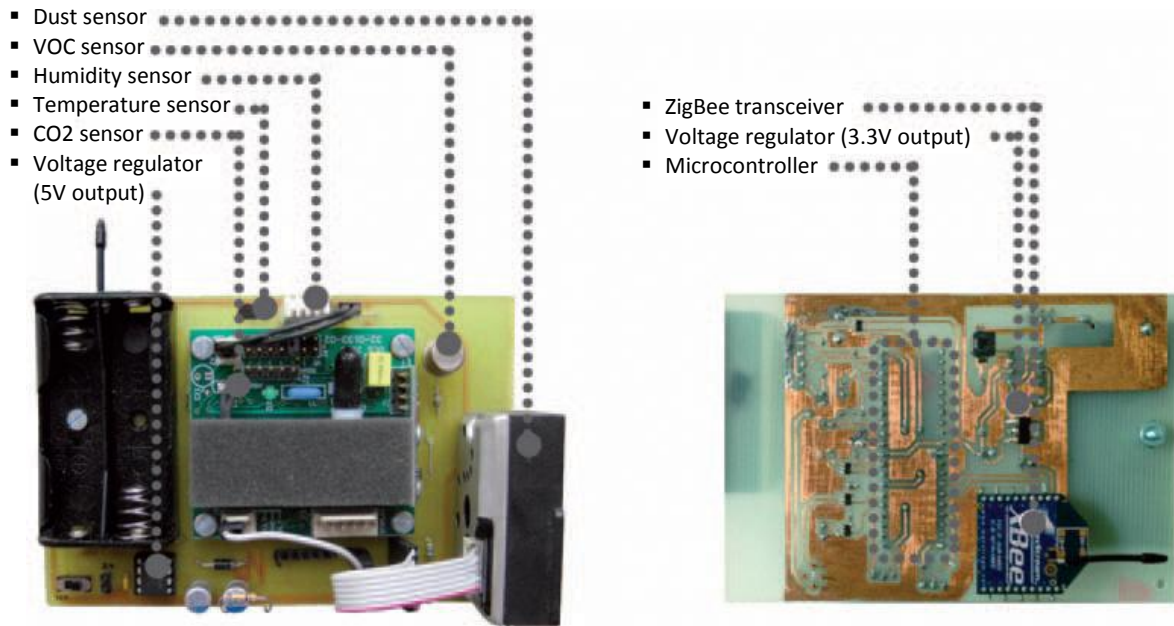


Figure 17- Indoor Air Quality transceiver implementing sensors for dust, VOC, humidity, temperature, and CO2, and a ZigBee radio [25].

Researchers at Arizona State University recently published data demonstrating a highly effective wearable VOC monitor. Approximately the size of a modern smartphone, the sensor utilizes the changes in resonant frequencies of crystals coated with a chemically active polymer to determine the concentration of hydrocarbon gasses with part-per-billion accuracy. While the novel sensor provides great accuracy, it has the caveat of a three minute cycle consisting of a two minute purge and a minute sampling time to provide each data point, during which time the sensor operates a small air pump. Also, calibration is required monthly. A Li-ion polymer battery is included in the system that can operate it for 10 hours of continuous measurements, and is recharged from a standard wall outlet [3].

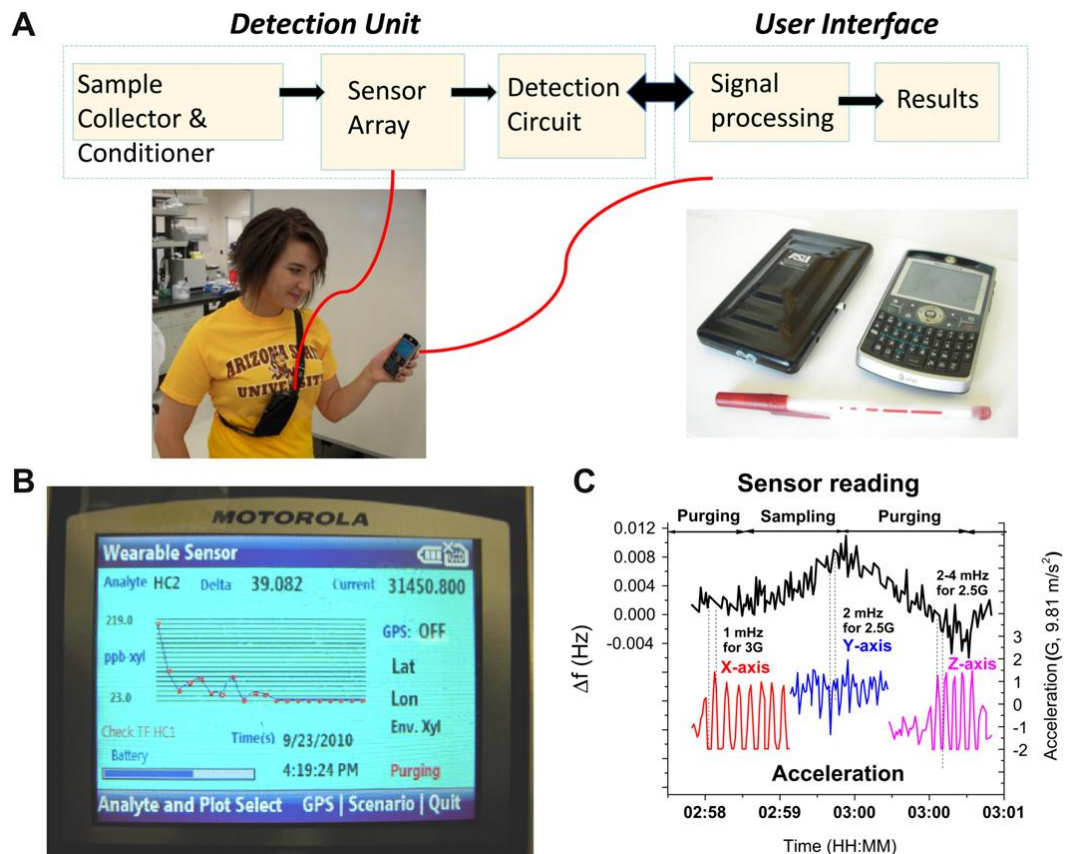


Figure 18- Wearable VOC sensor. (A) Sensor components, and pictures. It shows a person wearing the detection unit near the breathing zone while holding the phone that acts as user interface, as well as a view of both VOC sensor components. (B) User interface on the phone, displaying the data received from the monitor. (C) Robustness test: the plot shows the sensor response (at 1-Hz data resolution) during x-, y-, and z- acceleration events detected with an accelerometer attached to the VOC sensor [3].

The vast majority of the innovation for wireless sensor networks is for the health industry and not for measuring air quality. However, often the advances can be directly transferred to any type of sensor network, regardless of application. For example, South Korean researchers recently demonstrated a wireless body sensor network incorporating an EEG, ECG, respiration monitor, and PPG. The sensor platform was designed with reliability, low power consumption, low cost, and compactness in mind, all of which directly transfer

over to the Lab-in-a-Brick, even if the sensors are wholly unrelated. Three prototypes were developed: one utilized an 8-channel EEG sensor and the Zigbee communication protocol, another utilized a 4-channel multi-body sensor and the Bluetooth communication protocol, and the final being an enhanced version of the 4-channel multi-body sensor with Bluetooth. While the power drawn for each of these prototypes is not listed, current is, and given that images of the systems clearly show a standard 9V battery as the power source, it can be reasonably assumed that the listed current measurements are at either a 3V or 5V reference. Therefore, the Zigbee design used approximately 161-268mW, the Bluetooth design used 448-747mW, and the enhanced Bluetooth design used 312-521mW of power [26]. It is of note that duty cycling was not employed in this research due to the requirement for continuous monitoring of the signals in question.

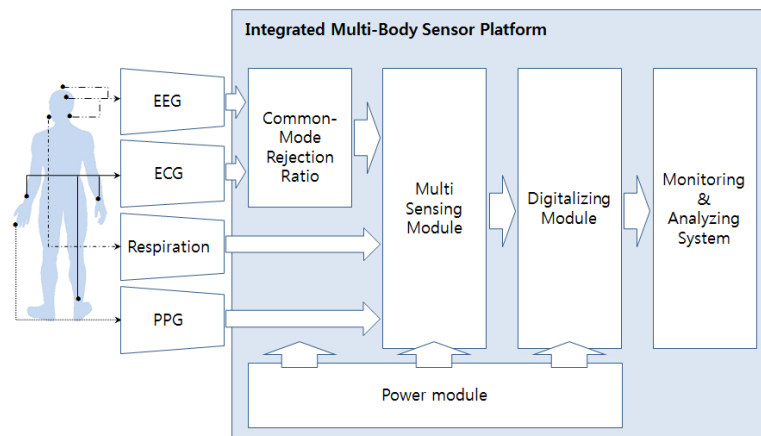


Figure 19- Structure of the integrated multi-body sensor platform [26].

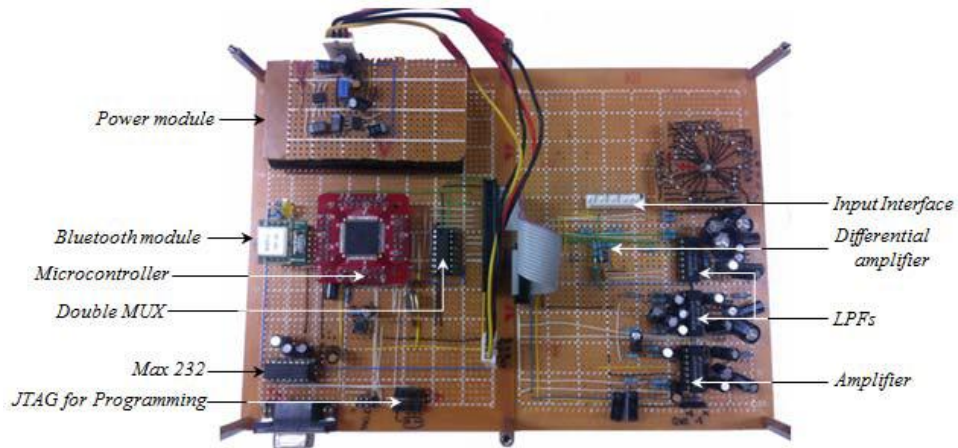


Figure 20- Prototype multi-body sensor platform [26].

Very few wireless sensors incorporate any type of energy harvesting. Sensors and radios generally require power far in excess of what an energy harvester can generate, but cycling the sensor platform on and off allows for the storage of a small but consistent stream of power for bursts of energy intensive operations. For example, a diagram for a generic sensor platform incorporating energy harvesting is provided in Figure 21 below. The nanogenerator noted in Figure 21 is piezoelectric, but it can simply be switched for whatever energy source is most prolific in the sensor's intended environment. Additional consideration for power generation and energy storage are in section 2.4.

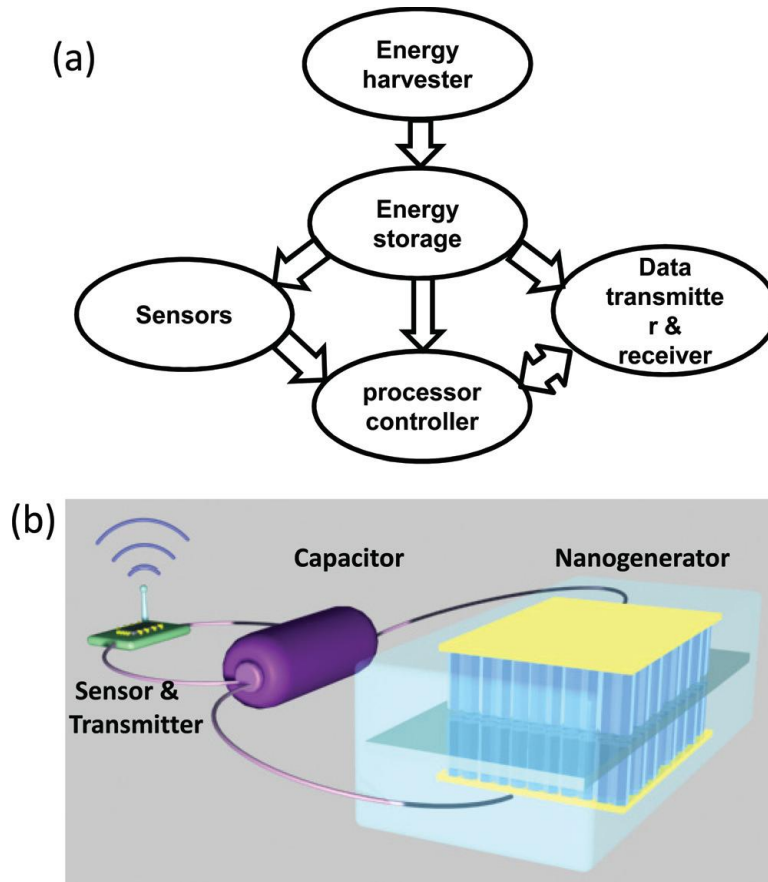


Figure 21- Schematic diagram of the integrated self-powered system. a) An integrated system can be divided into five modules: energy harvester, energy storage, sensors, data processor & controller, and data transmitter & receiver. b) Prototype of an integrated self-powered system using a nanogenerator as the energy harvester [27].

2.3 Air Quality Sensors

The effects of gasses and particulates on individuals vary widely according to the type and concentration of the pollutant. The EPA tracks and regulates six principle pollutants due to their impact on health [28]. These pollutants are the starting point for our investigation of air quality sensors. The Lab-in-a-Brick should be sensitive to as many of these pollutants as possible and able to track the concentration around the limits set. These

levels exist mainly for regulatory purposes and should not be taken as limits in the sensing range.

Table 3- National Ambient Air Quality Standards (NAAQS) table of pollutants and allowable maximum levels as of October 2011 [28].

Pollutant [final rule cite]	Primary/ Secondary	Averaging Time	Level	Form	
Carbon Monoxide [76 FR 54294, Aug 31, 2011]	primary	8-hour	9 ppm	Not to be exceeded more than once per year	
		1-hour	35 ppm		
Lead [73 FR 66964, Nov 12, 2008]	primary and secondary	Rolling 3 month average	0.15 µg/m ³	Not to be exceeded	
Nitrogen Dioxide [75 FR 6474, Feb 9, 2010] [61 FR 52852, Oct 8, 1996]	primary	1-hour	100 ppb	98th percentile, averaged over 3 years	
	primary and secondary	Annual	53 ppb	Annual Mean	
Ozone [73 FR 16436, Mar 27, 2008]	primary and secondary	8-hour	0.075 ppm	Annual fourth-highest daily maximum 8-hr concentration, averaged over 3 years	
Particle Pollution [71 FR 61144, Oct 17, 2006]	PM _{2.5}	primary and secondary	Annual	15 µg/m ³	annual mean, averaged over 3 years
			24-hour	35 µg/m ³	98th percentile, averaged over 3 years
	PM ₁₀	primary and secondary	24-hour	150 µg/m ³	Not to be exceeded more than once per year on average over 3 years
Sulfur Dioxide [75 FR 35520, Jun 22, 2010] [38 FR 25678, Sept 14, 1973]	primary	1-hour	75 ppb	99th percentile of 1-hour daily maximum concentrations, averaged over 3 years	
	secondary	3-hour	0.5 ppm	Not to be exceeded more than once per year	

As shown in Table 3, sensors can be divided between particulate and gas types. For the purposes of this research review, emphasis will be placed on those sensors with reduced energy and maintenance requirements.

The investigation begins with gas sensors. There are a wide variety of commercially available products, and Table 4 lists many of them with their respective voltage and power requirements. The majority of these sensors utilize a combination of two elements: a heating element and a variable resistor sensitive to the target gas. Another sensing method that is gaining popularity is IR absorption which exploits the attenuation of specific frequencies of light by different gasses to determine their presence. Research is very active in this field, with many groups reducing the power requirements while others are finding novel sensing methods.

Table 4- Commercial gas sensors with varying heater voltages, costs, and selectivity. Energy requirements are approximated based on minimum listed settling times. Information compiled from publicly available datasheets.

Name	Part Number	Type	Method	Company	Volt Range	Min Power	Min Energy	Cost / unit
Air Quality	MQ-135	Carbon Monoxide, Ammonia, Carbon Dioxide, Benzene	Heater / Resistor	Futurlec	4.9V - 5.1V	800mW	48J	\$6.90
Alcohol	MQ-3	Alcohol, Benzene	Heater / Resistor	Futurlec	4.9V - 5.1V	800mW	48J	\$6.90
Methane	MQ-4	Methane, Propane, Hydrogen, Butane	Heater / Resistor	Futurlec	4.8V - 5.2V	900mW	54J	\$3.90
Carbon Monoxide	MQ-7	Hydrogen, Carbon Monoxide, Propane, Methane, Alcohol	Heater / Resistor	Futurlec	4.9V - 5.1V	750mW	45J	\$8.90
Carbon Dioxide	MG811	Carbon Dioxide, Carbon Monoxide	Heater / Resistor	Futurlec	5.9V - 6.1V	1.2W	72J	\$19.90
Hydrogen	MQ-8	Hydrogen, Alcohol, Propane, Methane, Carbon Monoxide	Heater / Resistor	Futurlec	4.9V - 5.1V	800mW	48J	\$6.90
Natural Gas	H2 SENSOR	Propane, Methane, Hydrogen, Alcohol, Carbon Monoxide	Heater / Resistor	Futurlec	4.9V - 5.1V	800mW	48J	\$6.90
Propane	MQ-6	Propane, Methane, Hydrogen, Alcohol, Carbon Monoxide	Heater / Resistor	Futurlec	4.9V - 5.1V	750mW	45J	\$6.90
Ozone	MQ-131	Ozone, Chlorine, Nox	Heater / Resistor	Futurlec	5.9V - 6.1V	1.1W	66J	\$12.90
Ambient Range CO2	CO2S-PPM	Carbon Dioxide	Non-dispersive IR absorption	SST	3.25V - 5.5V	3.5mW	35mJ	
Ambient Range CO2	COZIR	Carbon Dioxide	Non-dispersive IR absorption	GSS	3.25V - 5.5V	3.5mW	35mJ	
Trace Hydrogen	701	Hydrogen	Heater / Resistor	Synkera	5.4V	600mW	60J	\$48

Table 4 Continued

LEL Hydrogen	703	Hydrogen, Ethanol, Carbon Monoxide, Methane	Heater / Resistor	Synkera	2.1V	150mW	15J	\$48
Ammonia	705	Ammonia, Methanol	Heater / Resistor	Synkera	7.5V	975mW	175.5J	\$54
NOx	706	Nitrogen Oxides	Heater / Resistor	Synkera	4.7V	500mW	50J	\$54
VOC	707	Hexene, Methoxyethanol, Cyclohexane, Tetrahydrofuran, Ethanol, Propanol, etc	Heater / Resistor	Synkera	3.5V	400mW	48J	\$48
Flammable Gas	711	Propane, Hydrogen, Methane	Heater / Resistor	Synkera	5.3V	900mW	90J	\$48
Nitrogen Trifluoride	712	Nitrogen Trifluoride	Heater / Resistor	Synkera	6V	750mW	225J	\$300
Hydrogen Sulfide	714	Hydrogen Sulfide	Heater / Resistor	Synkera	7V	900mW	90J	\$54
Hydrogen	724	Hydrogen, Hydrogen Sulfide, Ethanol, Carbon Monoxide, Methane	Heater / Resistor	Synkera	1.45V	125mW	15J	\$48
VOC	725	Isobutylene, Methanol, MEK, Toluene	Heater / Resistor	Synkera	1.25V	100mW	6J	\$48
Chlorine	726	Chlorine	Heater / Resistor	Synkera	1V	65mW	19.5J	\$54
Hydrogen Sulfide	727	Hydrogen Sulfide, Ethanol, Hydrogen, Methane	Heater / Resistor	Synkera	2.2V	225mW	13.5J	\$54
Ammonia	728	Ammonia	Heater / Resistor	Synkera	2.1V	225mW	27J	\$54
O3	MiCS-2610	Ozone	Heater / Resistor	SGX Sensortech	2.35V	80mW	4.8J	\$6.18
O3	MiCS-2611	Ozone	Heater / Resistor	SGX Sensortech	2.35V	80mW	4.8J	\$7.98
O3	MiCS-2614	Ozone	Heater / Resistor	SGX Sensortech	2.35V	80mW	4.8J	\$6.31
NO2	MiCS-2710	Nitrogen Dioxide	Heater / Resistor	SGX Sensortech	1.7V	43mW	2.58J	\$5.53
NO2	MiCS-2714	Nitrogen Dioxide	Heater / Resistor	SGX Sensortech	1.7V	43mW	2.58J	\$5.02
CO & NO2	MiCS-4514	Carbon Dioxide, Hydrocarbons, and Nitrous Oxide	Heater / Resistor	SGX Sensortech	2.4V & 1.7V	119mW	7.14J	\$6.31
CO & VOC	MiCS-5121	Carbon Monoxide, Hydrocarbons, Volatile Organic Compounds	Heater / Resistor	SGX Sensortech	2.4V	76mW	4.56J	
CO & VOC	MiCS-5121WP	Carbon Monoxide, Hydrocarbons, Volatile Organic Compounds	Heater / Resistor	SGX Sensortech	2.4V	76mW	4.56J	\$7.59
VOC	MiCS-5135	Carbon Monoxide, Hydrocarbons, Ethanol, Volatile Organic Compounds	Heater / Resistor	SGX Sensortech	3.2V	102mW	6.12J	
H2	MiCS-5315	Hydrogen	Heater / Resistor w/ Charcoal Filter	SGX Sensortech	1.6V	40mW	2.4J	\$8.62

Table 4 Continued

CO & VOC	MiCS-5521	Carbon Monoxide, Hydrocarbons, Volatile Organic Compounds	Heater / Resistor	SGX Sensortech	2.4V	76mW	4.56J	\$5.53
CO & VOC	MiCS-5524	Carbon Monoxide, Hydrocarbons, Volatile Organic Compounds	Heater / Resistor	SGX Sensortech	2.4V	76mW	4.56J	\$4.76
CO	MiCS-5525	Carbon Monoxide	Heater / Resistor w/ Charcoal Filter	SGX Sensortech	2.4V	76mW	4.56J	\$8.24
CO & VOC	MiCS-5526	Carbon Monoxide, Hydrocarbons, Volatile Organic Compounds	Heater / Resistor	SGX Sensortech	2.4V	76mW	4.56J	
Ammonia	MiCS-5914	NH3	Heater / Resistor	SGX Sensortech	2.2V	66mW	3.96J	\$5.02
Carbon Dioxide	IR11BD	Carbon Dioxide	Non-dispersive IR absorption	SGX Sensortech	3V – 15V	180mW	3.6J	\$213.49
Carbon Dioxide	IR11BR	Carbon Dioxide	Non-dispersive IR absorption	SGX Sensortech	3V – 15V	180mW	3.6J	\$182.53
Carbon Dioxide	IR11EJ	Carbon Dioxide	Non-dispersive IR absorption	SGX Sensortech	3V – 15V	180mW	3.6J	\$182.53
Carbon Dioxide	IR11EM	Carbon Dioxide	Non-dispersive IR absorption	SGX Sensortech	3V – 15V	180mW	3.6J	\$194.13
Carbon Dioxide	IR11GJ	Carbon Dioxide	Non-dispersive IR absorption	SGX Sensortech	3V – 10V	180mW	3.6J	\$194.13
Carbon Dioxide	IR11GM	Carbon Dioxide	Non-dispersive IR absorption	SGX Sensortech	3V – 10V	180mW	3.6J	\$195.95
Hydro-carbon	IR12BD	Butane, Ethanol, Ethylene, Hexane, Methane, Methanol	Non-dispersive IR absorption	SGX Sensortech	3V – 15V	180mW	3.6J	\$216.20
Hydro-carbon	IR12EJ	Butane, Ethanol, Ethylene, Hexane, Methane, Methanol	Non-dispersive IR absorption	SGX Sensortech	3V – 15V	180mW	3.6J	\$185.47
Hydro-carbon	IR12GJ	Butane, Ethanol, Ethylene, Hexane, Methane, Methanol	Non-dispersive IR absorption	SGX Sensortech	3V – 10V	180mW	3.6J	\$185.47
Carbon Dioxide	IR12GM	Carbon Dioxide	Non-dispersive IR absorption	SGX Sensortech	3V – 10V	180mW	3.6J	\$185.85
Hydro-carbon	IR13BD	Benzene, Butane, Ethanol, Ethylene, Hexane, Methane, Methanol	Non-dispersive IR absorption	SGX Sensortech	3V – 15V	180mW	3.6J	\$264.00
Acetylene	IR14BD	Acetylene	Non-dispersive IR absorption	SGX Sensortech	3V – 15V	180mW	3.6J	\$275.00
Carbon Dioxide & Methane	IR15TT	Carbon Dioxide, Methane	Non-dispersive IR absorption	SGX Sensortech	3V – 15V	180mW	3.6J	\$305.19
Carbon Dioxide & Methane	IR15TT-M	Carbon Dioxide, Methane	Non-dispersive IR absorption	SGX Sensortech	3V – 15V	180mW	3.6J	\$290.07
Carbon Dioxide & Methane	IR15TT-R	Carbon Dioxide, Methane	Non-dispersive IR absorption	SGX Sensortech	3V – 15V	180mW	3.6J	\$290.07
Carbon Dioxide	IR21BD	Carbon Dioxide	Non-dispersive IR absorption	SGX Sensortech	3V – 15V	180mW	3.6J	\$262.48

Table 4 Continued

Carbon Dioxide	IR21EJ	Carbon Dioxide	Non-dispersive IR absorption	SGX Sensortech	3V – 15V	180mW	3.6J	\$200.95
Carbon Dioxide	IR21EM	Carbon Dioxide	Non-dispersive IR absorption	SGX Sensortech	3V – 15V	180mW	3.6J	\$195.22
Carbon Dioxide	IR21GJ	Carbon Dioxide	Non-dispersive IR absorption	SGX Sensortech	3V – 10V	180mW	3.6J	\$194.50
Carbon Dioxide	IR21GM	Carbon Dioxide	Non-dispersive IR absorption	SGX Sensortech	3V – 10V	180mW	3.6J	\$202.83
Hydro-carbon	IR22BD	Butane, Ethanol, Ethylene, Hexane, Methane, Methanol	Non-dispersive IR absorption	SGX Sensortech	3V – 15V	180mW	3.6J	\$266.08
Hydro-carbon	IR22EJ	Butane, Ethanol, Ethylene, Hexane, Methane, Methanol	Non-dispersive IR absorption	SGX Sensortech	3V – 15V	180mW	3.6J	\$200.95
Hydro-carbon	IR22GJ	Butane, Ethanol, Ethylene, Hexane, Methane, Methanol	Non-dispersive IR absorption	SGX Sensortech	3V – 10V	180mW	3.6J	\$192.53
Hydro-carbon	IR23BD	Butane, Ethanol, Ethylene, Hexane, Methane, Methanol	Non-dispersive IR absorption	SGX Sensortech	3V – 15V	180mW	3.6J	\$264.00
Carbon Dioxide & Methane	IR25TT	Carbon Dioxide, Methane	Non-dispersive IR absorption	SGX Sensortech	3V – 15V	180mW	3.6J	\$305.19
Carbon Dioxide & Methane	IR25TT-M	Carbon Dioxide, Methane	Non-dispersive IR absorption	SGX Sensortech	3V – 15V	180mW	3.6J	\$290.07
Carbon Dioxide	IR31BC	Carbon Dioxide	Non-dispersive IR absorption	SGX Sensortech	3V – 15V	180mW	3.6J	\$290.95
Carbon Dioxide	IR31CE	Carbon Dioxide	Non-dispersive IR absorption	SGX Sensortech	3V – 15V	180mW	3.6J	\$344.00
Carbon Dioxide	IR31CEN	Carbon Dioxide	Non-dispersive IR absorption	SGX Sensortech	3V – 15V	180mW	3.6J	\$816.21
Carbon Dioxide	IR31SC	Carbon Dioxide	Non-dispersive IR absorption	SGX Sensortech	3V – 15V	180mW	3.6J	\$190.26
Carbon Dioxide	IR31SE	Carbon Dioxide	Non-dispersive IR absorption	SGX Sensortech	3V – 15V	180mW	3.6J	\$193.05
Hydro-carbon	IR32BC	Butane, Ethanol, Ethylene, Hexane, Methane, Methanol	Non-dispersive IR absorption	SGX Sensortech	3V – 15V	180mW	3.6J	\$227.70
Hydro-carbon	IR33BC	Benzene, Butane, Ethanol, Ethylene, Hexane, Methane, Methanol	Non-dispersive IR absorption	SGX Sensortech	3V – 15V	180mW	3.6J	\$243.85
Acetylene	IR34BC	Acetylene	Non-dispersive IR absorption	SGX Sensortech	3V – 15V	180mW	3.6J	
Hydro-carbon	IR42BC	Benzene, Butane, Ethanol, Ethylene, Hexane, Methane, Methanol	Non-dispersive IR absorption	SGX Sensortech	3V – 15V	300mW	6J	
Carbon Dioxide	IR601	Carbon Dioxide	Non-dispersive IR absorption	SGX Sensortech	5V	180mW	7.2J	\$434.65
Hydro-carbon	IR602	Ethylene, Methane, Propane	Non-dispersive IR absorption	SGX Sensortech	5V	180mW	7.2J	\$434.65
Hydro-carbon	IR603	Benzene, Ethylene, Methane, Propane	Non-dispersive IR absorption	SGX Sensortech	5V	180mW	7.2J	\$434.65
Acetylene	IR604	Acetylene	Non-dispersive IR absorption	SGX Sensortech	5V	180mW	7.2J	\$434.65

Table 4 Continued

Carbon Dioxide	IR81BB	Carbon Dioxide	Non-dispersive IR absorption	SGX Sensortech	5V	150mW	3J	\$268.40
Carbon Dioxide	IR82BB	Carbon Dioxide	Non-dispersive IR absorption	SGX Sensortech	5V	150mW	3J	\$268.40

From the above table, one can infer some useful information related to sensing trends. First, resistive sensing with a heated element is a relatively inexpensive mature technology, but also relatively energy intensive and non-selective. Second, IR absorption is younger, more expensive, more selective, and requires much less energy, but is also very limited in gasses to which it can be applied. A lot of work is currently being undertaken to improve the current methods for detection as well as to identify novel procedures, all in an effort to create smaller, more energy efficient, highly sensitive, and highly selective sensors. While the majority of commercially available gas sensors are of the metal oxide variety, IR absorption sensors are emerging for various gasses, and schemes involving surface plasmon resonance and cantilever resonant frequency shifts have been demonstrated in research prototypes.

At its simplest form, metal oxide sensors operate by exploiting the change in resistance of a compound in the presence of a target gas. For example, the commercially available Futurlec MQ-135 is a general-purpose sensor that reacts to ammonia, nitrous oxides, alcohol, volatile organics, and carbon dioxide. A heater electrode raises the temperature of the sensor to increase sensitivity. The sensitive electrode is coated with tin dioxide which, depending on the gas in question, either acts as a catalyst to liberate electrons from the target gas or to adsorb gas molecules from the ambient air. Similar effects are seen with other gas sensitive compounds, such as zinc oxide. The compound, added metals,

physical orientation, and temperature all play a part to determine the sensitivity and selectivity of the sensor.

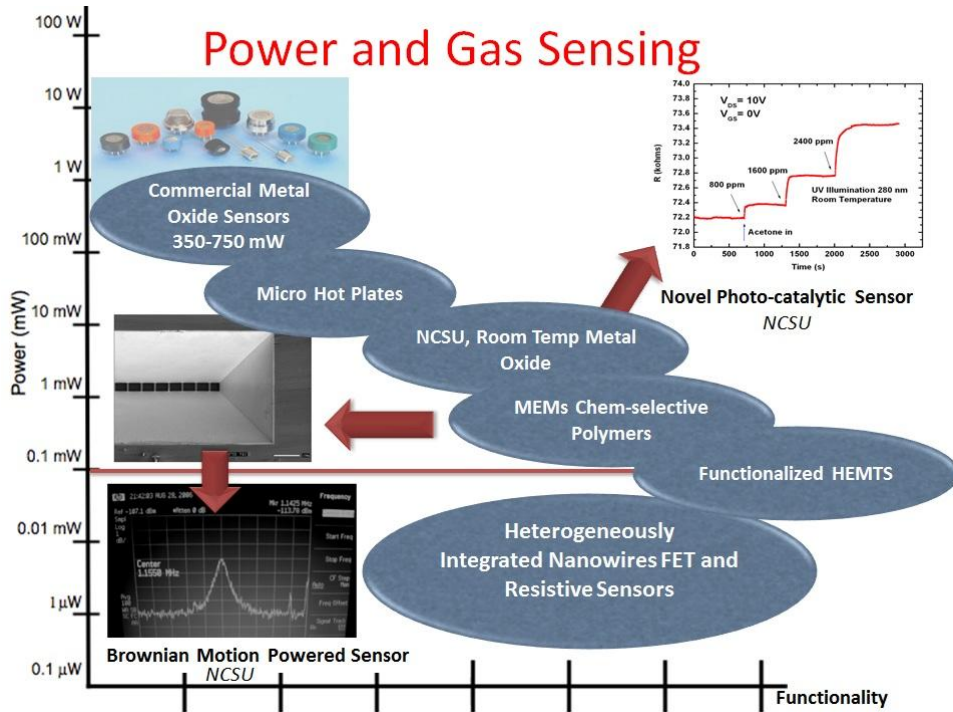


Figure 22- Comparison of various sensing methods outlining their approximate power requirements versus functionality.

Much research aims at reducing the size of the cross-sectional area of the sensing electrode while increasing the surface area, which should provide a greater change in resistance for a given gas concentration. One method to accomplish this is to grow single-crystal SnO_2 nanowires for the detection of NO_x (a mixture of nitric oxide and nitrogen dioxides). Interdigitated electrodes were bridged with a network of randomly grown nanowires characterized by an average diameter of 80nm but lengths up to hundreds of

microns. This extreme surface area to cross section ratio allowed researchers to increase the sensitivity by a factor of four over thin-film sensor approaches, achieving similar changes in resistance at 5ppm for the nanowires as the thin-films experience at 20ppm. However, this increase in sensitivity also resulted in the sensor saturating around 20ppm [29].

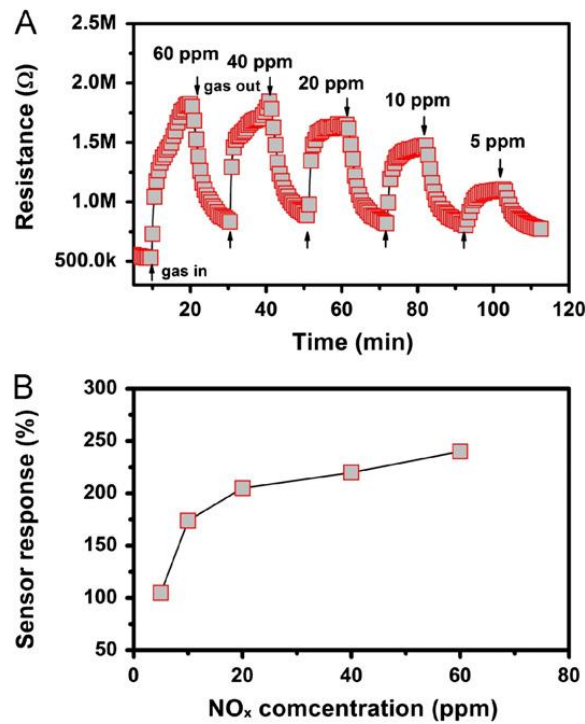


Figure 23- (A) The change in sensor resistances upon the exposure of different concentrations of NO_x, (B) and sensor response as a function of gas concentration [29].

Another thrust aims to reduce the total sensor energy requirement by incorporating the heater element as part of the sensing element. Given that the temperature of the sensing element greatly affects its sensitivity, incorporating both elements physically into the same wire improves its response and lowers the power requirement. Korean researchers fabricated

a sensor with a resistive wire heater underneath a thin film of tin dioxide sensing material with platinum catalyst dots on top [30]. This configuration resulted in a power requirement around 300mW, approximately half that required by a similar commercially-available Futurlec carbon monoxide sensor, the MQ-7. Reduced power consumption is not the greatest improvement in this research, however. Response time for this sensor is 12 seconds, far below the 60 second minimum time for the MQ-7.

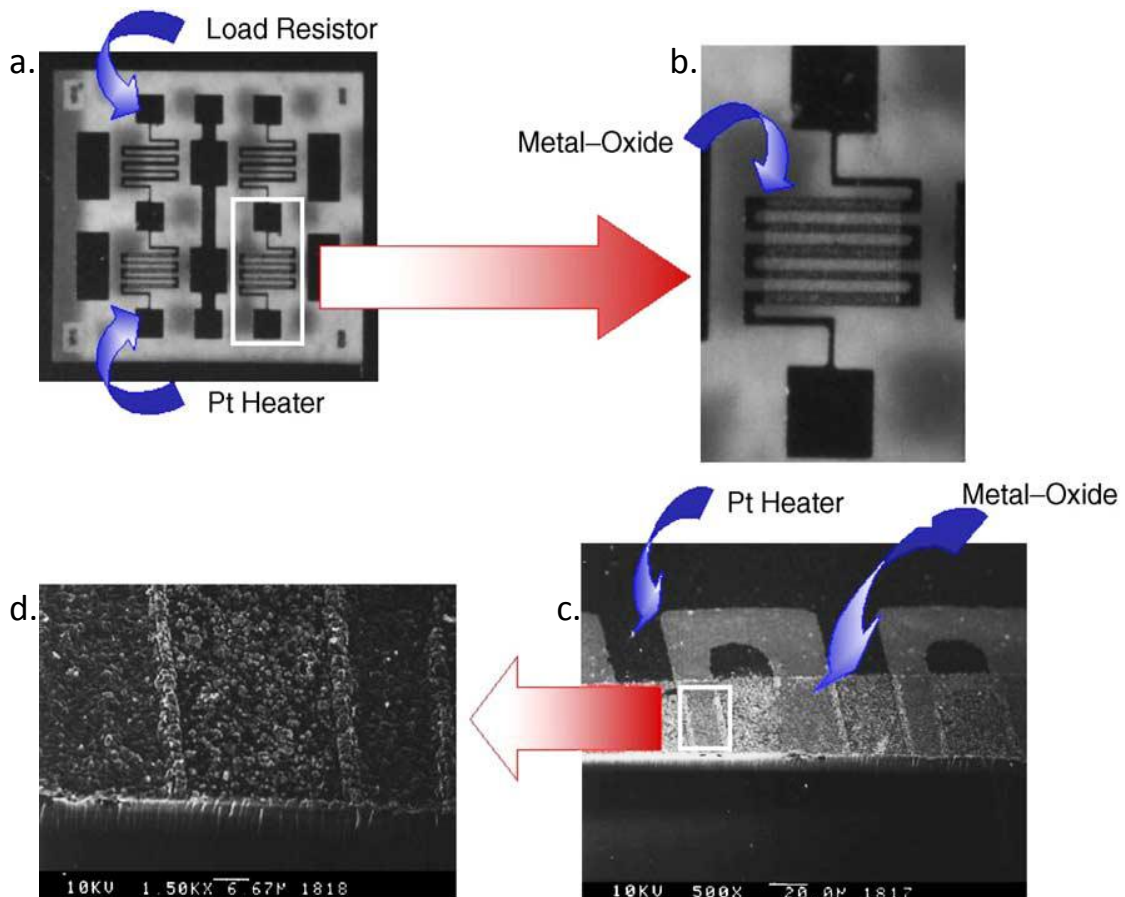


Figure 24 - Carbon monoxide thin-film micro hot wire sensor in a. showing two parallel sensors consisting of a combination heater and sensor electrode in series with a load resistor. A blowup of the heater element in b. shows the thin-film metal-oxide gas sensitive layer applied across the top of the heater, with a partial cross-section and finer detail in c. D. shows the additional platinum catalyst beads added to the top of the metal oxide layer [30].

An emerging method for gas sensing exploits the absorption of specific frequencies of IR light. The device generally consists of either an LED or incandescent light source with a known IR frequency profile. Between the source and either a photonic or thermal sensor is the gas chamber. Photonic sensors in the IR range require cryogenic cooling and are not generally used. Thermal sensors show good response and low power requirements. The gas chamber has ports to allow ambient air to enter. A closed chamber and second sensor must be included as a reference to compensate for any changes in source light intensity. Sensors have been produced for various gasses including carbon monoxide [31], methane [31, 32], and many other similar hydrocarbons. The thermal sensors and light source have a low power requirement, and signals quickly stabilize resulting in extremely low energy needs per sensing event. Commercial sensors have been developed, but their current price versus metal oxide sensors have kept them out of widespread use.

Surface plasmon resonance occurs when light strikes a solid and induces an oscillation in the surface electrons. This phenomenon only occurs at a very narrow range of angles depending on the dielectric constants of both the solid and whatever is next to its surface, and both the frequency and polarization of the incident light. As light of a very narrow incident angle is absorbed and its energy transferred to the plasmons, if a multi-angled light source is applied, the reflected light will show a physical gap corresponding to lack of a reflection of that absorbed light. Alternatively, if a multi-spectral light source is used at a single angle, a very narrow range of frequencies will be absorbed and transformed into plasmons, and the remaining light will be reflected. Sensors can thereby be created by choosing a particular solid that reacts to a target molecule by changing its dielectric constant.

The changing dielectric constant will change the angle or frequency of the absorbed light.

Researchers at Miami University created one such sensor for ozone using gold nanoislands in which an increase in ozone concentration results in a shift in absorbed frequency [33]. While the detectable concentration ranges from 20ppb up to nearly 200ppb, easily covering the EPA limit of 75ppb, and the sensor shows good selectivity and reversibility, NOx completely destroy the nanoislands.

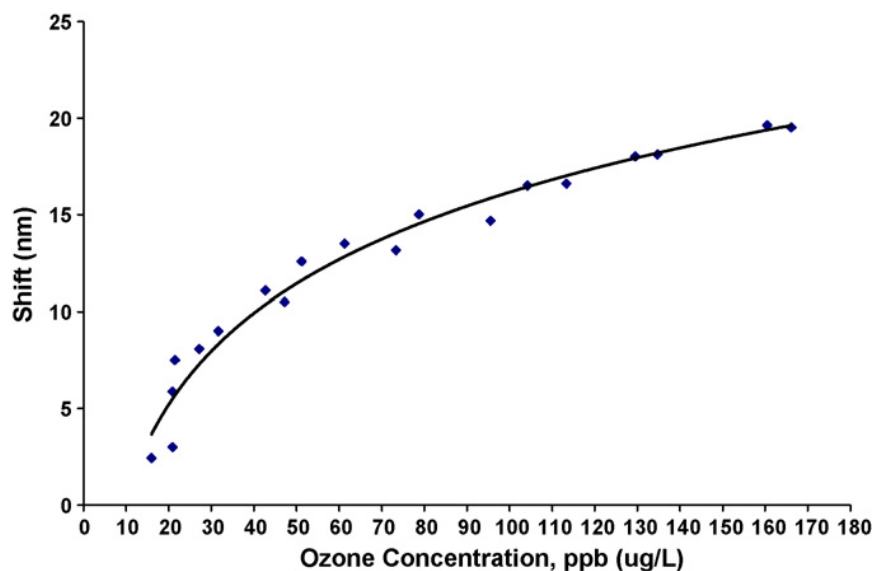


Figure 25- Shift in absorbed frequency from 520nm as a function of ozone concentration for 25nm gold nanoislands [33].

One final gas sensing scheme utilizes cantilevers arranged as a tuning fork with a gas-sensitive polymer coating. The resonant frequency of the cantilevers changes as the polymer coating absorbs or releases the target gas. The volatile organic compound sensor described earlier in this review uses this type of sensor, demonstrating its efficacy [34]. As the tuning

forks need to be coated with a polymer that can absorb and release a target molecule consistently without fouling and of a high enough concentration to adjust the resonant frequency, the challenge to bringing sensors based on this scheme to market lies in the polymer coating. Current research has produced sensors sensitive to benzene, toluene, and xylenes.

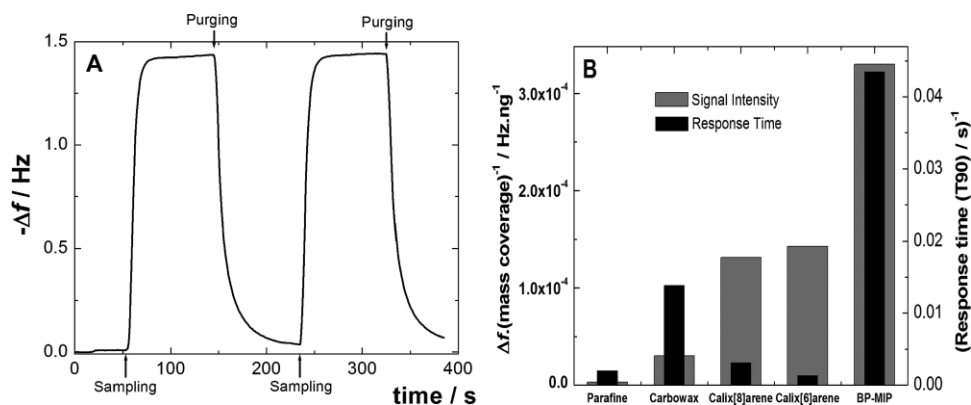


Figure 26- (A) Response of BP-MIP modified tuning fork to 40 ppmv toluene in air. Flow rate: 250 mL min⁻¹. (B) Mass normalized response and reciprocal of response for tuning forks modified with different polymers. Sample: 40ppmv toluene. Flow rate: 250mL/min. [34]

In addition to harmful gasses, particulates pose a health risk. Generally, particulates are grouped according to their size. The EPA lists maximum limits for two classes of particulates: PM_{2.5} and PM₁₀, corresponding to particulates with diameters less than 2.5 μm and 10 μm respectively. Particulate sensors generally operate by shining a laser across an air gap and recording the number of times the laser is scattered toward a photodiode. Air flow through the gap is maintained either by a pump or resistive heater. Laboratory grade sensors generally incorporate multiple stages and filter elements in order to provide more precise

measurements delineating the number of particles per size, while smaller, more general purpose sensors perform a simple count of anything large enough to trigger the photodiode.

Table 5- Commercially available dust and particle counters. ¹Requires additional 18" vacuum source.

Name	Part Number	Type	Method	Company	Voltage Range	Min Power	Min Energy	Cost per unit	Particle Sizes Detected
Compact Optical Dust Sensor	GP2Y1010AU0F	Dust Counter	IR laser reflection	Sharp	4.5V - 5.5V	55mW	550uJ	\$11.38	>0.1um – Highly imprecise
MET ONE 6000	6000	Particle Counter	Laser reflection	MET ONE	9V – 28V	3.3W ¹			0.5um
MET ONE R4800/R4900	R4800/R4900	Particle Counter	Laser reflection	MET ONE	6V	1.5W ¹			0.3um or 0.5um
PPD42NS	PPD42NS	Particle Counter	Laser reflection	Shinyei	4.9V - 5.1V	450mW	27J		1um or 5um
Air Quality Monitor	DC1100	Particle Counter		Dylos				\$199.99	0.5um or 2.5um

Accurate particle or aerosol sensing is not a perfect science. Even state-of-the-art counters designed for clean rooms and as references to validate filtration processes can be of variable accuracy for different particle sizes. For example, a study [35] in 2008 compared three different optical particle counters: a Model 1109 from Grimm Aerosol Technik, a Welas 2100 from Pallas, and the UKA A10 from the Karlsruhe Institute of Technology. The final measure of accuracy was counting efficiency, which was defined as the number of particles counted divided by the actual number of particles sent through the detector. It was found that many factors influenced the accuracies of the particle counters including size of the particle, refractive index of the particle, type of light used, orientation of the sensing chamber, and air flow rate through the sensing chamber.

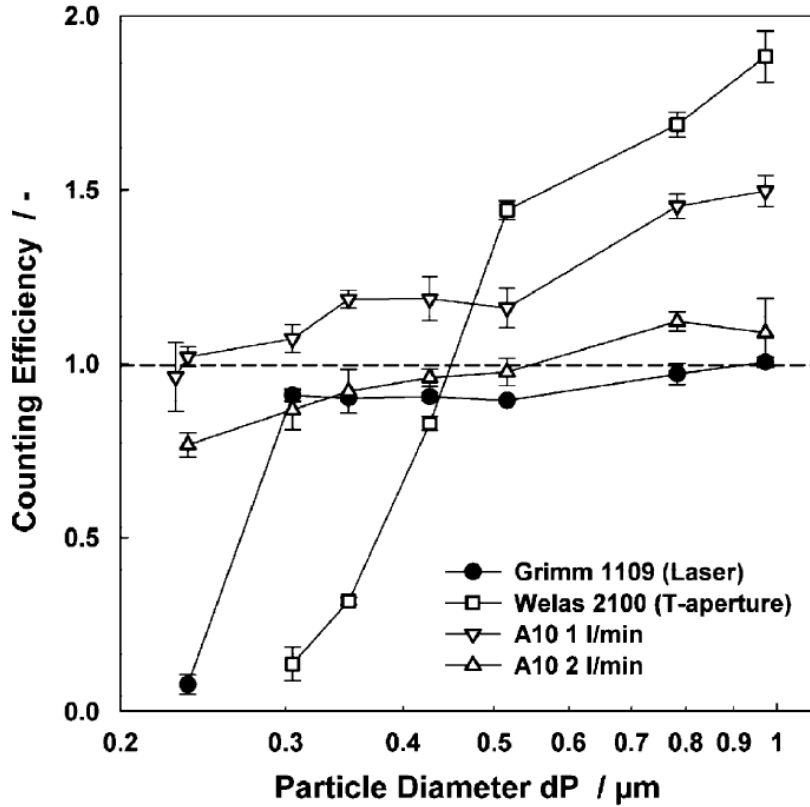


Figure 27- A comparison of three optical particle counters comparing counting efficiency (defined as the number of particles counted divided by the true number of particles passing through the sensing chamber) [35]. For the A10, two flow rates were tested.

Based on the results of this study, the manufacturers of the Welas counter improved their design to address some of the identified shortcomings. Their improved design, while better, still shows some error as per Figure 28. A comment was published as an update to the report in which the old and new particle counters were compared [36]. Examining these studies provides a starting point for considering the specific challenges faced when trying to perform accurate particle measurements.

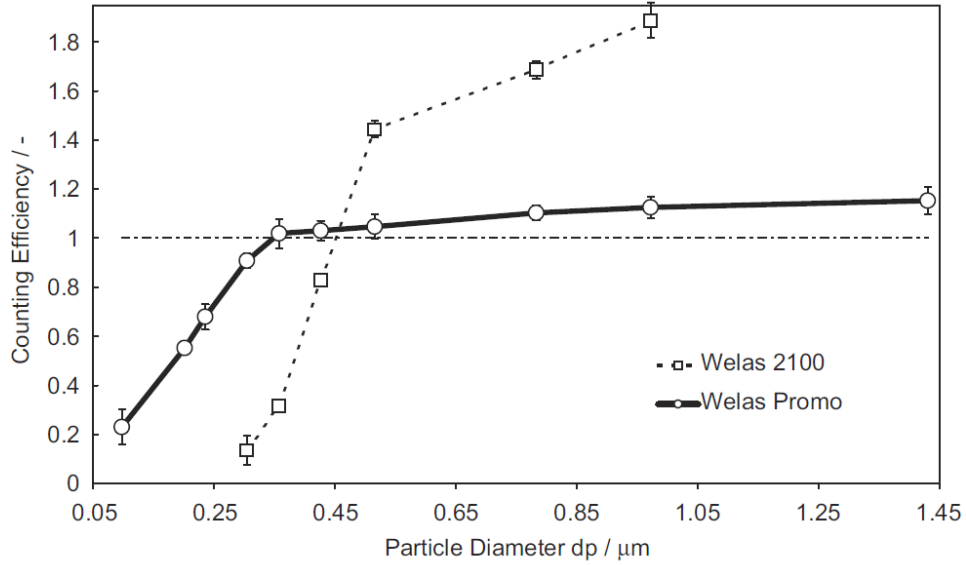


Figure 28- A comparison of the Welas 2100 and Welas 2100 Digital (Promo) showing improvements in counting efficiency and a lower minimum particle diameter threshold [36].

A sensor platform currently in development is the AirBot from the CREATE Lab at Carnegie Mellon University [37]. While the documentation for this platform is still somewhat light, it uses the standard laser scattering method that commercial sensors utilize, employs a small fan to induce the airflow, and reports the count of reflections seen during a defined interval. After integrating the AirBot’s signal to match the reporting periods, comparison to a MET ONE HHPC-6 shows a very similar dust profile shape, however order of magnitude differences in the number of particles counted demonstrates the need for further calibration.

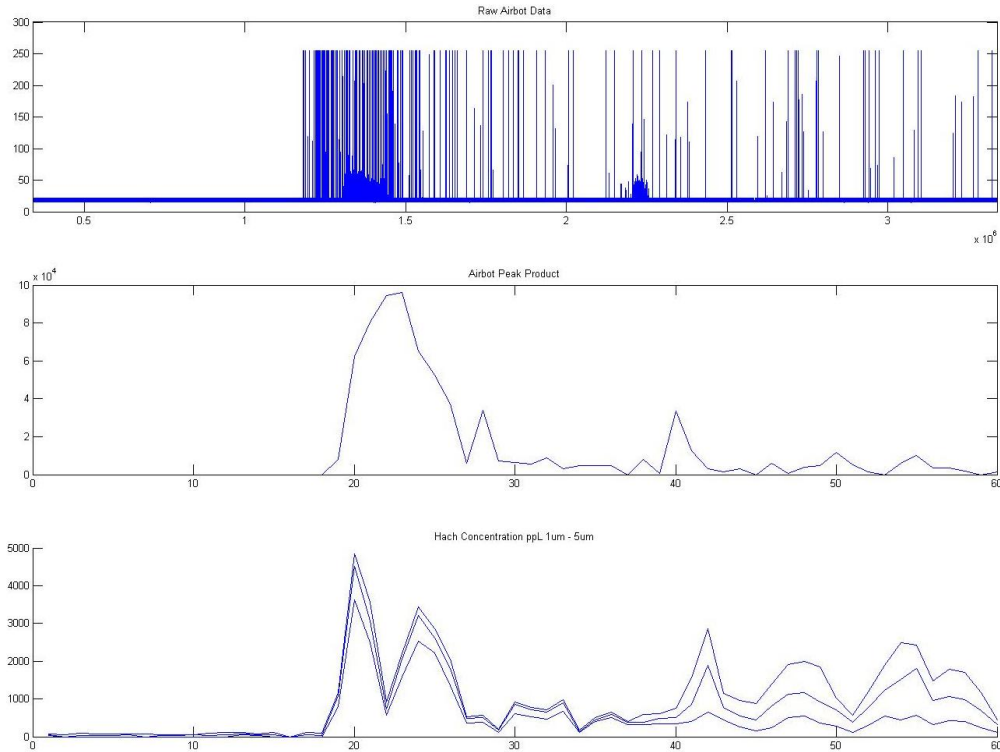


Figure 29- Comparative graph of two sensors: the Airbot research prototype and a commercial HHPC-6 from MET ONE. For the Airbot, specific particulate counts are shown (top) as well as the integrated total (middle). For the HHPC-6, the output (bottom) is used to validate the Airbot's integrated graph and provide a laboratory-grade baseline. [37]

The primary advances of the AirBot over other portable particulate counters lie in its size and power consumption. Whereas the HHPC-6 or the similar Dylos DC1100 are designed to be used in enclosed environments to detect problems with or verify the functionality of air purification and handling systems, the AirBot is tiny – smaller than a stack of playing cards – and is run off of an internal 900mAh Li-ion battery, allowing this sensor to be attached to a person and forgotten. An internal Bluetooth radio communicates with a base station, such as a mobile phone, to report particle counts with no user intervention.

2.4 Energy Harvesting & Storage

Power generation and energy storage are of great concern for this project. By placing this sensor platform in a brick as part of a building's thermal envelope, two primary power sources emerge: solar and thermal. Piezoelectric and RF energy harvesting were considered but determined to be of too low power density for this application. Additionally, no currently available energy harvester can provide a stream of power large enough to operate the gas and particulate sensors continuously. Therefore, various battery technologies are investigated alongside supercapacitors to provide energy storage.

Solar power generation is the most mature of the technologies utilized to power this project. Many research teams as well as the solar power industry are continuously looking for methods to improve the energy yield per area and per dollar. Photovoltaics operate on the principle that photons with energy values greater than a junction's band gap excite electrons sufficiently such that the electrons can jump the band gap, be harvested, and power a load. However, any energy from the photon greater than the band gap is lost to heat which contributes to a parasitic thermal current, reducing the usable power output. Hence, researchers and designers are faced with a tradeoff: either lower the band gap to create more lower-energy free electrons, or raise the band gap to create fewer higher-energy free electrons.

As a starting point for comparisons, Figure 30 is provided to illustrate the slow but steady rise in efficiencies for the various solar technologies. Commercial products rarely conform to the numbers provided in the figure, and generally lag by a few years. However,

as research has transitioned from purely academic to commercial R&D groups, more and more modules are becoming available to the general public that display efficiencies in line with the figure. One additional note: the efficiency of a cell is, by necessity, lower than the efficiency of a module. Modules combine many cells and require additional surface area, junctions, wiring, and bypass diodes; all of which slightly reduce the overall module efficiency.

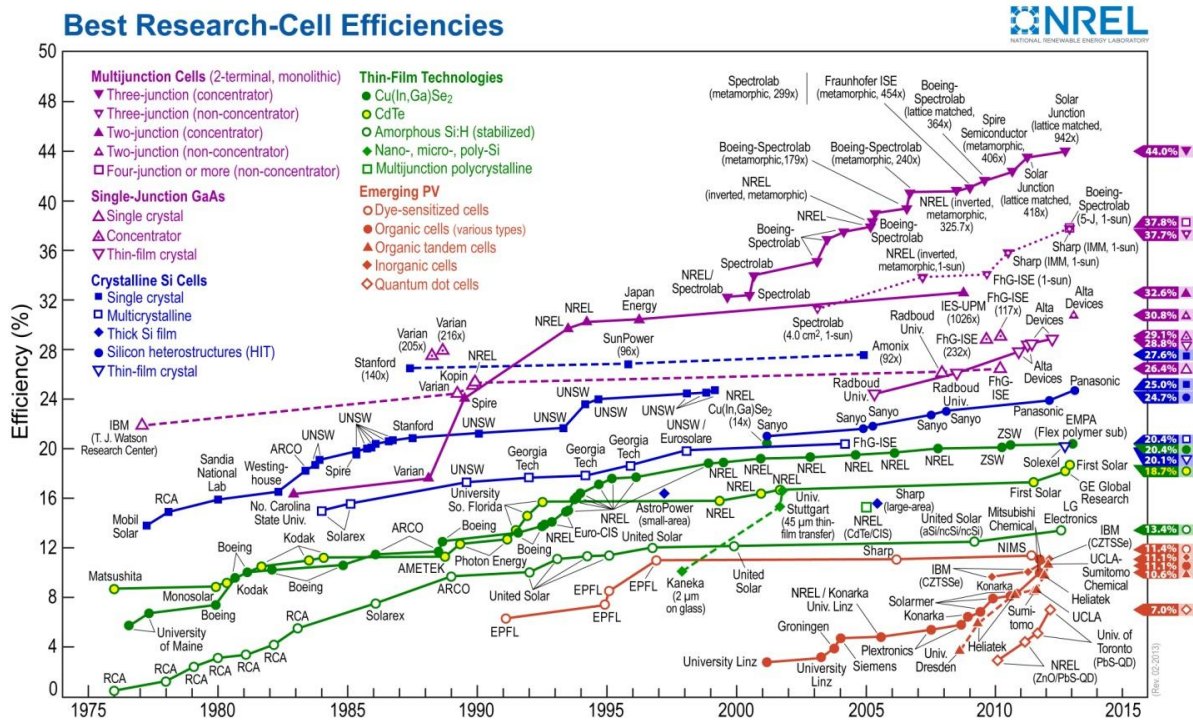


Figure 30 - Chart displaying the various types of photovoltaic technologies, peak research-cell efficiencies, responsible group, and date of achievement [38].

At the top of the list are three-junction cells using light concentrators from Solar Junction. This is a commercial enterprise, and production units are available that utilize the listed 44.3% efficient cells. A secondary company, Semprius, has produced modules utilizing these cells with overall efficiencies of 33.9%, demonstrating the reduction in overall efficiency from cells to modules. These three-junction cells convert light of three different wavelengths into usable energy, improving efficiency in two distinct ways. First, lowering the minimum band gap widens the range of useful photon energies. Second, by utilizing junctions with different band gap energies, the excess energy from a photon above the next highest band gap is reduced as compared to a comparable system with only one junction. However, these cells are expensive to produce and are generally only economically viable if solar concentrators are used, such as Fresnel lenses that focus sunlight 400 to 1000 times the ambient value onto the cell. [39]

Single junction cells are much more prevalent overall, both in research and commercially. Crystalline silicon cells comprise a very large fraction of the single junction cells. The Mono X LG260S1C-G3 is an example of a module comprised of many monocrystalline silicon cells from LG Electronics. At 16.2% module efficiency (17.8% cell efficiency), this device is not the most efficient monocrystalline device, however it is representative of the more advanced economical models [40].

Another technology often used is amorphous silicon. Amorphous silicon is part of the thin film family of photovoltaics which, though generally producing relatively low efficiency numbers, promise economical viability through reductions in production costs. For example, the CBC-PV-01 photovoltaic cell from Cymbet produces $161\mu\text{W}$ under 200 lux

of fluorescent light (approximately 2.3mW across the surface of the cell). This yields an efficiency of between around 7%, depending on the specific fluorescent light used [41].

Thermal power generation is, by comparison, underdeveloped. Thermoelectric generators operate via the Seebeck effect in which a temperature differential between the junctions of dissimilar metals or semiconductors directly produces an electric potential. Overall device efficiency is related to the temperatures of the hot and cold sides of the generator, the Seebeck coefficients of the materials used, electrical conductivities, and inverse of the thermal conductivities. The ZT figure of merit encapsulates these material properties into a convenient number and, once adjusted to an operating temperature regime, various thermoelectric generators can be compared. Research in this area generally follows along two paths – increasing electrical conductivity or decreasing thermal conductivity – and within one of only a few temperature regimes – approximately room temperature, combustion waste heat temperatures, and focused thermal collection temperatures. For the purposes of this project, only room temperature thermoelectric generators were investigated.

The physical design of most thermoelectric generators is the same – arrays of short p and n type legs are sandwiched between thermally conductive plates. The thermal potential transfers from one plate to the other with the array of legs between creating multiple parallel paths. Electrically, each leg has a contact on each end, and each contact is connected to two legs creating a series arrangement such that the small voltage potentials of each leg add to all the other legs. For most TEGs, the legs are 1mm long or longer, resulting in total thicknesses of 2 to 5mm.

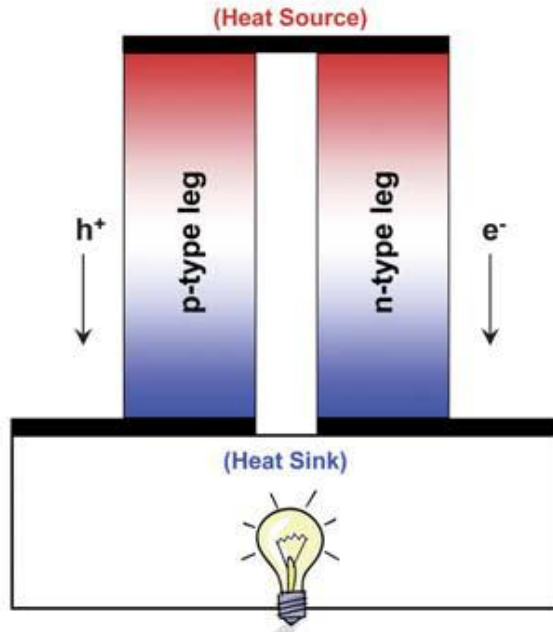


Figure 31 - Basic layout of a Thermoelectric Generator demonstrating the physical layout of n- and p-type legs placed between a heat source and heat sink with current flowing from the n-type leg to the p-type leg. [Enhancement of the]

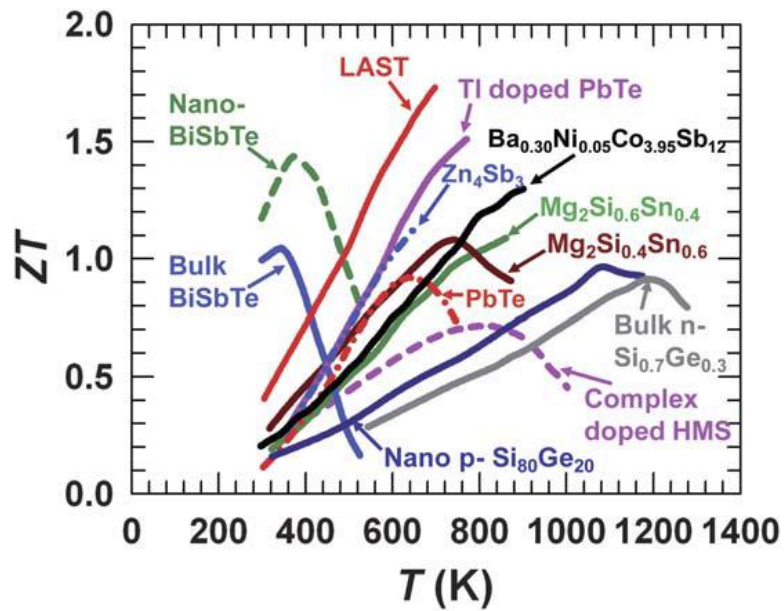


Figure 32- Comparison of figure of merit, ZT , for various temperatures and multiple thermoelectric materials. [42]

Most commercial thermoelectric generators are composed of chalcogenides: bismuth telluride or lead telluride [43, 44] with p or n type dopants and controlled impurities. While PbTe is generally associated with a higher peak ZT, these operate best at relatively high temperatures on the order of combustion waste heat. From Figure 32, BiTe has a slightly lower peak ZT, but is centered on room temperature. Bismuth chalcogenide composites (BiSbTe) maintain roughly the same operating temperature regime as BiTe, but with much higher ZT.

Most commercially available TEGs for low temperature operation utilize bulk BiTe legs. Through changes in leg and plate geometry and varying the number and orientation of legs, manufacturers have produced a wide variety of TEGs as shown in Table 6.

Additionally, as improvements over bulk BiTe are being discovered and implemented, comparisons between TEGs can become quite confusing. A simple metric for comparison is the output power per unit area of the overall plate dimensions (Watts/mm^2) with a set temperature across the plates. This ignores the variance in ZTs with changing average temperature, and as such should not be relied upon outside of the realm of similar technologies and similar temperature regimes. Incorporating the temperature differential into the metric ($\text{Watts}/[\text{mm}^2 \cdot \Delta T^2]$) provides a very rough number from which an approximate output power can be calculated given an area and hot and cold side temperatures.

Utilizing nanocomposites, researchers have been able to push the ZT for bismuth chalcogenides up to 1.2 for room temperature operation, with a peak of 1.4 around 100C, by fabricating the pellets such that there is no common grain in the crystal. By hot pressing milled BiTe and SbTe powder into pellets, inclusions are formed along grain boundaries.

These inclusions significantly limit the mean distance a heat-carrying phonon may travel while only posing a minor hindrance to electrical conduction. [42]

Table 6- Comparison of currently available bulk Bismuth Telluride Thermoelectric Generators listing the surface area of one side, power output at various temperature differentials, cost, power per unit area, cost per power, and power per unit area per temperature differential. All data gathered from datasheets.

Bulk BiTe								
Part Number	Area (mm ²)	Power Output (mW)	@	ΔT (K)	Cost	Power/Area (mW/mm ²)	Cost/Power (\$/W)	W/(mm ² * ΔT^2)
Company								
1261G-7L31-04CL	900	1040		100	\$30.00	1.16	\$28.85	0.000115556
Custom Thermoelectric	900	5190		270	\$30.00	5.77	\$5.78	7.91038E-05
1261G-7L31-04CQ	1600	1010		100	\$50.00	0.63	\$49.50	0.000063125
Custom Thermoelectric	1600	5100		270	\$50.00	3.19	\$9.80	4.37243E-05
1261G-7L31-05CQ	1600	1150		100	\$50.00	0.72	\$43.48	0.000071875
Custom Thermoelectric	1600	7150		270	\$50.00	4.47	\$6.99	6.12997E-05
1261G-7L31-10CX1	3136	3240		100	\$79.50	1.03	\$24.54	0.000103316
Custom Thermoelectric	3136	14700		270	\$79.50	4.69	\$5.41	6.43004E-05
1261G-7L31-24CX1	3136	3540		100	\$79.50	1.13	\$22.46	0.000112883
Custom Thermoelectric	3136	19100		270	\$79.50	6.09	\$4.16	8.35468E-05
TEG1-12610-5.1	1600	1000		100	\$47.00	0.63	\$47.00	0.0000625
TECTEG	1600	5100		270	\$47.00	3.19	\$9.22	4.37243E-05
TEG1-12611-6.0	3136	3100		100	\$75.00	0.99	\$24.19	9.8852E-05
TECTEG	3136	14600		270	\$75.00	4.66	\$5.14	6.3863E-05
TEG1-12611-8.0	3136	2700		100	\$100.00	0.86	\$37.04	8.60969E-05
TECTEG	3136	13000		270	\$100.00	4.15	\$7.69	5.68643E-05
TEG1B-12610-5.1	1600	1300		100	\$49.00	0.81	\$37.69	0.00008125
TECTEG	1600	7100		270	\$49.00	4.44	\$6.90	6.08711E-05
TEG1-1263-4.3	900	1000		100	\$30.00	1.11	\$30.00	0.000111111
TECTEG	900	5200		270	\$30.00	5.78	\$5.77	7.92562E-05
TEG1-1268-4.3	1225	1000		100		0.82		8.16327E-05
TECTEG	1225	5200		270		4.24		5.82291E-05
TEG1-12610-4.3	1600	1100		100	\$48.00	0.69	\$43.64	0.00006875
TECTEG	1600	5200		270	\$48.00	3.25	\$9.23	4.45816E-05

Superlattices of alternating layers of BiTe and SbTe have also shown increased ZT (>2) through the use of phonon scattering. These account for the high energy densities from the Nextreme Company in Table 7. [45]

Table 7- Comparison of currently available Thermoelectric Generators built from a superlattice of Bismuth Telluride and Antimony Telluride listing the surface area of one side, power output at various temperature differentials, cost, power per unit area, cost per power, and power per unit area per temperature differential. All data gathered from datasheets.

BiTe & SbTe Superlattice								
Part Number	Area (mm ²)	Power Output (mW)	@	ΔT (K)	Cost	Power/Area (mW/mm ²)	Cost/Power (\$/W)	W/(mm ² * ΔT^2)
Company								
HV14	1.5	9		50	\$50.70	6.00	\$5,633.33	0.0024
Nextreme	1.5	33		100	\$50.70	22.00	\$1,536.36	0.0022
	1.5	101		200	\$50.70	67.33	\$501.98	0.001683333
HV37	4.2	1		10	\$81.98	0.24	\$81,980.00	0.002380952
Nextreme	4.2	24		50	\$81.98	5.71	\$3,415.83	0.002285714
	4.2	90		100	\$81.98	21.43	\$910.89	0.002142857
HV56	6.4	1.5		10	\$102.98	0.23	\$68,653.33	0.00234375
Nextreme	6.4	36		50	\$102.98	5.63	\$2,860.56	0.00225
	6.4	130		100	\$102.98	20.31	\$792.15	0.00203125

Overlapping photovoltaic power generation and thermoelectric power generation are three fields of research: one stacks a PV module on top of a TEG so that the waste heat generated from the PV can be utilized by the TEG; a second uses heat to create photons within the energy band for which a specially-designed PV cell is most efficient; and the last uses a solar absorber to convert incident light into heat in order to power a specially-designed TEG. Solar thermionic generators operate in a similar manner to these solar/thermal hybrids, but utilize a different mechanism for electron generation, and are briefly discussed.

The concept behind a PV-TE (layering a TEG underneath a PV module) is simple. PV modules produce electricity when illuminated, however due to inefficiencies and mismatches between incident photon energies and band gaps, some of the photons are converted into heat. As the cell temperature rises, its efficiency decreases, further raising the temperature. A standard PV module attempts to maintain the lowest temperature possible by releasing this heat to the atmosphere or some other heat sink. Placing a TEG against the PV module allows some of that waste heat to be converted into electricity, as long as the cold side of the TEG can still shunt waste heat away. The caveat to this is that the TEG is not as effective at removing heat from the PV module as a direct connection to a heat sink would be, thereby keeping the PV at a higher temperature than it would be at otherwise. Herein lies the tradeoff: either produce more electricity from a PV with no TEG, or produce a little less from the PV and a little additional from a TEG. A recent study developed a model of a PV-TE system showing a gain of 8 to 23% over a pure PV system, however significant assumptions were made that, if false, will lessen those gains. Also, as noted in the report, the cost for the TEG portion of the system would be approximately 10x the cost for the PV portion of the system. [8]

Thermal photovoltaics (TPV) utilize a two or three step process to create electricity. The first and last steps are always the same. First, a heat source heats an element called an emitter that most efficiently produces photons in a narrow range of wavelengths. Last, a PV cell with a bandgap slightly below the average energy of the photons coming from the emitter converts the light into electricity. Optionally, a middle filter stage can be included that reflects photons that are not within the most efficient range of the PV cell back to the

heat source. The filter will decrease system efficiency by absorbing a small percentage of the photons passing through it, but also increase efficiency by reflecting photons outside the allowable energy band back to the emitter where they can be reabsorbed and reemitted. Most TPV systems operate at temperatures greater than 1000°C which requires optical concentration and solar tracking systems. [46]

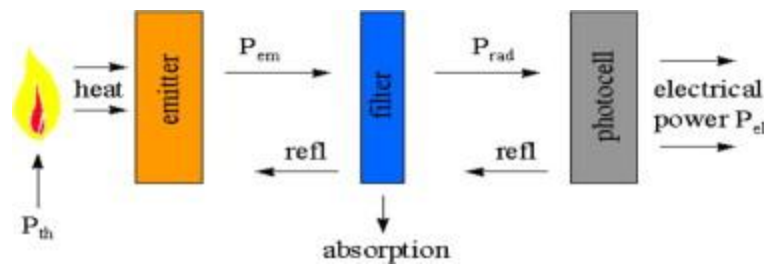


Figure 33 - Illustration of the principle of a TPV system in which a heated emitter creates photons that the photocell converts into electrical power. An optional filter removes photons that would otherwise be converted to heat in the photocell. [46]

Solar thermoelectric generators (STEGs) are standard TEGs optimized to work with heat provided by solar energy. A solar absorber is placed on the hot side of the TEG that will convert light into heat, which can be extremely efficient. If the solar absorber is kept in a vacuum, eliminating heat losses through conduction and convection to the ambient air, efficiencies for converting light to heat and providing that to the TEG can be in the range of 70 to 80%. Optical concentrators can be included to increase the energy available. Including BiTe TEG efficiencies of around 7%, the whole system can be up to 5% efficient, which is comparable to some PV systems. [24]

A similar technology currently being researched is solar thermionics. Thermionic emission of electrons is accomplished through heating an electrode to temperatures in excess of 1700°C. However, this electrode needs to be highly electrically conductive, and due to the relatively high thermal conductivity of conductors, a heat source with a high energy density is required to overcome the heat lost to the surrounding material. Carbon nanotubes have been shown to have a “Heat Trap” effect in which increased temperature reduces the thermal conductivity in a positive feedback loop that effectively locks the heat into one spot. Researchers have exploited this phenomenon to demonstrate a thermionic emission process utilizing incident solar irradiance as the heat source with 5100x optical concentration. However, the prototype unit only produced ~16μW, and would require a solar tracking system to be viable. [47]

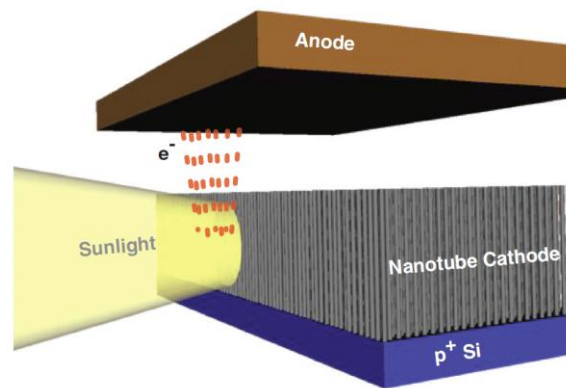


Figure 34 - A schematic representation of a solar powered thermionic electron source. The forest of nanotubes was grown on a highly doped silicon wafer and placed below a simple metallic anode. Focused sunlight directed at the side of the nanotube forest provided heating, which was further concentrated by the “heat island” effect of the nanotubes themselves. [47]

With each of these energy generation methods, the IV curves are non-linear and therefore require energy harvesting controllers to ensure that the maximum amount of power is being extracted at all times. Also, as the maximum power points change, with voltages varying accordingly, these production methods do not lend themselves to straight-forward storage in either batteries or capacitors, and instead require maximum-power-point trackers and DC-to-DC power transformation prior to storage. Advances in DC power conversion have recently reduced the losses to a point that milli-, and in some cases micro-, Volts can be accumulated, buffered, and transformed to the 2 to 3 Volts necessary to be stored in current supercapacitors and Li-ion batteries. A fully capable energy harvester includes three distinct systems: an AC-to-DC or DC-to-DC transformer to rectify, boost, or buck (or some combination of the three) the incoming power; a maximum power point tracker (MPPT) to control the energy extractor in order to follow the non-linear power curves of the generators, ensuring the maximum Watts are extracted; and a battery management unit to handle charging the batteries or capacitors and ensure no specifications are exceeded. Depending on the system for which the energy harvester is used, an additional DC-to-DC transformer may be incorporated to raise or lower the voltage of the stored energy for use by the payload sensors and electronics, as per Figure 35. [48]

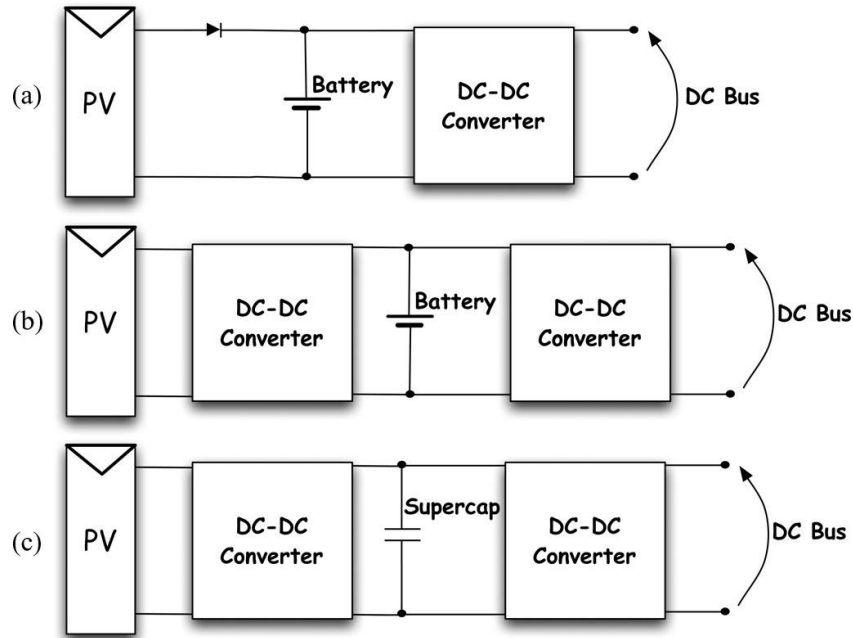


Figure 35 - Block diagrams representative of modern energy harvesting systems. The MPPT and battery management unit are left out of (a), with the diode serving as the simplest form of an energy extractor. With (b) and (c), various energy storage mediums can be tested allowing for simple comparison and evaluation. [48]

Most energy harvesters on the market today consist of a DC-to-DC converter, generally either a buck or a boost converter, which is designed for one specific type of power source and one specific type of energy storage mechanism. Due to switching losses and parasitic resistances, the efficiency of DC-to-DC converters varies significantly depending on the input and output voltages. Although many energy harvesters have inputs for two or more power sources, only one has been found on the market that is designed for multiple types of power sources. To clarify, many energy harvesters have multiple inputs for various power sources, but with all the various inputs tied to the same input line for the DC-to-DC converter. Cymbet Corporation provides an evaluation kit with separate inputs for PV, RF, thermoelectric, and piezoelectric energy generators in which each of the inputs is tied to an

appropriate converter as per Figure 36 [49]. While this is a better design than tying multiple sources into the same converter, this one-size-fits-all approach can be improved upon. Given the low energy densities for energy harvesting power sources, the converters transforming this power into something that can be stored should be of the highest efficiency possible, which tends to require converters that are custom-designed for the power source and storage medium.

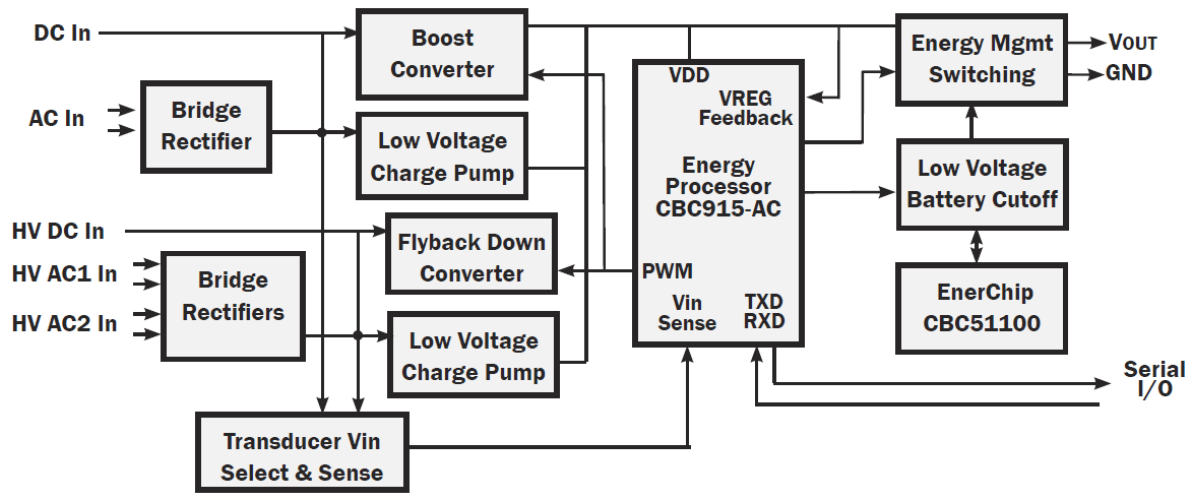


Figure 36 - CBC-EVAL-09 Energy Harvester block diagram. Five separate inputs are provided: DC in for a photovoltaic source, AC in for an electromagnetic or radio frequency source, HV DC in for a thermoelectric source, and two HV AC ins for piezoelectric or vibration sources. [49]

Lithium-ion batteries are currently the main storage medium utilized when weight or volume is at a premium. Their high energy density (200-280Wh/L, 90-115Wh/kg) combined with relatively good charge/discharge cycle life (500-1000 cycles) have made them attractive solutions for many applications in which volume, weight, or lifetime are significant design

criteria. [50] However, charging circuits for Li-ion batteries are complex, and premature battery failure can occur if charging is not accomplished properly. Charging generally consists of two separate phases: a constant current phase that brings the battery up from depleted to approximately 70% of full charge, and a constant voltage phase that adds the final 30% of the charge. [48]

Improvements are still being made in increasing energy density, cycle life, and safety. Experiments are underway with many anode, cathode, and electrolyte materials with varying levels of success. Incorporating composites of silicon nanoparticles and reduced graphene oxide into the anode can significantly increase the energy density up to 2,100mAh/g during the first charge/discharge cycle; although at 500mA/g approximately half of this capacity is lost by the 70th cycle [51]. Conversely, coating the cathode with AlF₃ can increase the capacity retention to 86.2% after 1000 cycles for Li[Ni_{0.8}Co_{0.15}Al_{0.05}]O₂ cathodes at 190mA/g [52]. Ionic liquids can be used as the electrolyte in order to reduce the risk of combustion as well as improve conductivity and cycle lifetime. Mixing PP₁₄-TFSI and TMS results in an electrolyte with excellent combustion resistance, with 0.001S/cm conductivity, and that retains 81% of its discharge capacity after 50 cycles [53].

Another promising line of research looks toward replacing the Li-ion battery itself. A lithium/sulfur battery could theoretically hold more energy per weight than a Li-ion battery by a factor of 5. However, significant problems have prevented this technology from reaching the market, namely a short cycle life, low charging efficiency, poor safety, and a high self-discharge rate. Many groups are looking at different ways to address these issues, and while progress is being made, these batteries are years from being consumer-ready. [54]

Supercapacitors offer an alternative to batteries with a much longer cycle life, but greatly reduced energy density. Two types of supercapacitors have been created: double-layer electrostatic capacitors and redox pseudocapacitors, with the redox pseudocapacitors further divided between polymer and metal oxide. [55] Commercially available supercapacitors are generally of the double-layer variety. Available in sizes up to a few thousand Farads, this technology is capable of replacing batteries in certain applications. However, shortcomings still exist limiting where these may be employed, namely low energy density, and a small but significant leakage current. [56]

Double layer electrolytic supercapacitors store energy as charge separations between the electrolyte and the highly porous carbon anode and cathode. Advances in this technology are generally centered on improving the electrolyte or increasing the surface area of the anode and cathode. Carbon is integral to the electrolytic supercapacitor as both the anode and cathode, however the form of the carbon molecule is highly important with treated biochar, activated carbon, graphene, activated graphene, and titanium carbide ranging in specific capacitance from 260 to 102 F/g, respectively. [57] The maximum voltage that the supercapacitor can maintain is limited by the electrolyte, with organic electrolytes being capable of higher voltages (2.3V - 2.75V) than aqueous electrolytes (1V). [58] Ionic liquids have been shown to support up to 3.7V, with a general rule being that the greatest gains are found when electrolyte ion size is matched to the electrode pore size. This 1V increase approximately doubles the energy storage of the supercapacitor. [59]

Redox pseudocapacitors store energy in charge transfers between the electrolyte and either an electrically conductive polymer (ECP) or metal oxide, effectively sitting in a middle

ground between batteries and capacitors. Like batteries, these charge transfers require chemical changes in either or both the electrode or the electrolyte. Like capacitors, the storage and release of electrical energy can be accomplished quickly and repeatedly. For polymer supercapacitors, electrodes of ECP store charge by altering the overall p- or n-doping of the polymer. Metal oxide supercapacitors are based on the transfer of a proton between two ruthenium oxide-based electrodes. [55]

Charging supercapacitors is a somewhat more straightforward process than Li-ion batteries. Whereas the cycle life and safety of a battery are highly dependent upon the charging method, with optimum charging requiring time-varying current sources, state of charge calculations, and approximations to determine when charging should end, a supercapacitor needs a minimum of a current limiter and overvoltage protection. A diode may suffice as the charger for some energy sources, as per Figure 35(a), however the energy source's full expected range of behavior must be within the supercapacitor's tolerances, and the efficiency of the system will be abysmal. [48] A better charger consists of a DC-to-DC converter that acts as a constant current source. Energy is temporarily stored in an inductor with switches closing to allow the energy source to charge the inductor and opening to allow the inductor to charge the supercapacitor. Current limiting is accomplished through setting a maximum time for which the switches will be closed. Overvoltage protection is accomplished by preventing the switches from closing when the supercapacitor reaches a set voltage. [60]

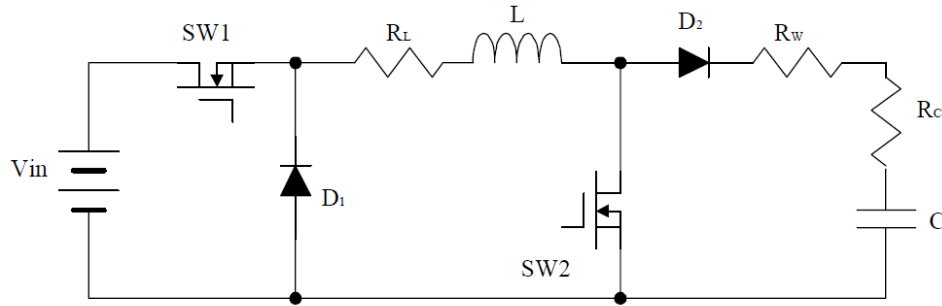


Figure 37 - Circuit diagram for a simple supercapacitor charger. When SW1 and SW2 are closed, current through L increases, storing energy. When SW1 and SW2 open, D1 and D2 begin to conduct, charging the supercapacitor. [60]

Finally, in an attempt to overcome the limited cycle-life of Li-ion batteries and low energy density of supercapacitors, a combined battery/capacitor system has been demonstrated. In order to combine the best parts of a supercapacitor with a Li-ion battery requires overcoming the naturally-occurring variations in power output found in every energy harvester. If system lifetime is the primary driving factor, battery cycling must be kept to a minimum, forcing maximum use of the supercapacitor. Obviously, increasing the size of the supercapacitor will reduce how much the battery is used as shown in Figure 38, however supercapacitors have a significant leakage current that increases with size. Therefore, the most efficient design would be one in which the size of the supercapacitor is minimized but large enough to prevent the battery from expending its cycle life, plus a reserve, prior to the expected lifetime of the system. Producing the algorithm that provides this result is multifaceted. First, the energy harvester must be modeled, including non-ideal behavior, weather events, variations in temperature, and other outside factors. Including the expected system energy requirements provides an approximation of how much energy must

be stored. Incorporating a MPPT is a necessity and allows for simpler control circuitry in the battery and supercapacitor management. Due to the MPPT, source current and voltage will vary in an approximately linear fashion. Given that the battery must initially be charged with a constant current, which cannot be guaranteed with the energy source alone, the supercapacitor is charged first. When the supercapacitor reaches a predetermined voltage, the battery charging circuitry turns on, allowing the energy source and supercapacitor to work together to charge the battery. The system is preferentially powered by the supercapacitor, with the battery used mainly to recharge the supercap when the energy source is not enough. Figure 38 clearly shows the reduction in total number of battery charge/discharge cycles with increasing supercapacitor size. These results are highly dependent upon the system being utilized and must be scaled appropriately for other applications. [48]

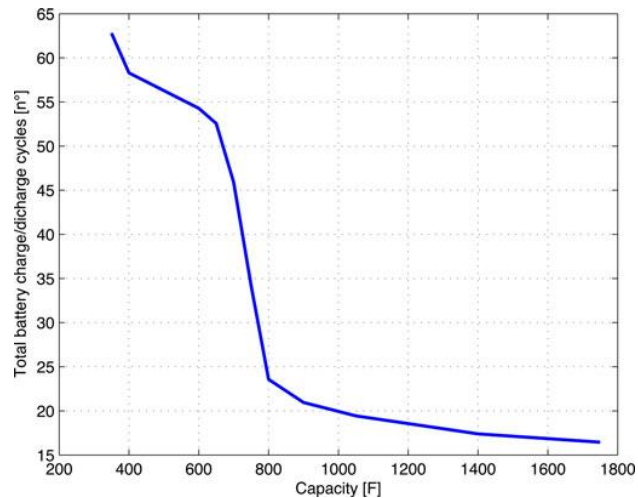


Figure 38 - Graph comparing the total number of charge and discharge cycles a Li-ion battery can be expected to be subjected to when combined with a supercapacitor of a certain size. Given the maximum number of cycles for a battery and the designed lifetime for this system, a supercapacitor can be chosen. [48]

Chapter 3 – Experimental Procedure

The goal of this research is to produce a Lab-in-a-Brick. As stated earlier, a systems approach was taken, breaking the design up into five general sections: energy harvesting, energy storage, gas and particulate sensing, low power computing and data storage, and low power wireless data transmission. Overall system requirements set the tone for the project, while goals set internally to each section guided the component selection process.

- Low power microcontroller with data storage and sensor interface
- Low power radio with minimum 3m range
- Energy storage medium with more than 20 years functional life
- Gas and particulate sensors appropriate for health monitoring
- Energy harvesters capable of powering at least one round of sensing events per day

In order to create the whole brick, each of the five sections was investigated in turn iteratively. Initially a broad survey of available components was conducted. When the results of this survey for any one category established a system constraint, the constraint was applied to each of the other categories until components were chosen that accomplished all the system goals. Many passes through all the system components were required before a full system could be developed that fulfilled all the requirements.

Microcontroller survey results and constraints:

- Various input voltages from 1.5V to 5V
- External memory units likely unnecessary
- Integrated ADCs common
- Serial bus appropriate for radio interface ubiquitous

Radio survey results and constraints:

- Proprietary, Bluetooth, and ZigBee options
- Little functional difference between types

Energy storage survey results and constraints:

- Only supercapacitors fulfill lifetime requirement
- No need for complex charging circuits
- Must include a DC-DC transformer for constant voltage loads while charging/discharging

Sensor survey results and constraints:

- Form factor and lifetime limits gas sensors to resistance heater type
- Must include humidity sensor for gas sensor calibration
- Must include temperature sensor for humidity sensor calibration
- Relatively massive power needs relegated other loads to being nearly negligible

Energy harvesting survey results and constraints:

- Many small photovoltaic systems available
- Thermoelectric energy harvesting untested in this application

3.1 Component Selection and Testing

Low Power Computing and Data Storage

It was assumed that finding a low power microcontroller would have the fewest options and therefore a good place to begin. The requirements for this component were as follows:

- Low power energy use while on
- Ultra low power energy use while in standby or ability to be duty cycled while maintaining memory
- ADC for sensor measurement, preferably but not necessarily integrated
- Ability to store days worth of sensor readings

The MSP430 line of microcontrollers from Texas Instruments are billed as ultra low power and included many features that made them the most appropriate choice for this project. Firstly, the wide rated voltage input range (1.8V to 3.6V) lent itself to the intermittent energy production regime of energy harvesting and fit within the varying voltages of supercapacitor energy storage. Secondly, while the power requirement while active is extremely low (approximately 600 μ W), multiple lower power modes are available depending on what oscillators, interrupts, or memory need to be maintained. Thirdly, the integrated ADC with 1.5V and 2.5V internal reference voltages and various input pins allowed for straightforward sensor integration.

The eZ430-RF2500-SEH kit was chosen to be the starting point for all further work. This kit included not only an MSP430F2274 microcontroller which fulfilled the need for low power computing with a small amount of data storage but also the CC2500 low power radio, a small solar panel, energy harvesting circuit, and battery/capacitor unit for energy storage [61]. The MSP430F2274 microcontroller and CC2500 radio were integrated onto the same PCB, the eZ430 package, with all requisite supporting hardware as well as code examples, greatly simplifying the communication portion of the project. Eighteen IO pins, fifteen usable, on the microcontroller PCB provided the sensor interface options and set restraints that both simplified the sensor selection process while simultaneously complicating the overall system design. The solar panel, energy harvester, and energy storage devices were combined onto a separate PCB with various breakout pins and customization options for additional IO devices or energy generation, allowing for easy customization or complete replacement.

Little specific testing was performed on the microcontroller beyond basic input voltage limitation measurements. Instead, the eZ430 was utilized throughout the design and construction process as a measurement tool, verifying its operation through use. The input voltage testing showed proper operation below the datasheet minimum value, but with certain limitations. Applying a slowly increasing voltage to the eZ430 input would often not turn the system on until nearly 3V had been reached, as per the brownout reset circuitry. Given the intermittent nature of energy harvesting, it was decided to retain the energy harvesting and storage portion of the eZ430-RF2500-SEH kit purely to ensure proper eZ430 operation.

The 10 bit ADC performed well. Integer math performed on a resultant measurement required forethought to ensure that overflows were avoided. Also, due to voltage range limitations in the gas sensor signals, it was possible to retain the resolution of the 10 bit ADC in an 8 bit value through level-shifting and scaling the result to exclude impossible values.

Data storage in the eZ430 was by no means vast. The MSP430F2274 contained 1kB of RAM, however each full set of sensing events required only 27 bytes. Assuming an energy-generous 10 full sensing events per day, over three days of data could be stored.

Overall, the eZ430-RF2500-SEH kit fulfilled the primary system requirements and imposed only modest restrictions:

- Maximum storage of 1kB of measurements
- 15 IO pins, 10 accessible by the ADC, plus V_{CC} and GND

3.2 Wireless Data Transmission

In choosing the eZ430-RF2500-SEH, the signaling regime, hardware, and basic software for the wireless data transmission scheme were also set. The CC2500 radio integrated into the eZ430 package utilized the proprietary low power SimpliciTI protocol for data transmission, operated on the 2.4GHz band, and claimed a range of up to 50 meters under laboratory conditions [62] – all components similar to ZigBee or Bluetooth radios.

These qualities exceeded the admittedly relaxed minimum requirements:

- Half-duplex communication
- 3m range

Testing was performed to determine both the amount of energy required to send a message as well as the robustness of communication. To determine the amount of energy required, a 1Ω resistor was placed in line with V_{CC} to the eZ430. A known message was sent consisting of two pings and four frames of data. The voltage drop across the resistor and timing was measured to calculate overall energy use and energy per bit. As can be seen in Figure 39, activating the radio resulted in a pulse at around 9ms with the first ping being sent from around 11ms until 12ms. The radio transitioned to receiving and waited from 12ms until 15ms. A second ping & receive event occurred between 16ms and 20ms. Finally, the four data frames began around 24ms and completed around 42ms. Each of the four data frames consisted of 9 bytes of data. It was notable that the energy use of the eZ430 increased noticeably when the radio was awakened, even when not being used to send or receive data.

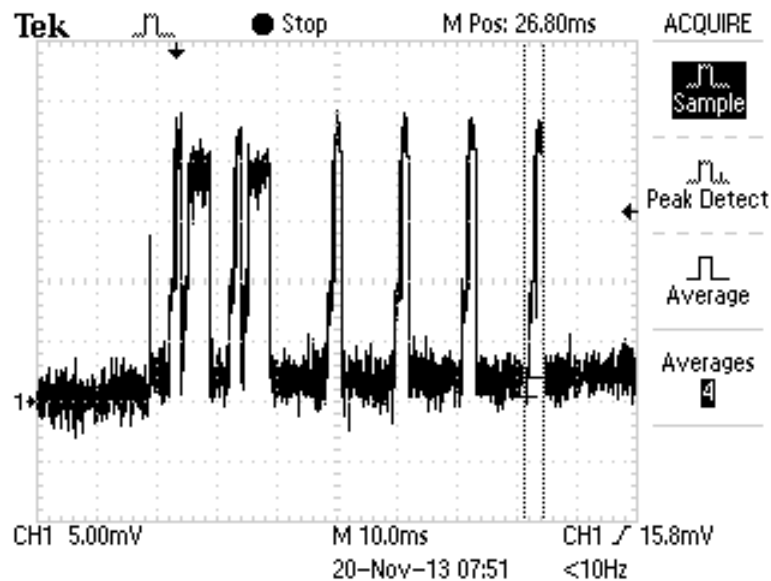


Figure 39 - Oscilloscope display showing the voltage across a 1.067Ω resistor place in series with the eZ430 while transmitting a sample data set.

Taking into account that the voltages shown on the oscilloscope screen capture are across a 1Ω resistor (1.067Ω), Ohm's law was used to determine the current through the resistor. Power utilized by the eZ430 was then calculated for each event: microcontroller on but radio off, both microcontroller and radio on, both on with the radio sending, and both on with the radio receiving. The baseline power drawn for the eZ430 rose by 4.20mW , from $821\mu\text{W}$ to 5.02mW , when the CC2500 was activated. A transmission event consisted of three distinct segments: two lower power stages in which the frame was prepared, and one final higher power stage in which the frame was sent. The first two stages were independent of the length of the message and drew 15.8mW and 37.3mW for $800\mu\text{s}$ and $480\mu\text{s}$, respectively. The final transmit stage drew a set amount of power but for a time directly proportional to the length of the message plus a small header: 45.4mW for $960\mu\text{s}$, which corresponded to 9 bytes of data and 9 bytes of header. While listening, a multi-stage behavior similar to transmission was observed. Initially, power use rose to 13.8mW for $680\mu\text{s}$, and 37.5mW for an additional 4.04ms .

Restrictions were few but significant:

- Limited to 80 bits payload per message
- Wake-on-radio too costly to implement

3.3 Energy Storage

While the eZ430-RF2500-SEH kit did include two small Li-ion batteries (CBC050-MBC-ES) and a 1mF capacitor for burst currents, these storage mediums have neither the

capacity nor lifetime necessary for the lab in a brick. Integrating a system into the structure of a building requires that the system have a similar lifetime to the building, which can vary from 50 to 70+ years, with most buildings exceeding their original design lifetimes. It was this constraint that defined the remaining requirements for the energy storage system.

- 20 years effective life
- Minimum of 3 days of microcontroller energy storage with no energy input

The only commercially available option that fulfills the lifetime requirement is a capacitor. In order to hold three days of energy requires a supercapacitor. Given recent advances in this field, supercapacitors are available in many sizes from 1F to many hundred Farads that still fit within the form factor of the brick [56]. However, the only type of supercapacitor available is electrolytic double layer. This imposed the restraint of operating at no more than 2.75V. Any system requiring a greater voltage than this would need a DC-DC boost converter.

Given that the gas sensors are by far the largest load, it made sense to size the supercapacitor to power them first. Sensing events require a certain minimum of energy. Measuring the time required to achieve a stable output allowed for the calculation of this minimum energy. Applying more power to a sensor causes it to heat faster and stabilize sooner. Also, the power applied to the sensor's heating element must overcome the power lost to the environment, which is nearly linear with time. From Figure 40, 3V across a 30Ω heater is produced a stable measurement at 20s, using only 6J. 2V across the same heater required approximately 60s of heating, which corresponded to 8J. Using 2.35V from the

energy harvesting section and assuming a worst-case settling time of 60s established the minimum energy required for one sensing event at 11J.

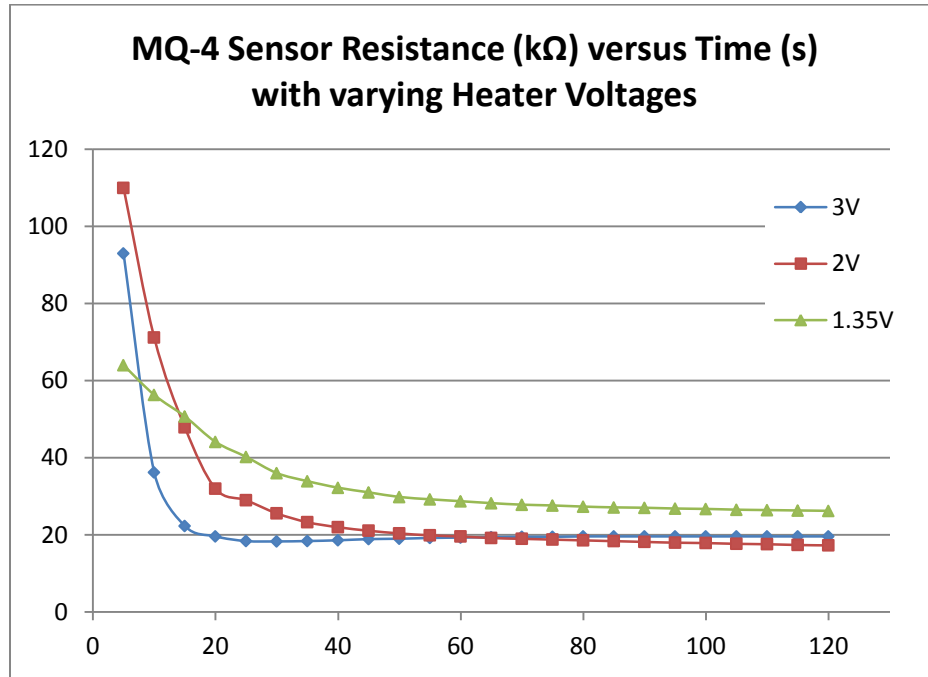


Figure 40 – Representative comparison of Sensor Resistance versus time with 3V, 2V, and 1.35V across the heating element for the MQ-4 (Carbon Monoxide) sensor.

Given the energy needed for the sensors, calculating the required supercapacitor size was straightforward. Assuming a continuous capacitance loss of 30% every 10 years [56] and a 20 year life, the final capacity will be slightly less than half the original value. Doubling the 11J necessary for a measurement means that the supercapacitor, when new, should have a capacity of at least 22J. At 2.35V, 8F is required.

With the minimum size of the supercapacitor set, it would seem reasonable to install the largest capacitor that could fit within the size constraints. However, the larger the capacitor, the larger the leakage current, which for an energy harvesting application is a significant problem. Therefore, the appropriate supercapacitor is the smallest one that will still allow operation at the end of the device's life: 10F.

With the supercapacitor size set, the last important issue to determine was the final voltage of the supercapacitor after a sensing event. When turned on, a gas sensor drew current through both the sensing element and the heater element in parallel. However, the sensing element resistance in series with the load resistance was never less than 3.5k Ω , more than 110 times the heater resistance, and could be ignored. The RC time constant for a 30 Ω heater and 10F supercap was 300s. Assuming a settling time of 60s and a starting voltage of 2.35V, the ending voltage across the capacitor would therefore be 82% of the starting value, or 1.92V.

The eZ430-RF2500-SEH included a Li-ion battery and a 1000 μ F capacitor. However, a Li-ion battery's lifetime is far below the 20 year system lifetime, and is therefore ignored as an energy storage device. The voltage drop on the 10F supercapacitor during a sensing event would be more than the eZ430 could reliably handle without browning-out, so a second 5F supercapacitor specifically for the microcontroller and radio.

The restrictions on the rest of the design from this section became:

- No more than 2.75V for any system without a DC-DC boost converter
- 2.2V input to the eZ430-RF2500-SEH in place of the PV panel
- Loads must take into account decreasing source voltage

3.4 Energy Harvesting

Given the eventual placement of the lab in a brick on the exterior of a building, it would have been trivial to stipulate that it must be placed with an unobstructed view of the sun during peak daylight hours, attached a solar panel, and moved on in the design.

However, the overall purpose of the lab is to evaluate air quality where people are. People go places that do not receive much incident solar energy. Therefore, the goals of this section were tailored to not only power the device, but also to investigate alternative energy harvesting schemes. Unfortunately (or fortunately) buildings do not move very much, so piezoelectric harvesting would not provide enough energy. Also, ambient RF harvesting would be extremely site specific and was discounted as well. The requirements for this section therefore became:

- Incorporate solar energy harvesting as a baseline system
- Incorporate thermal energy harvesting with through-wall heat transfer

The eZ430-RF2500-SEH included the CBC-SEH-01 energy harvesting board with the CBC5300 energy harvesting module and a 2.25”x2.25” amorphous silicon solar panel (CBC-PV-01). [41] While not the most efficient solar panel available, the CBC-PV-01 is representative of those currently available for a production device, and was therefore kept in the final design. The CBC-SEH-01 energy harvesting board was designed purely to operate the eZ430 microcontroller and radio board, and as such was not overly conducive to the relatively massive loads of resistive gas sensors. A solar energy harvesting chip from Linear

Technology, the LTC3105, was selected to serve as the primary interface between the PV panel and the rest of the device.

In order to validate that the PV panel and solar harvesting chip would work, a model had to be developed beginning with the available ambient energy. The first step in determining how much energy was available to the brick was modeling the solar energy striking the brick's surface. Radiant energy has been used to great effect to generate electricity through optical concentration and thermal conversion, and more recently through photovoltaic systems. Although the precise amount of solar energy striking a point the Earth's surface at any given time is dependent upon the distance from the Earth to the Sun, amount of atmosphere the light must traverse, moisture and dust content of that atmosphere, and orientation of the chosen point in relation to the incident rays, simplified equations have been developed allowing for the prediction of daily solar irradiance with an empirical one-sun-hour parameter [63]. Measured values for the insolation available throughout the year for many US cities have been compiled by the National Renewable Energy Laboratory in the Solar Radiation Data manual for Flat-Plate and Concentrating Collectors, commonly referred to as the Redbook [16]. Equation 1 shows how to determine the expected power available using these values.

Equation 1 – Per day energy output given insolation based on plate orientation, area of the plate, and average system efficiency. [63]

$$\text{Power (kWh/day)} = \text{Insolation} \left(\frac{\text{kWh/m}^2}{\text{day}} \right) * \text{Area (m}^2) * \text{Average System Efficiency } (\bar{\eta})$$

Table 8 lists the measured insolation from 1961 to 1990 for flat-plate collectors at various tilt angles for Raleigh. This table is reproduced below exactly from the Redbook.

Table 8 - Solar Radiation for Flat-Plate Collectors Facing South at a Fixed Tilt (kWh/m²/day), Uncertainty $\pm 9\%$. [16]

Tilt (°)		Jan	Feb	Mar	Apr	May	June	July	Aug	Sept	Oct	Nov	Dec	Year
0	Average	2.4	3.2	4.4	5.5	6.0	6.3	6.1	5.5	4.6	3.8	2.7	2.2	4.4
	Min	2.0	2.5	3.6	4.8	5.1	5.7	5.2	4.3	3.8	3.2	2.0	1.6	4.0
	Max	2.8	3.8	5.1	6.4	6.6	7.1	6.8	6.1	5.3	4.4	3.0	2.6	4.6
Latitude -15	Average	3.4	4.1	5.0	5.8	6.0	6.2	6.0	5.7	5.1	4.6	3.7	3.1	4.9
	Min	2.6	3.1	4.0	5.1	5.1	5.5	5.1	4.5	4.1	3.7	2.5	2.1	4.5
	Max	4.1	5.0	6.0	6.9	6.6	6.9	6.7	6.3	6.0	5.6	4.3	4.0	5.1
Latitude	Average	3.8	4.5	5.2	5.7	5.7	5.7	5.6	5.5	5.2	4.9	4.1	3.6	5.0
	Min	2.8	3.3	4.1	5.0	4.8	5.1	4.7	4.3	4.1	3.9	2.7	2.3	4.5
	Max	4.8	5.6	6.2	6.8	6.2	6.4	6.2	6.1	6.1	6.0	4.8	4.6	5.2
Latitude +15	Average	4.1	4.6	5.1	5.3	5.0	4.9	4.9	5.0	5.0	5.0	4.3	3.8	4.8
	Min	2.9	3.4	3.9	4.6	4.3	4.5	4.2	3.9	3.9	3.8	2.8	2.3	4.3
	Max	5.2	5.8	6.1	6.3	5.5	5.5	5.5	5.6	5.9	6.1	5.2	5.1	5.0
90	Average	3.6	3.8	3.6	3.1	2.5	2.3	2.4	2.8	3.3	3.8	3.7	3.5	3.2
	Min	2.5	2.8	2.8	2.7	2.3	2.2	2.1	2.2	2.5	2.9	2.3	2.0	2.9
	Max	4.7	4.8	4.3	3.6	2.7	2.4	2.6	3.0	3.8	4.8	4.5	4.7	3.4

Photovoltaics are generally listed with power outputs for standard test conditions (STC). From these values, the surface area of the panel, and Equation 2, an efficiency percentage can be calculated. Applying this process to the CBC-PV-01 provided an efficiency which was then applied to the information in Table 8 to provide an expected per-day energy output. Unfortunately, the CBC-PV-01 was intended for indoor use, and as such listed the expected output power as a function of Lux. To convert lux to Watts, a luminous efficacy of radiation 283lm/W was assumed. [64]

Equation 2 - Efficiency of the CBC-PV-01 assuming 200 lux of white fluorescent light and a luminous efficacy of 283 lumens per watt.

$$\eta = \frac{P_{out}}{P_{in}} = \frac{800mV * 201\mu A}{(200 \text{ lux FL} * 3.29 * 10^{-3} m^2) / (283 lm/W)} \cong \frac{161\mu W}{2.33mW} = 6.91\%$$

Table 9 – Monthly average, minimum, and maximum energy produced per day by the CBC-PV-01 in Raleigh, NC, when placed vertically and facing south in Wh/day and kJ/day.

		Jan	Feb	Mar	Apr	May	June	July	Aug	Sep	Oct	Nov	Dec	Year
Average	Wh/day	1.01	1.07	1.01	0.87	0.70	0.65	0.67	0.79	0.93	1.07	1.04	0.98	0.90
	kJ/day	3.64	3.84	3.64	3.13	2.53	2.32	2.42	2.83	3.33	3.84	3.74	3.54	3.23
Min	Wh/day	0.70	0.79	0.79	0.76	0.65	0.62	0.59	0.62	0.70	0.81	0.65	0.56	0.81
	kJ/day	2.53	2.83	2.83	2.73	2.32	2.22	2.12	2.22	2.53	2.93	2.32	2.02	2.93
Max	Wh/day	1.32	1.35	1.21	1.01	0.76	0.67	0.73	0.84	1.07	1.35	1.26	1.32	0.95
	kJ/day	4.75	4.85	4.34	3.64	2.73	2.42	2.63	3.03	3.84	4.85	4.55	4.75	3.43

Basic model validation was determined through benchtop testing of the PV panel. The panel was loaded with an RS-200 Resistance Substituter from IET Labs, Inc. A Samsung Nexus S provided a reference brightness value in lux. Two Agilent 34401A multimeters provided voltage and current measurements. Three varying brightness levels were tested: 4.7 lux, the minimum available; 187 lux, approximately that at which the PV panel was rated; and 315 lux, the maximum available. The output from these tests was graphed in Figure 42. Interestingly, peak efficiency for both the 187 lux and 315 lux tests were determined to be over 17%, which is greater than the most efficient amorphous PV cell currently in existence [38]. This disparity is most likely due to error in the measured lux

value, but could also be accounted for in a variance in the actual spectral efficiency of the fluorescent lights used and that used to calculate the assumed luminous efficacy.

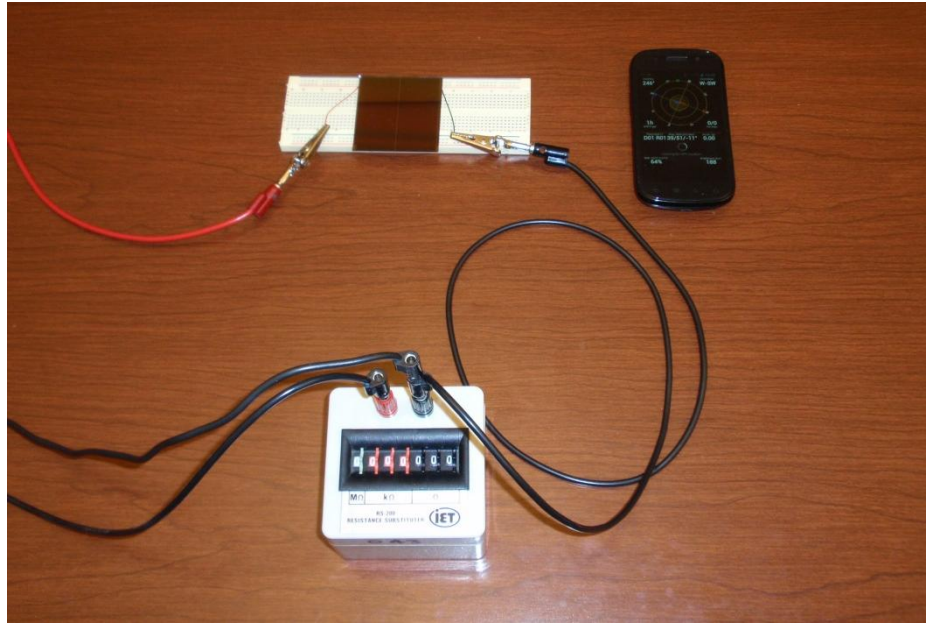


Figure 41 - Picture of the benchtop setup used to test the efficiency of the CBC-PV-01 solar panel. The panel is placed in series with a variable resistor box to allow for changing the load in order to track the non-linear current-voltage curve. A smartphone is used as a light meter to determine incident radiation.

Figure 42 demonstrates two very important aspects of PV panels. Firstly, the electrical efficiency of the panel is directly tied to the size of the load attached, and therefore the voltage across the terminals. A maximum power point tracker must be included in any PV energy harvester to maintain peak panel efficiency. Secondly, the efficiency of the panel is also tied to the insolation it is exposed to. Power output from a panel will be reduced in low light conditions not only because there is less energy available striking the panel's surface, but also because the panel is less capable of converting this light energy into

electrical energy. For model simplicity, the calculated efficiency, 6.91%, was used through the rest of the modeling.

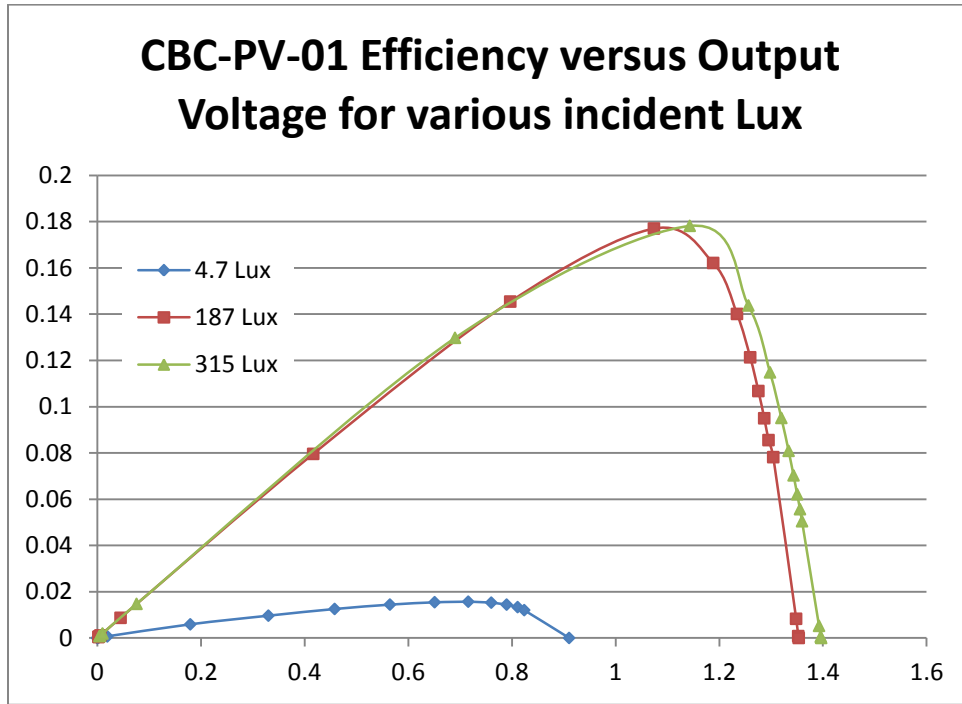


Figure 42 - Graph of panel efficiency versus output voltage for the CBC-PV-01 for three desktop lux values (4.7 lux, 187 lux, and 315 lux).

It was also somewhat useful to find the energy per hour available to the solar panel. Clear-sky insolation tables of kWh/m²/day have already been calculated in other work for latitudes on 5° increments. [63] The recording station used to generate the Redbook data used earlier was located at 35.87°N, so interpolation was performed on the 35° and 40° tables. In order to account for local weather issues, surface area of the CBC-PV-01, and efficiency, the hourly insolation values were converted to a percent of total daily insolation and then

multiplied by Table 9 on a month by month basis. Figure 43 and 44 show the expected hourly energy output for January through June and July through December, respectively.

To accomplish the second part of this system's goals, many thermo-electric generation schemes were evaluated. Every TEG currently available has a curved efficiency band with peak efficiency only over a narrow band of temperatures. TEG operation in and around normal ambient temperatures is avoided as a rule due to extremely poor energy conversion characteristics. Given these facts, the types of TEGs appropriate for this project are limited. Two systems were developed with two different types of TEGs.

In the more traditional approach, two 40mmx40mm BiTe thermo-electric generators (1261G-7L31-05CQ) from Custom Thermoelectric were thermally placed in parallel with one side facing the ambient air and the other tied through thermally conductive epoxy to a pyrolytic graphite sheet (PGS). This PGS would then be used as a thermal bridge to the interior of the wall that the brick is to be placed in, with the interior environment acting as the thermal sink, either hot or cold depending on the outside air temperature. Electrically, the TEGs were tied in series to the LTC3109 energy harvesting chip from Linear Technologies. The LTC3109 allows for full wave rectification which permits the TEGs to produce usable electrical energy under either a positive or negative thermal gradient between the interior and exterior air temperatures. Reasons for selecting the LTC3109 are described further in this section.

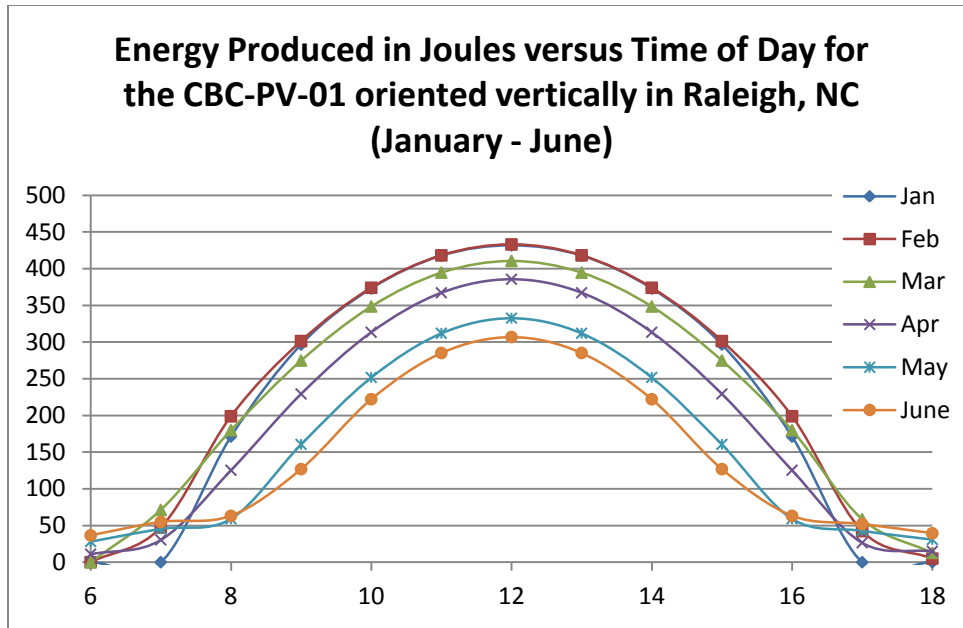


Figure 43 – Expected hourly energy output through a day from the CBC-PV-01 oriented vertically and facing south in Raleigh, NC, for January through June.

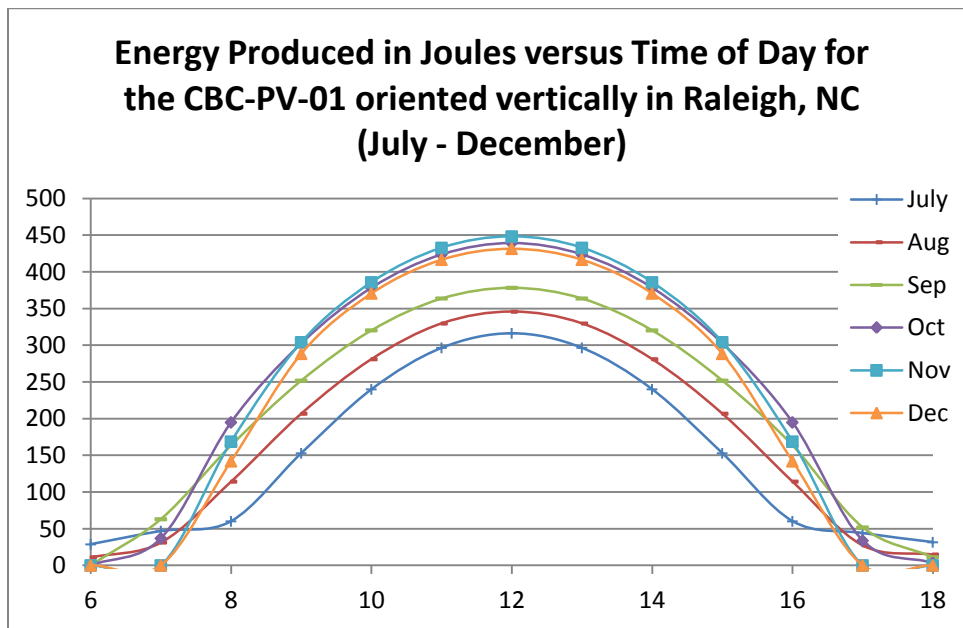


Figure 44 - Expected hourly energy output through a day from the CBC-PV-01 oriented vertically and facing south in Raleigh, NC, for July through December.

Along with the standard TEG, a new type of TEG has been developed that incorporates alternating layers of thin crystal lattices, thereby increasing the overall amount of energy that can be extracted from any given thermal gradient. However, these TEGs are extremely difficult to produce, and as such are expensive and exceedingly small. Two 2mmx2mm thin film TEGs (HV37) from Nextreme were incorporated into the project. Similar to the standard TEGs, thermal epoxy and PGS tied the back sides to the interior wall space, however, given their small size, compound parabolic collectors (CPCs) from Edmunds Optics were able to be placed on the exterior face while still remaining within the brick form factor. The CPCs increase the effective surface area of the TEGs by a factor of 10.77, but limited the angles at which sunlight could strike the TEGs to 25° from center. Electrically, they were tied in series to the LTC3108 which was a half wave version of the LTC3109 mentioned previously.

A model was developed for the TEGs similar to the PV evaluation. However, whereas photovoltaics are almost exclusively concerned with the irradiance they are exposed to with a minor temperature dependency, the energy output from thermoelectrics utilizing the sun and ambient air as power sources is significantly more complicated. Calculations for the expected energy output must take into account heat flux through the device, resistances to this flow, the resultant temperature across the TEG itself, and the efficiency of the TEG in transforming this temperature delta into usable energy.

Heat flux through the device is determined by the outside air temperature, incident solar radiation, efficiency of converting that radiation into thermal energy, losses through radiation and convection on the outside surface, the inside air temperature, and the series

thermal resistance or conductance of the components in the device. The incident radiation has already been demonstrated by the photovoltaic modeling and required only changes for the surface area of the two TEG systems, the inclusion of the CPCs, and the tilt of the CPCs and HV37 TEGs. The conversion of this radiation to thermal energy was approximated with an efficiency inverse to the reflectivity of the material the light is striking. Losses due to re-radiation were calculated based on the Stefan-Boltzman Law given a temperature. Energy gains and losses from and to the air through convection were a bit more complex and required accounting for the difference in temperature of the ambient air and the surface of the device and the wind-speed variant heat transfer coefficient. Historical models can be used for the outside air temperature. The inside air temperature was assumed to be held constant at 25°C. Combining each of these, an equation was developed to model heat flux through the entire system.

Equation 1 combines the insolation on a flat plane, the area of that plane, and the efficiency of conversion from sunlight to electrical power. The same equation can be used to find the solar power flowing into the exterior of the TEGs. Whereas the efficiency calculated for the PV panel was relatively low, the conversion from sunlight to heat is generally very high, and can be approximated using the average reflectivity of the surface. Equation 3 includes this change. Metal Velvet, an extremely low reflectivity foil from Acktar Advanced Coating Ltd., was applied to the TEGs to raise the conversion efficiency. Furthermore, using the clear-sky insolation tables used previously that divide out the per-day insolation into hour blocks allows for a much more accurate estimation. The insolation values for the CustomThermoelectric and HV37 were different due to the different angles each were set at

in relation to the latitude. Also, the clear-sky insolation tables were zeroed 1 hour 40 minutes before and after noon for the HV37 to account for the angles allowed with the CPC.

Equation 3 - Energy in kWh/day produced given Insolation, Surface Area, and Surface Reflectivity.

$$Q_{solar} \text{ (kWh/day)} = \text{Insolation} \left(\frac{\text{kWh/m}^2}{\text{day}} \right) * \text{Area (m}^2) * (1 - \% \text{ reflection)}$$

Energy will be re-radiated back into the atmosphere according to the Stephen-Boltzman Law. Equation 4 demonstrates how the instantaneous power loss was calculated.

Equation 4 - Power radiated to the environment from the exterior sides of the TEGs.

$$Q_{radiation} \text{ (W)} = \sigma \left(\frac{\text{W}}{\text{m}^2 * \text{T}^4} \right) * \text{Area (m}^2) * \text{Temperature (} T_{\text{surface}}^4 \text{)}$$

Conduction and convection with the ambient air will drive the surface temperature of the TEG to the exterior environment temperature. In Raleigh, this phenomenon will both provide more energy than insolation alone for the TEG during the summer days and winter nights, and work against solar heating during summer nights and winter days. While the Equation 5 is straightforward, one component, the heat transfer coefficient, is dependent on the speed of the air moving across the exterior face of the TEG. Conveniently, the Redbook includes both the ambient air temperature average, minimum, and maximum and the average

wind speed per month. Equation 6 shows an empirically derived equation for the heat transfer coefficient for a given wind speed. Humidity and air pressure affects are ignored.

Equation 5 - Power lost (or gained) to the environment due to a temperature differential between the surface of the device and ambient.

$$Q_{convection}(W) = h_c \left(\frac{W}{m^2T} \right) * Area (m^2) * (T_{surface} - T_{ambient})$$

Equation 6 - Approximation to calculate the heat transfer coefficient to air for a given wind speed.

$$h_c \text{ (heat transfer coefficient)} \cong 10.45 - v_{wind} + 10 * v_{wind}^{0.5}$$

A similar equation could have been developed to account for the energy transfer from the PGS to the interior of the building. However, this became unnecessary as it was assumed that a sufficiently large heat sink could be found such that no matter the heat flux through the device, the surface area of the heat sink would keep the end of the PGS at approximately 25°C.

The final necessary component to create the model was the thermal resistance from the outside to the inside. As each TEG created a separate series “circuit” of thermal resistances, the resistances of the elements from the outside to the inside for each circuit were simply added.

Table 10 - Listing of the Specific Thermal Resistances for each of the elements in series with the 40mmx40mm CustomThermoelectric TEGs. Component values were taken from datasheets where available and measured or approximated when necessary.

Material	Thermal Conductance (W/mK)	Area (m2)	Thickness (m)	Specific Thermal Resistance (K/W)
TEG				
CustomThermoelectric TEG	3.88	0.0016	0.0035	0.5638
Metal Velvet				
Carbon	1.7	0.0016	0.000005	0.0018
Aluminum	205	0.0016	0.000115	0.0004
Adhesive	0.2	0.0016	0.00006	0.1875
Misc				
Epoxy	7.5	0.0016	0.0001	0.0083
PGS	700	0.000004	0.15	53.57
Total				54.33

Table 11 - Listing of the Specific Thermal Resistances for each of the elements in series with the 2mmx2mm HV37 TEGs from Nextreme. Component values were taken from datasheets where available and measured or approximated when necessary.

Material	Thermal Conductance (W/mK)	Area (m2)	Thickness (m)	Specific Thermal Resistance (K/W)
TEG				
Nextreme HV37 TEG	6.37	4.22E-06	0.00056	21
Metal Velvet				
Carbon	1.7	4.22E-06	0.000005	0.70
Aluminum	205	4.22E-06	0.000115	0.13
Adhesive	0.2	4.22E-06	0.00006	71.09
Misc				
Epoxy	7.5	4.22E-06	0.0001	3.16
PGS	700	0.00000035	0.15	612.24
CPC	1.12	0.000271	0.02902	95.61
Total				803.94

With all the components, a full model was developed.

Equation 7 - Conservation of energy based equation for the calculation of energy available and lost through the thermoelectric conversion process.

$$Q_{solar} - Q_{radiation} - Q_{convection} - Q_{extracted} = Q_{sink}$$

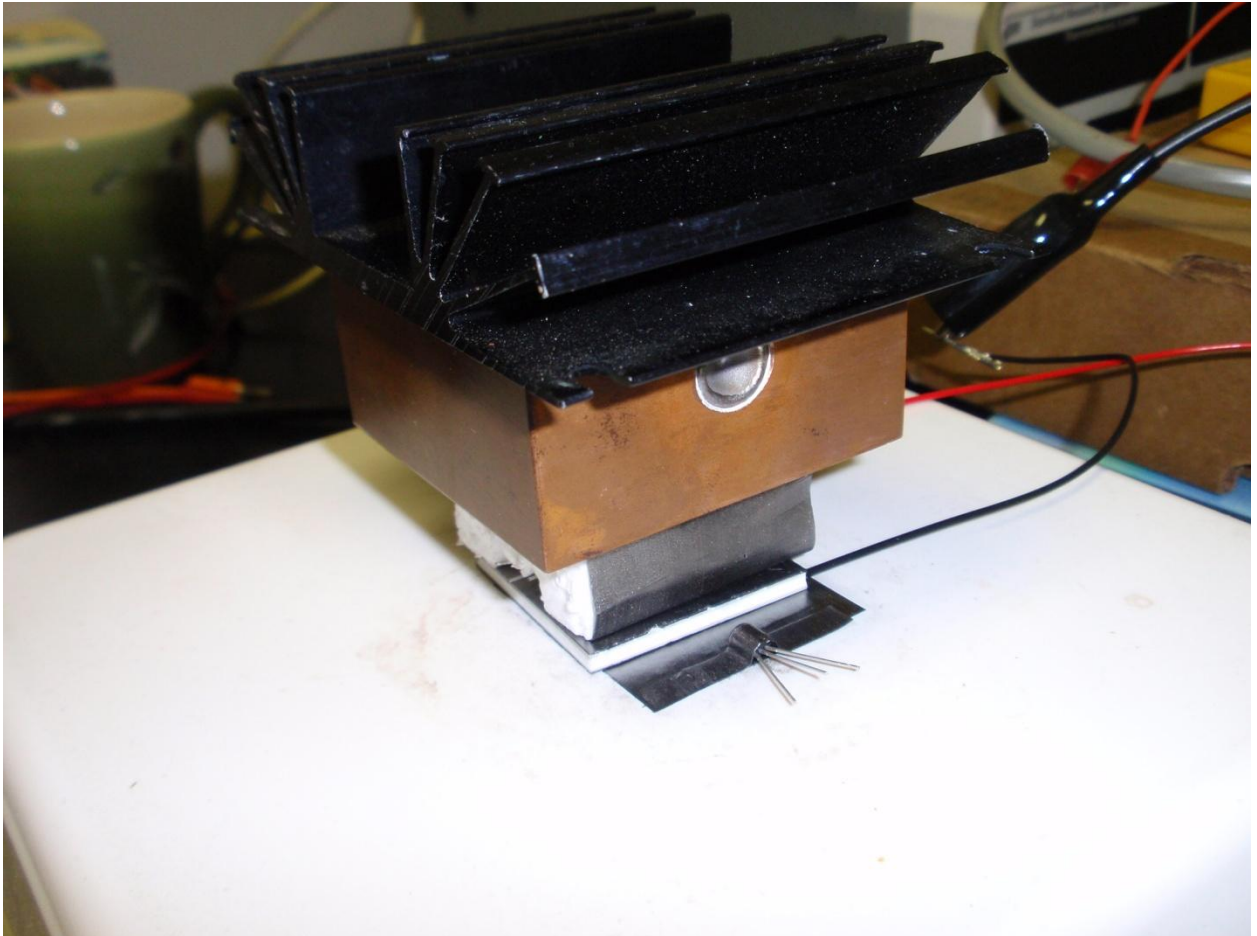


Figure 45 - Picture of the benchtop testing setup used to validate the TEG datasheet values. The TEGs were sandwiched between a large copper heatsink and a hotplate with thermistors attached via PGS to both sides of the TEGs for the most accurate temperature readings. Voltage across the TEGs and current through a series potentiometer measurements were taken to determine power output.

In order to validate the datasheets, benchtop testing was conducted on the TEGs. The generators were placed between a hotplate and a copper heatsink inside a 25°C lab. Experiments were run with between 5°C and 20°C across the plates. Pyrolytic graphite sheets were used as thermal connections from each side of the TEGs to thermistors used to verify the operating temperatures. Figure 46 through 49 show the voltage versus current and power curves for various temperature deltas for each type of TEG. After a few tests, it became extremely apparent that the most important aspect of extracting power from a TEG was ensuring a strong thermal connection from it to the heat source and sink. Measured efficiencies were below the datasheet values due to these excess thermal resistances.

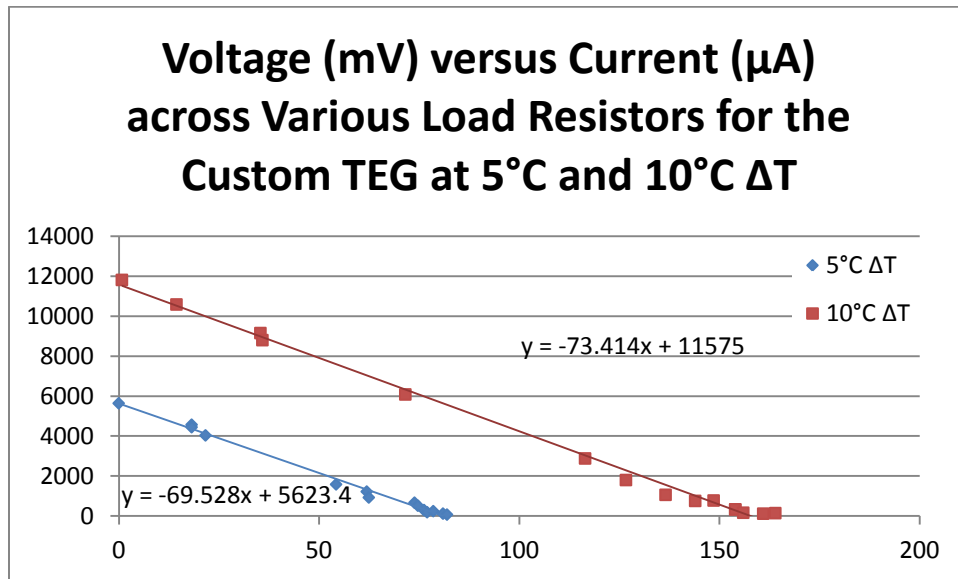


Figure 46 - Graph of measured voltage and current at various load resistances for the 40mmx40mm TEG at 5°C and 10°C ΔT.

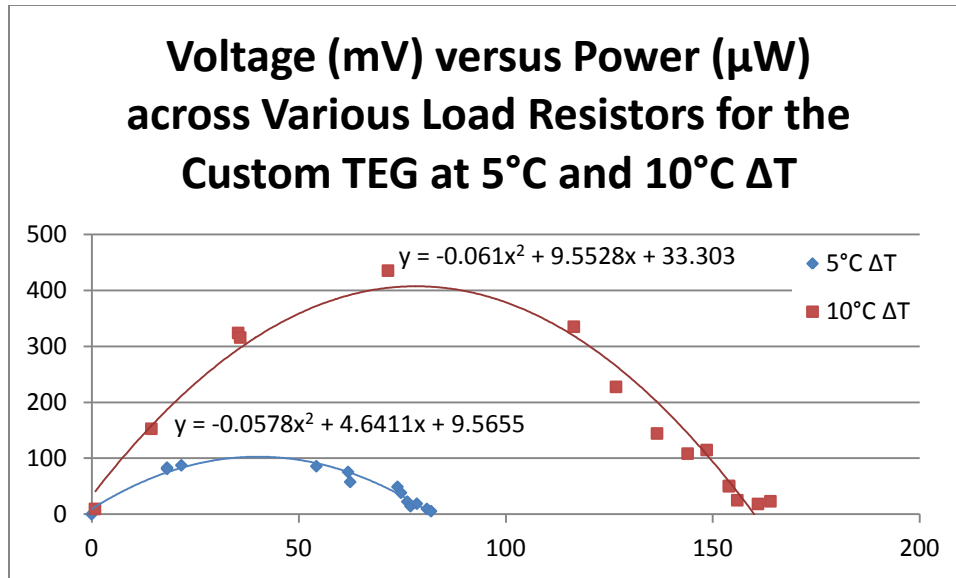


Figure 47 - Graph of measured voltage and calculated power at various load resistances for the 40mmx40mm TEG at 5°C and 10°C ΔT .

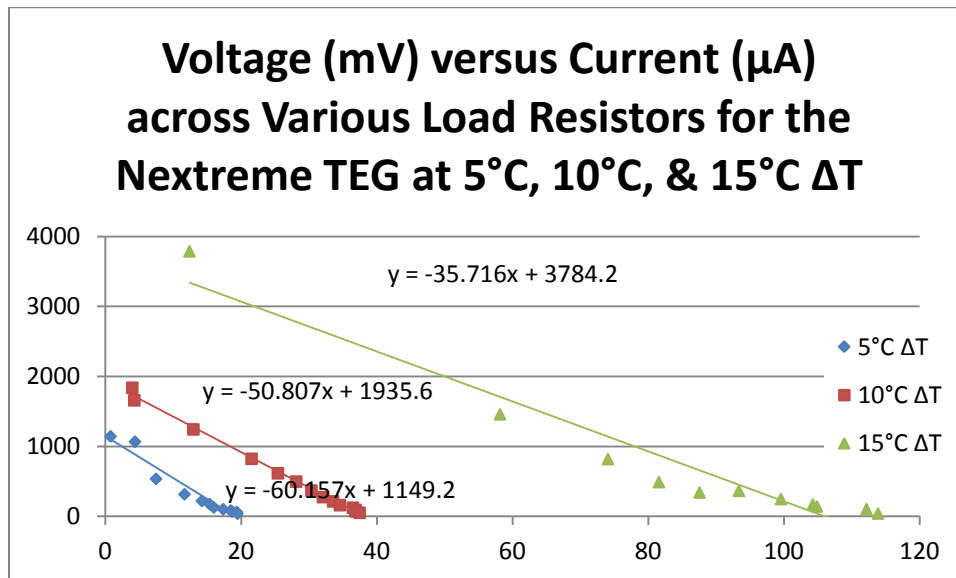


Figure 48 - Graph of measured voltage and current at various load resistances for the HV37 TEG at 5°C , 10°C , and 15°C ΔT .

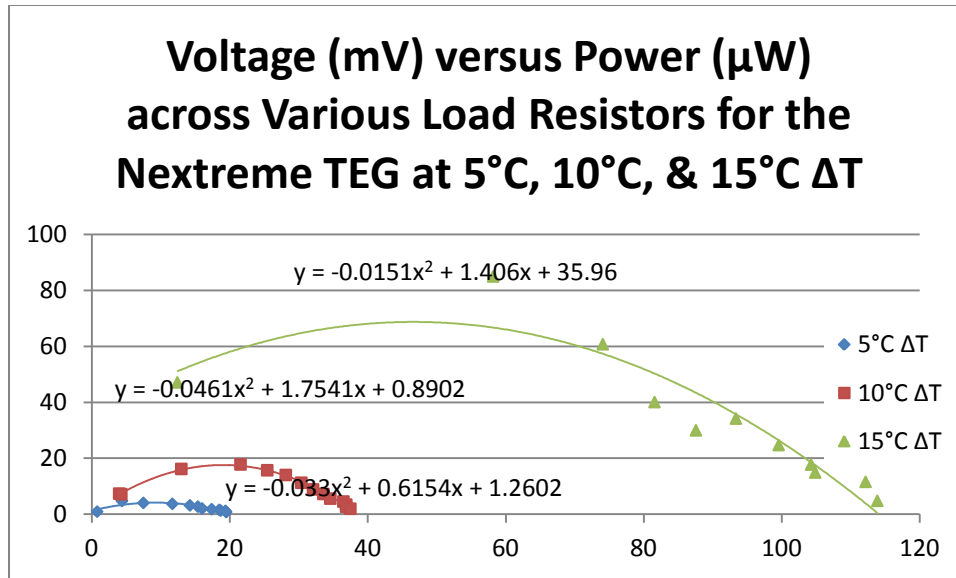


Figure 49 - Graph of measured voltage and calculated power at various load resistances for the HV37 TEG at 5°C, 10°C, and 15°C ΔT.

To determine the actual power output available and confirm or disprove the model, an experiment was conducted in which the PV panel from the eZ430-RF2500-SEH kit, both 40mmx40mm TEGs from CustomThermoelectric, and both HV37 2mmx2mm TEGs from Nextreme were fitted to a piece of 3/4" foam paneling. Two compound parabolic collectors were used to focus the sunlight onto the HV37 TEGs. One of each type of TEG included the Metal Velvet foil on the hot side. The highly thermally conductive epoxy was not used to adhere the PGS to the cold side of the TEGs. Instead, a thermal acrylic adhesive was included (specific thermal resistance of 0.22K/W for the Custom TEGs and 83K/W for the HV37s). A void behind this exterior panel simulated the interior of the lab-in-a-brick while an additional panel simulated a building wall. Behind the simulated wall, a Peltier cooler maintained a void between 8°C and 15°C to simulate the environment inside a building.

Temperature sensors were placed in the simulated building interior, inside the simulated brick, on the exterior face of the brick, behind and attached to the PV panel, and attached to both the hot and cold sides of each 40mmx40mm TEGs. A pyranometer measured the incident solar radiation. Each energy generator was tested in turn with two Agilent 34401A multimeters measuring the voltage and current across and through a RS-200 Resistance Substituter.



Figure 50 - Experimental setup to test the real-world power generation available from the CBC-PV-01 solar module, 40mmx40mm TEGs, and HV37 TEGs.

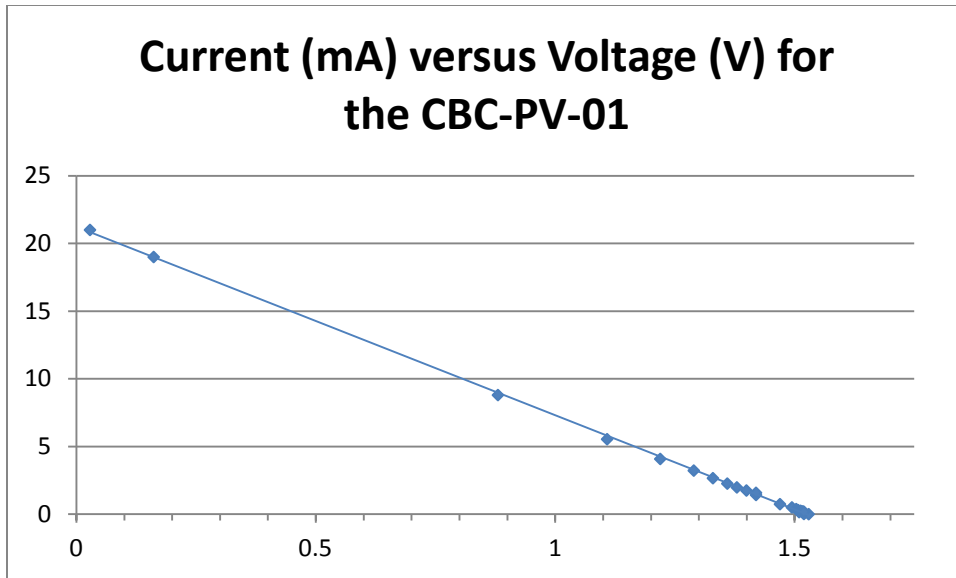


Figure 51 - Experimentally measured current versus voltage plot for the CBC-PV-01 in real-world, bright sun conditions.

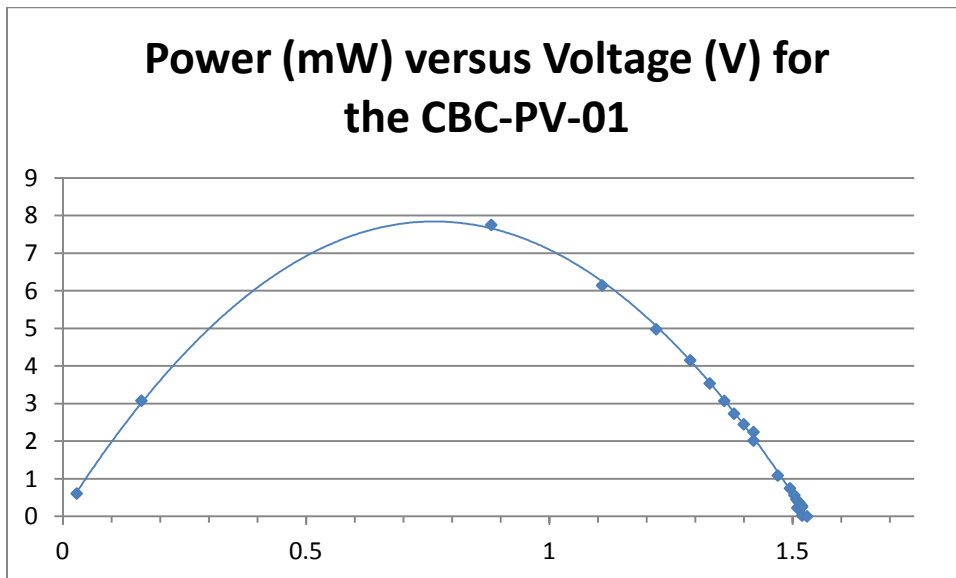


Figure 52 - Experimentally measured voltage and calculated power plot for the CBC-PV-01 in real-world, bright sun conditions.

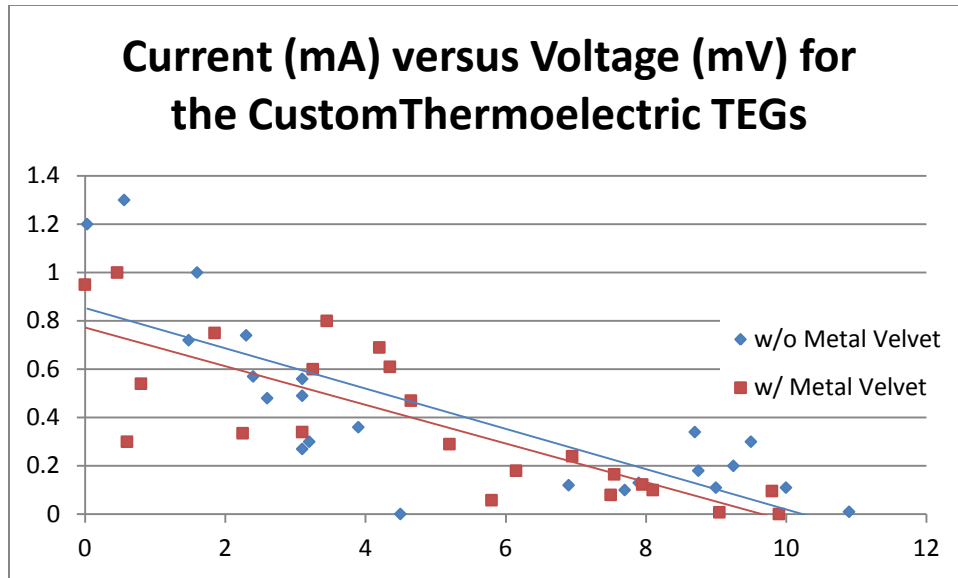


Figure 53 - Experimentally measured current versus voltage plot for the 40mmx40mm TEG in real-world, bright sun conditions both with and without the Metal Velvet anti-reflective coating.

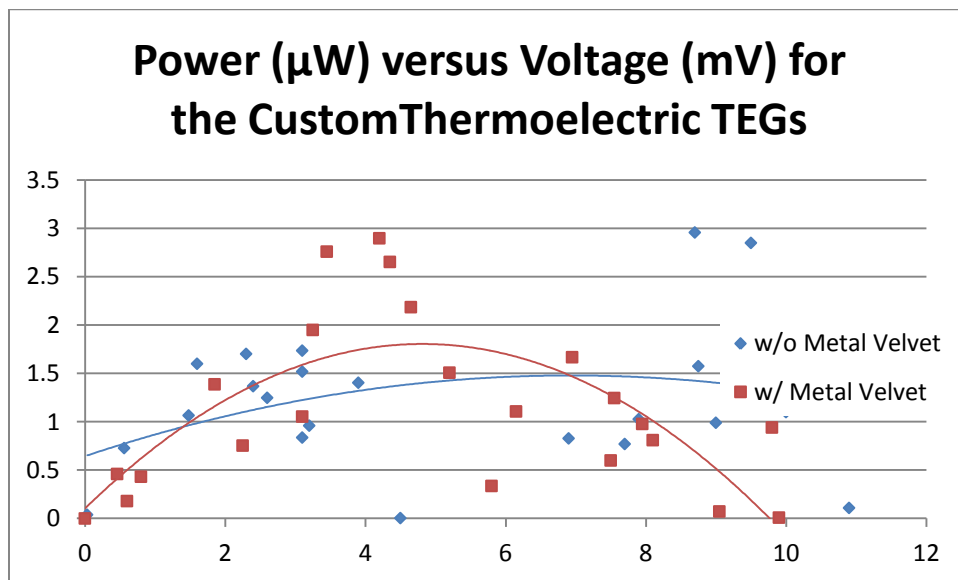


Figure 54 - Experimentally measured voltage and calculated power plot for the 40mmx40mm TEG in real-world, bright sun conditions both with and without the Metal Velvet anti-reflective coating.

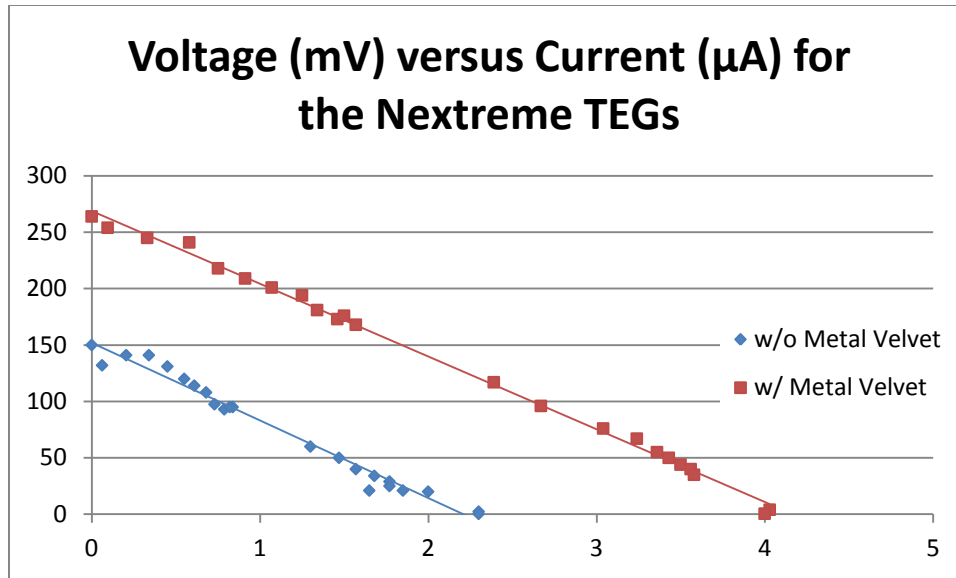


Figure 55 - Experimentally measured current versus voltage plot for the 2mmx2mm HV37 TEG with CPC in real-world, bright sun conditions both with and without the Metal Velvet anti-reflective coating.

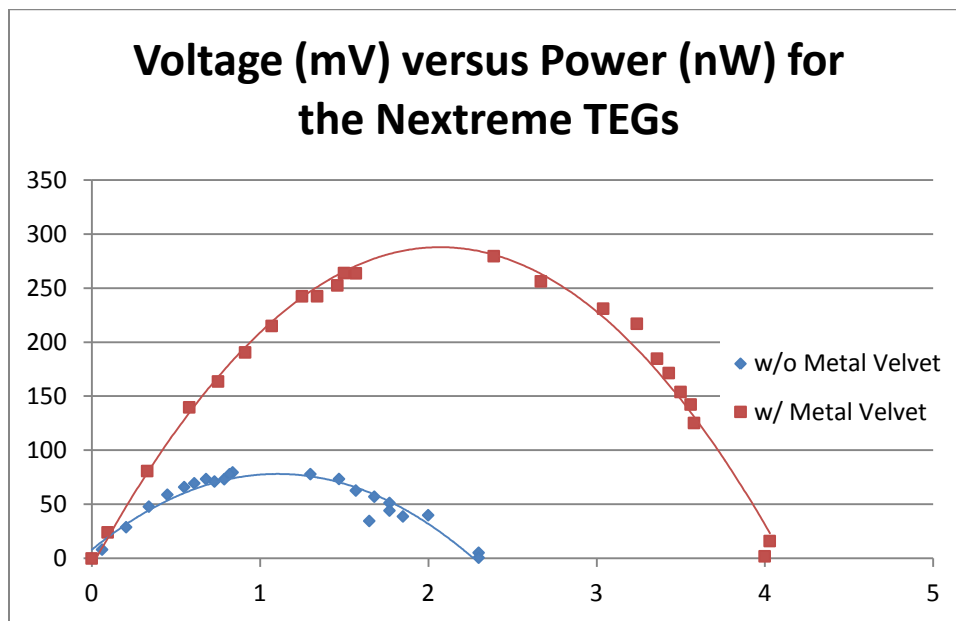


Figure 56 - Experimentally measured voltage and calculated power plot for the 2mmx2mm HV37 TEG with CPC in real-world, bright sun conditions both with and without the Metal Velvet anti-reflective coating.

The most obvious outcome from these results is that the solar panel produces three orders of magnitude more energy than the four TEGs combined. Surprisingly, the PV panel's IV curve was approximately linear, strikingly different than the benchtop curves. The CPC-PV-01 is designed to work under the relatively low light levels of standard fluorescent bulbs. Parasitic resistances in the cell become more prevalent in the direct sunlight and work to flatten the nonlinear IV curve noted in low light conditions. Given the PV panel's response during benchtop testing, a Maximum Power Point Tracker (MPPT) should still be included in its energy harvesting circuit.

As expected, the TEGs produced linear IV curves similar to those found in laboratory testing. The energy harvesting circuits for the TEGs can therefore do without the MPPT and run with a lower power loss which would otherwise have been used to power the MPPT controls. Of note, the Custom TEG without the Metal Velvet light-absorbing foil demonstrated very noisy IV and PV relationships. This was due to the reduction in conversion efficiency from solar radiation to heat, variations in wind speed altering the amount of heat energy gained and lost from convection and conduction, and can be assumed to be indicative of how the TEG will behave under low-light conditions. The Metal Velvet film on the other Custom TEG essentially served as a more consistent energy source than the ambient air, buffering the changes that the varying wind speeds caused. The more expected curves from the two Nextreme TEGs clearly illustrate the radiant energy to heat conversion when it is insulated from the ambient air.

Collectively, the three Linear energy harvesting circuits had primary outputs which could be set to a variety of values and LDO outputs locked to 2.2V. The CBC-SEH-01 was

retained to provide a regulated output to the eZ430 and fed through the LDO outputs from the three Linear harvesters. The LDO outputs are each charged to 2.2V before the regular outputs are ramped up. This ensures that the microcontroller will preferentially be powered even if there is a fault on the supercapacitor powering the sensors.

Verification of the energy harvesting circuits was performed by applying DC voltage from a standard power supply, the Agilent E3620A, and slowly stepping the voltage up from zero. A device was determined to have a turn-on voltage when the output pin began to ramp up to 2.35V and held. The LTC3105 was found to operate with an input from 0.2 to 5 V and includes Maximum Power Point Tracking, ideal for the PV cell. The LTC3108, when coupled with a 1:100 transformer on the input, operated from 20 to 500mV, which corresponded to the HV37 TEGs. The LTC3109 was similar to the 3108 but due to the full wave rectification had a higher minimum input voltage of 30mV, which corresponds to the larger 40mmx40mm TEGs.

Reverse blocking current was also tested, with both the LTC3108 and LTC3109 demonstrating less than 6 μ A with 2.35V on the output pins. However, the LTC3105 showed 22 μ A. Prior to incorporating the entire design into one system, an N-channel power MOSFET was included on the ground line with the gate tied to the PGOOD output from the LTC3105 and the source and drain inverted such that the body diode would allow charging until the PGOOD output turned the transistor on, but in all other states, the transistor would be off. Leakage current was thus limited to 4.6 μ A. A similar arrangement was tested on both the LTC3108 and LTC3109, but no reduction in leakage current was observed.

3.5 Sensors

The gas and particulate sensor requirements were designed to maximize their utility for sensing those elements most harmful to people [28]. Within that constraint, flexibility was given to the manner in which the measurement would take place as well as the power requirements for that measurement.

- Include the maximum number of sensors practicable
- At a minimum, include sensors for
 - Carbon Monoxide
 - Nitrogen Dioxide
 - Ozone
 - Volatile Organic Compounds
 - Particulate matter of PM₁₀ size or smaller

The MQ-4 (natural gas and propane), MQ-7 (hydrogen and carbon monoxide), and MQ-135 (nitrous oxides, smoke, and ammonia) from Futurlec were chosen as well as the MICS-2610 (ozone), MICS-2710 (nitrogen dioxide), and MICS-5521 (carbon monoxide and volatile organic compounds) from e2v (formerly SGX Sensortech). All of these sensors were based on measuring the change in resistance of a heated element in the presence of its target gas. However, this type of sensor was extremely prone to cross-sensitivity. The inclusion of additional sensors sensitive to chemicals not included in the listed requirements was to allow for primary component analysis to filter out this noise from the measurements.

Unfortunately, the each of the sensors had different specific voltage requirements. The Futurlec sensors required either 5V or 6V applied to the heater circuit for 24 to 48 hours continuously. The e2v sensors required between 1.7V and 2.5V but did not have a listed minimum heating time. Additional testing was performed to ensure that the Futurlec sensors could be operated outside their operating range to avoid an untenable restraint.

Additionally, heating the sensing element not only increases its reaction with the target gas, it also assists in driving out adsorbed humidity from the sensing compounds. Therefore, the ambient humidity became the most important measurement for calibrating each of the other sensor readings. The HIH-5030 from Honeywell was chosen to provide the humidity value.

For the particle counter, very few simple solutions existed. Most particle counters available require precise vacuums to ensure their measurements are accurate. For the lab in a brick, absolute precision is not required, or even possible given current limitations. Instead, given the success of similar research noted in the literature review a relatively simple IR reflective counter, the GP2Y1010AU0F from Sharp, was chosen.

Firstly, the Futurlec sensor had to be tested to determine if they could be operated with a meaningful sensing result at 2.35V, the voltage from the energy harvester outputs, rather than their listed 5V or 6V. If not, a boost converter would need to be incorporated into the design which would not only increase the complexity and take up valuable space, but also dissipate energy that could be better used elsewhere. Additionally, regardless of the voltage applied, requiring 24 hours of heating prior to taking a measurement is impossible given the energy source and storage mechanism. To provide the energy directly would require a

massive increase in the number of energy harvesters, and to be able to store a day's worth of energy would require a supercapacitor too large to fit within the form factor.

Testing was accomplished by applying voltages to the heating elements of the sensors and measuring the resistance of the sensing elements. Sensing resistance was intended to follow an inverse exponential curve approaching a limit defined by the percent of the target gas in the ambient air. Mathematically, it is possible to determine the eventual value of the curve from a few early data points at the sacrifice of accuracy. This premise was confirmed experimentally with the datasheet-recommended heater voltage values on the Futurlec sensors.

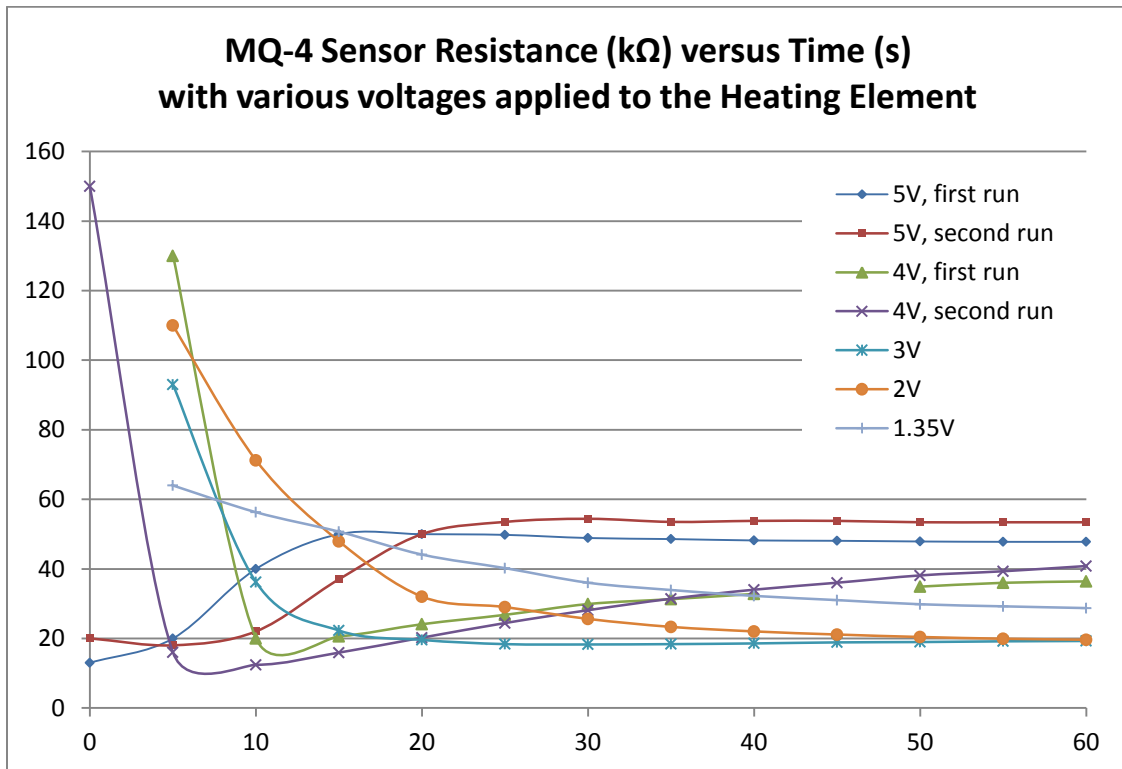


Figure 57 - Measured response from the MQ-4 sensor with varying heater voltages.

Reducing the heater voltage reduced the heater temperature, which in turn reduced the sensing element's sensitivity and accuracy. Experimentally, it was shown that with a significantly reduced heater voltage, a signal was produced that stabilized, but did not match the shape of the signal produced with the proper voltage (Figure 57). Calibration with known gas mixtures was not performed.

The circuit chosen to drive the sensors consisted of the sensing element being placed in series with a known load resistor in a voltage divider relationship. The heater element was placed in parallel with these two. The high sides of both branches were tied to the 2.35V line while the grounds were tied together and to the drain of an NMOS power transistor. The gate signal was provided by one of the eZ430 IO pins, and the source was tied to the system ground. The series load resistor was sized to maximize the voltage swing across the sensor considering the datasheet range of sensor resistances, without exceeding 1.5V, the chosen reference value.

Table 12 - List of sensors, minimum and maximum sensing resistances, and load resistors chosen to maximize the voltage swing as gas concentration changes.

Sensor	Sensing Resistance		Load Resistor Actual Value
	Minimum	Maximum	
MQ-4	2k Ω	20k Ω	5.617k Ω
MQ-7	2k Ω	20k Ω	5.617k Ω
MQ-135	30k Ω	200k Ω	54.39k Ω
MICS-2610	3k Ω	60k Ω	18.04k Ω
MICS-2710	800 Ω	8k Ω	2.673k Ω
MICS-5521	100k Ω	1M Ω	425.8k Ω

Equation 8 - Equation used to determine appropriate series resistance to include with the gas sensors to maximize the voltage swing as gas concentration changes, and taking into account the reduction in supply voltage due to powering the heating element.

$$R_{sensor} = \frac{V_{sensor} * R_{load}}{(V_{supply} \text{ (final measured value)} - V_{sensor})}$$

Given the relatively large power requirements for each of the Futurelec sensors, only one was allowed to operate at a time. The system needed to be allowed to recharge between measurements, possibly for hours. The e2v sensors, being significantly smaller and less energy intensive, were able to be operated in sequence: MICS-5521, MICS-2610, and then MICS-2710. Each of these sensors was rated for a different heater voltage: 2.4V, 2.35V, and 1.7V, respectively, and operating them in series allowed the supercapacitor voltage to drop to an appropriate value. All of the sensors were heated for one minute each to allow the measurement to settle.

As noted previously, humidity significantly affected the resistance value. A low voltage humidity sensor from Honeywell, the HIH-5030, was included. This extremely intuitive device allowed for the simplest measurement in the entire device. The voltage output varies with the sensed relative humidity as per the below equation. True relative humidity requires an adjustment for temperature. Conveniently, the eZ430 includes an integrated thermometer. With a current draw less than 200 μ A, the sensor is powered directly from one of the eZ430 digital IO pins. The output is tied to an ADC input pin and compared to a 2.5V reference. A humidity measurement is taken prior to each gas sensing event. A

measurement greater than 95% would halt the operation of any of the gas sensors to prevent damage.

Equation 9 - Method for determining relative humidity as per the HIH-5030 datasheet.

$$RH (\%) = \frac{\left(\frac{V_{out}}{V_{supply}} - 0.1515 \right)}{(0.006707 - 0.00001374 * T (^{\circ}C))}$$

Also included in the design was a particle counter from Sharp, the GP2Y1010AU0F. Internally, it was made from an IR LED source and detector. The two elements were out of direct line of sight. Any particle that entered the aperture in the middle of the device would reflect some portion of the IR signal towards the receiver, which would produce an analog voltage output proportional to the strength of the reflected signal. There was no method to differentiate between small numbers of large particles or large numbers of small particles. The six connections to the sensor were divided into two sets of three: one set for the LED, and one set for the sensor. The LED connections were tied to the 2.35V line and an NMOS transistor such that a high signal from the eZ430 would turn the LED on. The LED was set to draw approximately 10mA, which allowed for a small voltage buffer should the input 2.35V drop. The detector drew low enough current (2.4mA maximum) that it could be powered directly from the eZ430. The control circuitry had an undocumented startup delay of 60ms. Also, the maximum value of the output signal occurred 240 μ s after the application

of the LED signal. In order to accurately drive particle counter, the control circuitry needed to remain on while the LED was pulsed.

Finally, the particle counter required some type of air flow to bring dust through the aperture. An air inlet was cut into the front of the brick below the particle counter and an exit above such that the gas sensors, placed on the lower level, would create a small updraft due to the creation of an upside-down thermal gradient across the particle counter.

3.6 Experimental Procedure and Assembly

Combining all of the component systems into one working whole presented its own array of issues. The basic concept was to tie the harvesters together in parallel, attach the sensors to the 2.35V output, and attach the eZ430-RF2500-SEH to the 2.2V LDO output. As noted earlier, an inverted N-channel power MOSFET was attached to the LTC3105 with the energy harvester's internal ground tied to the MOSFET drain, and the system ground tied to the source. This significantly reduced the reverse leakage current into the LTC3105 without greatly affecting the system efficiency. N-channel power MOSFETs were used extensively throughout this system as switches. The gate-source threshold voltage was 1.0 and 2.0V and on-resistance less than 300m Ω for these V_{GS} , values allowing for efficient switching.

Combining the three harvesters in this way allowed for any of them to charge the 5F and 10F capacitors simultaneously. However, this parallel arrangement also meant that there would always be some small amount of leakage current flowing back into the harvesters from the capacitors.

The CPC-PV-01 was removed from the eZ430-RF-SEH. Instead of using the solar panel, the combined LDO outputs from the three Linear harvesters were used to feed into the CBC-SEH-01. Its internal boost converter maintained a regulated 3V input to the eZ430.

The eZ430 included 15 general purpose IO pins. Of those 15, ten could be used as inputs to the ADC. However, with six gas sensors requiring two pins each, one humidity sensor requiring two pins, one particle counter requiring three pins, and two voltage rails requiring one pin each, the eZ430 could not support the needed 19 pins. In order to reduce the number of pins required, the outputs from the gas sensors were tied together similarly to a multiplexer using more of the N-channel power MOSFETs. This reduced the number of eZ430 pins to 14: five in, nine out.

The last step was to implement a decision matrix that would minimize the data that needed to be stored while keeping enough to make the measurements accurate. As the system started up, the LDO line and 5F supercapacitor were the first to be charged. The CBC-SEH-01 fed off of the LDO line and was the second component to start up. Once the CBC-SEH-01 could maintain a regulated output, it turned the eZ430 on, which began the sensing process. Each gas sensing event required a humidity measurement. Each humidity measurement required a temperature measurement. As the particle counter was reliant upon the thermal gradient created when any of the gas sensors was activated, the best draft and therefore best particle counting measurement should be available immediately after the most energetic gas sensing event. Each Futurelec sensor utilizes about 18.4J at 306mW. It was decided that the particle counter would take a measurement after the Futurelec sensor located nearest the aperture: the MQ-135.

3.7 Coding

Programming the microcontroller turned out to be a relatively simple and straightforward affair. Initially, the eZ430-RF2500-SEH was programmed to sense the ambient temperature through a built-in on-chip thermometer. Both the end device and the access point sensed the temperature, but the end device transmitted its reading to the access point, and demonstration software provided a GUI that displayed both readings. By altering the included code through Code Composer Studio, five of the available pins were set as inputs to the ADC. Three utilized the internal 2.5V reference (measuring the two voltage lines and humidity), while the other 2 used the 1.5V reference (measuring all of the gas sensors and the particle counter). In order to save storage space and transmission bandwidth, the 10 bit ADC result was reduced to 8 bits. Resolution was maintained where possible by level shifting and scaling the analog outputs to remove the out-of-range high and low parts of the measurement.

Chapter 4 – Conclusions

The goal of this project was to create a gas sensing lab in a brick. It should create its own energy and store it for future use. It should be able to accurately sense many atmospheric gasses and particulates important to human health. It should be able to make multiple rounds of measurements per day and store them. Finally, it should be able to wirelessly transmit the data to a base station or access point.

The system fulfilled the requirements on a basic level. In creating its own energy, the system works. The PV panel provides milli-Watts of power while the TEGs each provide micro-Watts. Until the efficiency of thermoelectric generators significantly rises, photovoltaics will remain the primary power sources for systems of this size. That said, if the largest loads, the resistive gas sensors, were removed, the TEGs would be able to power the rest of the brick. Commercially available energy harvesting circuits were able to extract meaningful amounts of energy from each of the energy sources, though the thermoelectric sources could only barely produce enough voltage to overcome the minimum input requirement. Supercapacitors were effectively used to store this energy.

The gas sensors provided measurements, however accuracy was a significant concern. For the Futurlec sensors, operation in the brick was significantly outside the intended procedure, so the correctness of the measurements are not guaranteed. The e2v sensors were

rated for similar voltage levels to those used in the brick, and can be assumed to be more accurate, though the absolute accuracy cannot be assured without knowing the temperature of the sensing element. The humidity and temperature measurements have no significant accuracy issues. Finally, the particle counter, while accurate in counting particles, cannot be assured to have any sort of accuracy in determining particle density or type. Without a calibrated air flow rate, it is unknown how quickly a particle moves through the aperture. Also, without filter elements, which logistically cannot be included in a lab in a brick system, there is no way to determine the size of the particles reaching the sensor.

Finally, the microcontroller and radio setup used fulfilled the system requirements. Without a wake-on-radio feature, the system had to periodically ping for an access point and await a response, which could mean that the person recording data would need to wait for however long the duration is between pings. A shorter duration would mean a shorter wait, but more energy lost as each transmission uses an appreciable amount of energy. A wake-on-radio feature would eliminate both the wait and energy lost from pings without an access point nearby, but the current normal method for implementing such a feature involves leaving the radio on continuously, which would waste even more energy. Other than this minor communications issue, the eZ430 board fully implemented the lab in a brick concept.

Known faults in the design were limited to those areas that were not tested. Deploying the device in a real-world setting is likely to present problems heretofore unnoticed such as insect, water, or dirt intrusion into the sensing area; the effect of sub-freezing temperatures on the highly temperature dependent gas sensors; daily expansion and

contraction while encased in a rigid structure (the brick wall); and the public's response to yet another sensor deployed around them.

Chapter 5 – Future Research

There are many opportunities for future work in the fields utilized in the lab in a brick. The most obvious work is that which is ongoing: improving the efficiencies of solar panels, thermoelectric generators, and energy storage mediums; finding novel gas sensing processes; and improving the effectiveness of DC-DC transformers and energy harvesters.

Less obvious are those areas that are not normally an issue for anything other than these types of small, self-contained devices designed to interact with an unpredictable world. The faults noted earlier are a good place to start.

Most gas and particle testing is performed in relatively stable environments with ready access to grid power, such as carbon monoxide sensors in homes, particle counters in building controls, or oxygen sensors in industrial enclosed spaces. Exterior environmental monitoring is accomplished through large complex systems requiring space, maintenance and maintenance personnel, replacement filters, backup generators, and a myriad of other consumables. Weather independent, or at least weather resilient, gas sensing schemes are few, with the most promising being those relying on the absorption of light frequencies corresponding to the gasses in question. These are still relatively large, expensive, and have only been commercially developed for a few of the most commercially interesting gasses.

Improving the particle counter may be of the most benefit, however, due to the abysmal selection of units available and lack of apparent ongoing improvements. Taking the current design; that of an IR source, aperture for particles to pass through, and IR sensor; and simply replacing the IR sensor with a cell-phone style CCD could provide massive improvements very quickly. A short series of pictures taken in rapid succession of a known volume of space would improve the accuracy of particle counts, allow for the categorization of particles by size, and remove the need for a regulated air flow as the flow could be computed from the movement of particles. Including LEDs of various wavelengths could open up the possibility of determining particle composition as well.

REFERENCES

- [1] J. Sacks, L. Stanek, T. Luben, D. Johns, B. Buckley, J. Brown and M. Ross, "Particulate Matter-Induced Health Effects: Who Is Susceptible," *Environ Health Perspect.*, vol. 119, pp. 446-454, 20 Oct 2010, 2010.
- [2] Anonymous "2005 national-scale air toxics assessment," U.S. Environmental Protection Agency, Tech. Rep. 4, 11 Mar 2011. 2011.
- [3] C. Chen, K. D. Campbell, I. Negi, R. A. Iglesias, P. Owens, N. Tao, F. Tsow and E. S. Forzani. A new sensor for the assessment of personal exposure to volatile organic compounds. *Atmos. Environ.* 54pp. 679-687. 2012. . DOI: 10.1016/j.atmosenv.2012.01.048.
- [4] Anonymous "AQM 60 air quality station," Aeroqual Limited, Dec 2010. 2010.
- [5] (). *Air Quality Egg*. Available: <http://airqualityegg.com/>.
- [6] D. D. Redmond and S. C. Holman, "2010 annual monitoring network plan for the north carolina division of air quality," North Carolina Division of Air Quality, 1 Jul 2010. 2010.
- [7] A. Cronin, "PV system performance comparisons," University of Arizona, 2 Feb 2010. 2010.
- [8] W. G. J. H. M. van Sark. Feasibility of photovoltaic - thermoelectric hybrid modules. *Appl. Energy* 88(8), pp. 2785-2790. 2011. . DOI: 10.1016/j.apenergy.2011.02.008.
- [9] Anonymous "Specifications for and Classification of Brick," *Tech Notes on Brick Const*, vol. 9A, pp. 1-13, Oct 2007, 2007.
- [10] M. Dondi, F. Mazzanti, P. Principi, M. Raimondo and G. Zanarini, "Thermal Conductivity of Clay Bricks," *J. Mater. Civ. Eng.*, vol. 16, pp. 8-14, 2004.
- [11] W. T. Grondzik and D. L. O'Neal, "Heat, air, and moisture control in building assemblies - material properties," in *2009 ASHRAE Handbook - Fundamentals (I-P Edition)*, Inch-Pound ed., M. S. Owen and H. E. Kennedy, Eds. Atlanta, GA: American Society of Heating, Refrigerating and Air-Conditioning Engineers, Inc., 2009, pp. 26.7.
- [12] (12 Aug 2002). *Bricks - Thermal Conductivity and Thermal Resistance of Extruded and Pressed House Bricks*. Available: <http://www.azom.com/article.aspx?ArticleID=1567>.

- [13] O. Koronthalyova and P. Matiasovsky, "Pore structure and thermal conductivity of burnt clay bricks," in *Thermophysics 2007, a Meeting of the Thermophysical Society Working Group of the Slovak Physical Society*, Bratislava, Slovakia, 2007, .
- [14] P. Lertwattanaruk and J. Choksiriwanna, "The Physical and Thermal Properties of Adobe Brick Containing Bagasse for Earth Construction," *BUILT*, vol. 1, pp. 53-61, 2011.
- [15] C. Luo, B. Moghtaderi, S. Hands and A. Page. Determining the thermal capacitance, conductivity and the convective heat transfer coefficient of a brick wall by annually monitored temperatures and total heat fluxes. *Energy Build.* 43(2-3), 2011. . DOI: 10.1016/j.enbuild.2010.09.030.
- [16] W. Marion and S. Wilcox, *Solar Radiation Data Manual for Flat-Plate and Concentrating Collectors*. Golden, Colorado: National Renewable Energy Laboratory, 1994.
- [17] P. T. Tsilingiris. Thermal flywheel effects on the time varying conduction heat transfer through structural walls. *Energy Build.* 35(10), 2003. . DOI: 10.1016/S0378-7788(03)00053-7.
- [18] A. Page, B. Moghtaderi, D. Alterman and S. Hands, "A study of the thermal performance of australian housing," Priority Research Centre for Energy, University of Newcastle, Newcastle, 2011.
- [19] J. C. Chen. Thermodynamic analysis of a solar-driven thermoelectric generator. *J. Appl. Phys.* 79(5), 1996. . DOI: 10.1063/1.361143.
- [20] M. Telkes. Solar thermoelectric generators. *J. Appl. Phys.* 25(6), 1954. . DOI: 10.1063/1.1721728.
- [21] D. Kraemer, K. McEnaney, M. Chiesa and G. Chen. Modeling and optimization of solar thermoelectric generators for terrestrial applications. *Solar Energy* 86(5), 2012. . DOI: 10.1016/j.solener.2012.01.025.
- [22] M. Mizoshiri, M. Mikami, K. Ozaki and K. Kobayashi. Thin-film thermoelectric modules for power generation using focused solar light. *J Electron Mater* 41(6), 2012. . DOI: 10.1007/s11664-012-2047-0.
- [23] G. Chen. Theoretical efficiency of solar thermoelectric energy generators. *J. Appl. Phys.* 109(10), pp. 104908. 2011. . DOI: 10.1063/1.3583182.
- [24] D. Kraemer, B. Poudel, H. Feng, J. C. Caylor, B. Yu, X. Yan, Y. Ma, X. Wang, D. Wang, A. Muto, K. McEnaney, M. Chiesa, Z. Ren and G. Chen. High-performance flat-panel

solar thermoelectric generators with high thermal concentration. *Nature Materials* 10(7), 2011. . DOI: 10.1038/NMAT3013.

[25] J. Kim, S. K. Jung and J. T. Kim. Wireless monitoring of indoor air quality by a sensor network. *Indoor Built Environ.* 19(1), pp. 145-150. 2010. . DOI: 10.1177/1420326X09358034.

[26] Y. Gil, W. Wu and J. Lee. A synchronous multi-body sensor platform in a wireless body sensor network: Design and implementation. *Sensors* 12(8), pp. 10381-10394. 2012. . DOI: 10.3390/s120810381.

[27] Z. L. Wang. Self-powered nanosensors and nanosystems. *Adv Mater* 24(2), pp. 280-285. 2012. . DOI: 10.1002/adma.201102958.

[28] (16 Jul 2012). *National Ambient Air Quality Standards*. Available: <http://epa.gov/air/criteria.html>.

[29] Do Dang Trung, Nguyen Van Toan, Pham Van Tong, Nguyen Van Duy, Nguyen Duc Hoa and Nguyen Van Hieu. Synthesis of single-crystal SnO₂ nanowires for NO_x gas sensors application. *Ceram. Int.* 38(8), pp. 6557-6563. 2012. . DOI: 10.1016/j.ceramint.2012.05.039.

[30] K. Song, B. Joo, N. Choi, Y. Lee, S. Lee, J. Huh and D. Lee. A micro hot-wire sensors for gas sensing applications. *Sens. Actuator B-Chem.* 102(1), pp. 1-6. 2004. . DOI: 10.1016/j.snb.2003.11.038.

[31] Q. Tan, W. Zhang, C. Xue, J. Xiong, Y. Ma and F. Wen. Design of mini-multi-gas monitoring system based on IR absorption. *Opt. Laser Technol.* 40(5), pp. 703-710. 2008. . DOI: 10.1016/j.optlastec.2007.10.011.

[32] Z. Zhu, Y. Xu and B. Jiang. A one ppm NDIR methane gas sensor with single frequency filter denoising algorithm. *Sensors* 12(9), pp. 12729-12740. 2012. . DOI: 10.3390/s120912729.

[33] A. N. Pisarenko, W. U. Spindel, R. T. Taylor, J. D. Brown, J. A. Cox and G. E. Pacey. Detection of ozone gas using gold nanoislands and surface plasmon resonance. *Talanta* 80(2), 2009. . DOI: 10.1016/j.talanta.2009.07.062.

[34] R. A. Iglesias, F. Tsow, R. Wang, E. S. Forzani and N. Tao. Hybrid separation and detection device for analysis of benzene, toluene, ethylbenzene, and xylenes in complex samples. *Anal. Chem.* 81(21), 2009. . DOI: 10.1021/ac9015769.

- [35] M. Heim, B. J. Mullins, H. Umhauer and G. Kasper, "Performance evaluation of three optical particle counters with an efficient "multimodal" calibration method," *Journal of Aerosol Science*, vol. 39, pp. 1019-1031, 22 Jul 2008, 2008.
- [36] B. J. Mullens, D. Kampa and G. Kasper, "Comment on "Performance evaluation of 3 optical particle counters with an efficient multimodal calibration method" (Heim et al., 2008)-Performance of improved counter," *Journal of Aerosol Science*, vol. 49, pp. 48-50, 3 Feb 2012, 2012.
- [37] M. Taylor, "Data visualization and hardware for citizen science," CREATE Lab, Robotics Institute, Carnegie Mellon University, 26 Mar 2012. 2012.
- [38] National Center for Photovoltaics, "Best research-cell efficiencies," NREL, US Department of Energy, 23 Jun 2013. 2013.
- [39] V. Sabnis, H. Yuen and M. Wiemer. High-efficiency multijunction solar cells employing dilute nitrides. *8th International Conference on Concentrating Photovoltaic Systems (Cpv-8) 1477* pp. 14-19. 2012. . DOI: 10.1063/1.4753823.
- [40] LG Electronics, "Mono X LG265S1C-G3/LG260S1C-G3/LG255S1C-G3," May 2013, 2013.
- [41] Cymbet Corporation, "CBC-PV-01 Photovoltaic Cell," 2012.
- [42] J. R. Szczech, J. M. Higgins and S. Jin. Enhancement of the thermoelectric properties in nanoscale and nanostructured materials. *J. Mater. Chem. 21(12)*, pp. 4037-4055. 2011. . DOI: 10.1039/c0jm02755c.
- [43] K. Biswas, J. He, I. D. Blum, C. Wu, T. P. Hogan, D. N. Seidman, V. P. Dravid and M. G. Kanatzidis. High-performance bulk thermoelectrics with all-scale hierarchical architectures. *Nature 489(7416)*, pp. 414-418. 2012. . DOI: 10.1038/nature11439.
- [44] H. Wang, W. D. Porter, H. Boettner, J. Koenig, L. Chen, S. Bai, T. M. Tritt, A. Mayolet, J. Senawiratne, C. Smith, F. Harris, P. Gilbert, J. W. Sharp, J. Lo, H. Kleinke and L. Kiss. Transport properties of bulk thermoelectrics-an international round-robin study, part I: Seebeck coefficient and electrical resistivity. *J Electron Mater 42(4)*, pp. 654-664. 2013. . DOI: 10.1007/s11664-012-2396-8.
- [45] I. Chowdhury, R. Prasher, K. Lofgreen, G. Chrysler, S. Narasimhan, R. Mahajan, D. Koester, R. Alley and R. Venkatasubramanian. On-chip cooling by superlattice-based thin-film thermoelectrics. *Nat. Nanotechnol. 4(4)*, pp. 235-238. 2009. . DOI: 10.1038/NNANO.2008.417.

- [46] B. Bitnar, W. Durisch and R. Holzner. Thermophotovoltaics on the move to applications. *Appl. Energy* 105pp. 430-438. 2013. . DOI: 10.1016/j.apenergy.2012.12.067.
- [47] P. Yaghoobi, M. V. Moghaddam and A. Nojeh. Solar electron source and thermionic solar cell. *AIP Adv.* 2(4), pp. 042139. 2012. . DOI: 10.1063/1.4766942.
- [48] F. Ongaro, S. Saggini and P. Mattavelli. Li-ion battery-supercapacitor hybrid storage system for a long lifetime, photovoltaic-based wireless sensor network. *IEEE Trans. Power Electron.* 27(9), pp. 3944-3952. 2012. . DOI: 10.1109/TPEL.2012.2189022.
- [49] Cymbet Corporation, "CBC-EVAL-09, EnerChip EP Universal Energy Harvester Eval Kit Datasheet," 3 Jul 2013, 2013.
- [50] Anonymous *Battery Management Systems Electronic Resource* : *Accurate State-of-Charge Indication for Battery Powered Applications* 2008 Available: <http://www2.lib.ncsu.edu/catalog/record/NCSU2372320>; Get an online version (NCSU only) (<http://proxying.lib.ncsu.edu/index.php?url=http://link.springer.com/openurl?genre=book&isbn=978-1-4020-6944-4>).
- [51] R. C. de Guzman, J. Yang, M. Ming-Cheng, S. O. Salley and K. Y. S. Ng. A silicon nanoparticle/reduced graphene oxide composite anode with excellent nanoparticle dispersion to improve lithium ion battery performance. *J. Mater. Sci.* 48(14), pp. 4823-4833. 2013. . DOI: 10.1007/s10853-012-7094-7.
- [52] S. Lee, C. S. Yoon, K. Amine and Y. Sun. Improvement of long-term cycling performance of $\text{Li}[\text{Ni}_{0.8}\text{Co}_{0.15}\text{Al}_{0.05}]\text{O}_2$ by AlF_3 coating. *J. Power Sources* 234pp. 201-207. 2013. . DOI: 10.1016/j.jpowsour.2013.01.045.
- [53] J. Xiang, F. Wu, R. Chen, L. Li and H. Yu. High voltage and safe electrolytes based on ionic liquid and sulfone for lithium-ion batteries. *J. Power Sources* 233pp. 115-120. 2013. . DOI: 10.1016/j.jpowsour.2013.01.123.
- [54] S. S. Zhang. Liquid electrolyte lithium/sulfur battery: Fundamental chemistry, problems, and solutions. *J. Power Sources* 231pp. 153-162. 2013. . DOI: 10.1016/j.jpowsour.2012.12.102.
- [55] W. A. v. Schalkwijk and B. Scrosati. *Advances in Lithium-Ion Batteries* 2002 Available: <http://search.ebscohost.com/login.aspx?direct=true&db=nlebk&AN=78412&site=ehost-live>.
- [56] Maxwell Technologies, "HC Series Ultracapacitors - Datasheet," .

[57] H. Jin, X. Wang, Z. Gu and J. Polin. Carbon materials from high ash biochar for supercapacitor and improvement of capacitance with HNO₃ surface oxidation. *J. Power Sources* 236pp. 285-292. 2013. . DOI: 10.1016/j.jpowsour.2013.02.088.

[58] M. T. Penella-López. *Powering Autonomous Sensors Electronic Resource] : An Integral Approach with Focus on Solar and RF Energy Harvesting* 2011 Available: <http://www2.lib.ncsu.edu/catalog/record/NCSU2496380>; Get an online version (Duke only) (http://proxy.lib.duke.edu/login?url=http://getitduke.library.duke.edu/?sid=sersol&SS_jc=TC0000508599&title=Powering%20Autonomous%20Sensors%3A%20An%20Integral%20Approach%20with%20Focus%20on%20Solar%20and%20RF%20Energy%20Harvesting); Get an online version (NCSU only) (<http://proxying.lib.ncsu.edu/index.php?url=http://link.springer.com/openurl?genre=book&isbn=978-94-007-1572-1>).

[59] P. Simon and Y. Gogotsi. Capacitive energy storage in nanostructured carbon-electrolyte systems. *Acc. Chem. Res.* 46(5), pp. 1094-1103. 2013. . DOI: 10.1021/ar200306b.

[60] M. S. W. Chan, K. T. Chau and C. C. Chan, "Effective Charging Method for Ultracapacitors," *Journal of Asian Electric Vehicles*, vol. 3, pp. 771-776, Dec 2005, 2005.

[61] Texas Instruments, "eZ430-RF2500-SEH Solar Energy Harvesting Development Tool User's Guide," July 2013, 2013.

[62] Texas Instruments, "eZ430-RF2500 Development Tool User's Guide," April 2009, 2009.

[63] G. M. Masters, *Renewable and Efficient Electric Power Systems*. Hoboken, NJ: John Wiley & Sons, Inc., 2004.

[64] T. W. Murphy Jr. Maximum spectral luminous efficacy of white light. *J. Appl. Phys.* 111(10), pp. 104909. 2012. . DOI: 10.1063/1.4721897.

APPENDIX

Appendix A – End Device Source Code

```
//*****  
// THIS PROGRAM IS PROVIDED "AS IS". TI MAKES NO WARRANTIES OR  
// REPRESENTATIONS, EITHER EXPRESS, IMPLIED OR STATUTORY,  
// INCLUDING ANY IMPLIED WARRANTIES OF MERCHANTABILITY, FITNESS  
// FOR A PARTICULAR PURPOSE, LACK OF VIRUSES, ACCURACY OR  
// COMPLETENESS OF RESPONSES, RESULTS AND LACK OF NEGLIGENCE.  
// TI DISCLAIMS ANY WARRANTY OF TITLE, QUIET ENJOYMENT, QUIET  
// POSSESSION, AND NON-INFRINGEMENT OF ANY THIRD PARTY  
// INTELLECTUAL PROPERTY RIGHTS WITH REGARD TO THE PROGRAM OR  
// YOUR USE OF THE PROGRAM.  
//  
// IN NO EVENT SHALL TI BE LIABLE FOR ANY SPECIAL, INCIDENTAL,  
// CONSEQUENTIAL OR INDIRECT DAMAGES, HOWEVER CAUSED, ON ANY  
// THEORY OF LIABILITY AND WHETHER OR NOT TI HAS BEEN ADVISED  
// OF THE POSSIBILITY OF SUCH DAMAGES, ARISING IN ANY WAY OUT  
// OF THIS AGREEMENT, THE PROGRAM, OR YOUR USE OF THE PROGRAM.  
// EXCLUDED DAMAGES INCLUDE, BUT ARE NOT LIMITED TO, COST OF  
// REMOVAL OR REINSTALLATION, COMPUTER TIME, LABOR COSTS, LOSS  
// OF GOODWILL, LOSS OF PROFITS, LOSS OF SAVINGS, OR LOSS OF  
// USE OR INTERRUPTION OF BUSINESS. IN NO EVENT WILL TI'S  
// AGGREGATE LIABILITY UNDER THIS AGREEMENT OR ARISING OUT OF  
// YOUR USE OF THE PROGRAM EXCEED FIVE HUNDRED DOLLARS  
// (U.S.$500).k  
//  
// Unless otherwise stated, the Program written and copyrighted  
// by Texas Instruments is distributed as "freeware". You may,  
// only under TI's copyright in the Program, use and modify the  
// Program without any charge or restriction. You may  
// distribute to third parties, provided that you transfer a  
// copy of this license to the third party and the third party  
// agrees to these terms by its first use of the Program. You  
// must reproduce the copyright notice and any other legend of  
// ownership on each copy or partial copy, of the Program.  
//  
// You acknowledge and agree that the Program contains  
// copyrighted material, trade secrets and other TI proprietary  
// information and is protected by copyright laws,  
// international copyright treaties, and trade secret laws, as  
// well as other intellectual property laws. To protect TI's  
// rights in the Program, you agree not to decompile, reverse  
// engineer, disassemble or otherwise translate any object code  
// versions of the Program to a human-readable form. You agree  
// that in no event will you alter, remove or destroy any  
// copyright notice included in the Program. TI reserves all  
// rights not specifically granted under this license. Except  
// as specifically provided herein, nothing in this agreement  
// shall be construed as conferring by implication, estoppel,
```

```

// or otherwise, upon you, any license or other right under any
// TI patents, copyrights or trade secrets.
//
// You may not use the Program in non-TI devices.
//
//*****
// eZ430-RF2500 Temperature Sensor End Device using Cymbet Solar Energy
// Harvesting Board
//
// Description:
//     This is the End Device software for the eZ430-RF2500-SEH Temperature
//     Sensing demo when hooked up to a Cymbet solar Energy Harvester board.
//
//     The Energy Harvester End Device (EHED) will join the traditional
//     Access Point (AP). The EHED was optimized to reduce active time
//     especially during start up.
//
// W. Goh
// Version 1.5
// Texas Instruments, Inc
// March 2009
// Built with IAR Embedded Workbench Version: 4.11B
// Built with Code Composer Essentials Version: 3.1 build 3.2.3.6.4
//*****
// Change Log:
//*****
// Version: 1.5 using SimpliciTI ver 1.06
// Comments: Fixed an un-initialized bug inside SimpliciTI
//           Removed unnecessary port initialization in code
// Version: 1.4 using simpliciTI ver 1.06
// Comments: Fixed several bugs.
//           Added blinking LED on power-up
//           Application files now compiles on both IAR and CCE
// Version: 1.3 using Simpliciti ver 1.06
// Comments: Added count battery used count fields
//           Added number_transmits_on_battery counts up and down
//           Added check if battery charged for 1 hour
// Version: 1.0
// Comments: Initial Release date
//*****

#include "bsp.h"
#include "mrfi.h"
#include "bsp_leds.h"
#include "bsp_buttons.h"
#include "nwk_types.h"
#include "nwk_api.h"
#include "nwk_frame.h"
#include "nwk.h"

#include "msp430x22x4.h"

```

```

#include "vlo_rand.h"

#define WakeupPeriod      15000           // ~10 sec (=15000/(12000/8))
#define a_d_wakeup_time  4500            // ~3 sec
#define TXPeriod          7500           // ~5 sec (=7500/(12000/8))
#define delay_time        500            // led delay time
#define debounce_time     750            // key debounce

//Timer count for time between transmit
#define sec1               1500           // ~1 sec
#define sec2               2610
#define sec5               7500           // ~5 sec (=7500/(12000/8))
#define sec10              15000          // ~10 sec
#define sec20              30000          // ~20 swec
#define sec40              60000          // ~40 sec
#define sec30_2            43000          // ~30sec 2 min?
#define sec30_4            50434          // ~30sec 4 min?
#define one_hour           5400000

#define port_delay         10             // 6ms - 1.5 msec

#define status_one         1
#define status_two         2
#define status_three       3
#define status_four        4
#define status_five        5
#define status_six         6

#define timer_state_1      1
#define timer_state_2      2
#define timer_state_3      3
#define timer_state_4      4
#define timer_state_5      5
#define timer_state_6      6

#define run_voltage        29             // Minimum voltage to execute 2.9V
#define ad_check_voltage   29
#define key_down_count     12            // # times to check if button is
// still button pressed

#define battery_time_test  174           // 3 min count at 10 sec for testing
#define running_on_battery 100           // Tells GUI that it is running on
// battery
#define xmt_count          100           // # max transmit on battery - 400
// magic number
//
reduced to 100 due to 4x transmissions

#define ON                  1
#define OFF                  0

```

```

unsigned int timer_state;
unsigned char change_mode;
unsigned char ftt_flag;
unsigned int battery_ready = 0;
unsigned int in_delay = 0;
char status = 0;
unsigned int battery_full_flag = 0;
unsigned long battery_full_timer = 0;

unsigned int number_transmits_on_battery;

void linkTo(void);
void StatusBlink_led1(int BlinkCount);
void StatusBlink_led2(int BlinkCount);
void status_indicator(char status, int status_led);
void delay(unsigned int BlinkCount);
void button_still_pressed(void);
unsigned int get_voltage(void);
void transmit_time_delay(void);
void display_mode(void);
void check_bat_full(void);
void createRandomAddress(void);
int OneFiveVrefADC(void);

void main (void)
{
    addr_t lAddr;
    char *Flash_Addr;
    unsigned int current_voltage;

    WDTCTL = WDTPW + WDTHOLD;                // Stop WDT

    P1DIR |= 0x03;                            // Set P1.0,1 Output
    if( CALBC1_1MHZ == 0xFF && CALDCO_1MHZ == 0xFF &&
        CALBC1_8MHZ == 0xFF && CALDCO_8MHZ == 0xFF )// Do not run if cal values
    {                                          // are erased and set LEDs ON
        P1OUT |= 0x03;                       // Set P1.0,1 High
        __bis_SR_register(LPM4_bits);        // Enter LPM4 if Cal missing
    }

    // Blink LED for startup feedback
    P1OUT |= 0x03;                            // Set P1.0,1 High
    __delay_cycles(10000);
    P1OUT &= ~0x03;                           // Set P1.0,1 Low

    Flash_Addr = (char *)0x10F0;             // RF Address = 0x10F0
    if( Flash_Addr[0] == 0xFF &&
        Flash_Addr[1] == 0xFF &&
        Flash_Addr[2] == 0xFF &&
        Flash_Addr[3] == 0xFF )
    {

```

```

    createRandomAddress();           // Create Random device address at
}                                   // initial startup if missing
lAddr.addr[0] = Flash_Addr[0];
lAddr.addr[1] = Flash_Addr[1];
lAddr.addr[2] = Flash_Addr[2];
lAddr.addr[3] = Flash_Addr[3];
SMPL_Ioctl(IOCCTL_OBJ_ADDR, IOCCTL_ACT_SET, &lAddr);

BSP_Init();                         // Initialize eZ430 hardware

BCSCTL3 |= LFXT1S_2;                // LFXT1 = ACLK = VLO
TBCCTL0 = CCIE;                     // TBCCR0 interrupt enabled
TBCCR0 = WakeupPeriod;              // ~10_sec (=15000/(12000/8))
TBCTL = TBSSEL_1 + MC_1 + ID_3;    // ACLK, upmode, Divider = 8

status = status_four;               // Set status to 4

// Initialize SimpliciTI
while(SMPL_NO_JOIN == SMPL_Init((uint8_t (*)(linkID_t))0))
{
    __bis_SR_register(LPM3_bits + GIE); // LPM3 with interrupts enabled
}

// Put radio to sleep
SMPL_Ioctl( IOCCTL_OBJ_RADIO, IOCCTL_ACT_RADIO_SLEEP, "" );

ftt_flag = 1;                       // first time thru the program flag

BCSCTL1 = CALBC1_1MHZ;              // Set DCO = 1MHz
DCOCTL = CALDCO_1MHZ;

// SimpliciTI will change port pin settings as well
P1DIR = 0xFB;                       // P1.2 (button) = input
P1OUT = 0x04;                       // P1.2 pullup
P1REN |= 0x04;                      // P1.2 pullup
P1IE |= 0x04;                       // P1.3 interrupt enabled
P1IES |= 0x04;                      // P1.3 Hi/lo edge
P1IFG &= ~0x04;                    // P1.3 IFG cleared
P2DIR = 0x20;
P2REN |= 0x00;
P2OUT = 0x00;
P3DIR |= 0xD0;                      // port 3 set after initialization
P3OUT &= ~0x30;                    // set up port 3
P3REN |= 0x20;                      // Enable Pull-Down Res for /Charge
P4DIR = 0x87;                      // setup port 4 - 4.3 to 4.6 set low
P4OUT = 0x00;
P4REN = 0x00;

timer_state = timer_state_2;        // set timer state to 2 ~ 10_sec
change_mode = 10;                   // Default GUI display mode set to
// 10_sec

```

```

TBCTL |= TBCLR; // Clear TBR counter
TBCCR0 = a_d_wakeup_time; // set timer to wakeup time ~ 3 sec
// added to check if battery voltage stable before linking
current_voltage = get_voltage(); // get current battery voltage
if(current_voltage < run_voltage)
{
    current_voltage = 0;
    while (current_voltage < ad_check_voltage)
    {
        __bis_SR_register(LPM3_bits + GIE); // Enter LPM3 w/ interrupts
        current_voltage = get_voltage();
    }
}

SMPL_Ioct1( IOCTL_OBJ_RADIO, IOCTL_ACT_RADIO_AWAKE, "" );
// unconditional link to AP which is listening due to successful join.
linkTo();
}

/*****
* @fn linkTo
*****/
void linkTo(void)
{
    linkID_t linkID1;
    uint8_t chunk0[9], chunk1[9], chunk2[9], chunk3[9];
    unsigned int *tempOffset; // Initialize temperature offset
    tempOffset = (unsigned int *)0x10F4; // coefficient
    number_transmits_on_battery = xmt_count; // Initialize to max
transmit #
    int number_failed_transmits = 0; // Initialize to 0
    int saved_transmits[180]; // 25 saved messages -
36 bytes each - 900 bytes total

    // keep trying to link... Uses Timer B to wake up periodically
    while (SMPL_SUCCESS != SMPL_Link(&linkID1))
    {
        __bis_SR_register(LPM3_bits + GIE); // LPM3 with interrupts enabled
    }
    // put radio to sleep once a successfull connection has been established
    SMPL_Ioct1( IOCTL_OBJ_RADIO, IOCTL_ACT_RADIO_SLEEP, "" );

    while(1)
    {
        volatile long temp;
        int degC, volt, pin3, pin4, pin5, pin6, pin7, pin8, pin9, pin10, pin11,
pin17;

        // If battery charging, go back to sleep (if P3.5 = 1, Sleep)
        P3REN &= ~0x20; // turn off pulldown resistor

```

```

delay(port_delay);

// Measure Temperature
ADC10CTL1 = INCH_10 + ADC10DIV_4;           // Temp Sensor ADC10CLK/5
ADC10CTL0 = SREF_1 + ADC10SHT_3 + REFON + ADC10ON + ADC10IE + ADC10SR;
__delay_cycles(350);                       // delay to allow reference to settle
ADC10CTL0 |= ENC + ADC10SC;                // Sampling and conversion start
__bis_SR_register(LPM0_bits + GIE);        // LPM0 with interrupts enabled
degC = ADC10MEM;
ADC10CTL0 &= ~ENC;

// Measure Battery Voltage
ADC10CTL1 = INCH_11;                       // AVcc/2
ADC10CTL0 = SREF_1 + ADC10SHT_3 + REFON + ADC10ON + ADC10IE + REF2_5V;
__delay_cycles(350);                       // delay to allow reference to settle
ADC10CTL0 |= ENC + ADC10SC;                // Sampling and conversion start
__bis_SR_register(LPM0_bits + GIE);        // LPM0 with interrupts enabled
volt = ADC10MEM;
ADC10CTL0 &= ~ENC;

// Measure A0/Pin3 - 1.5V internal reference
ADC10AE0 = 0x01;
ADC10CTL1 = INCH_0;
pin3 = OneFiveVrefADC();
ADC10AE0 = 0x00;

// Measure A1/Pin4
ADC10AE0 = 0x02;
ADC10CTL1 = INCH_1;
pin4 = OneFiveVrefADC();
ADC10AE0 = 0x00;

// A2/Pin5
ADC10AE0 = 0x04;
ADC10CTL1 = INCH_2;
pin5 = OneFiveVrefADC();
ADC10AE0 = 0x00;

// A3/Pin6
ADC10AE0 = 0x08;
ADC10CTL1 = INCH_3;
pin6 = OneFiveVrefADC();
ADC10AE0 = 0x00;

// A4/Pin7
ADC10AE0 = 0x10;
ADC10CTL1 = INCH_4;
pin7 = OneFiveVrefADC();
ADC10AE0 = 0x00;

// A12/Pin8

```

```

ADC10AE1 = 0x10;
ADC10CTL1 = INCH_12;
pin8 = OneFiveVrefADC();
ADC10AE1 = 0x00;

// A13/Pin9
ADC10AE1 = 0x20;
ADC10CTL1 = INCH_13;
pin9 = OneFiveVrefADC();
ADC10AE1 = 0x00;

// A14/Pin10
ADC10AE1 = 0x40;
ADC10CTL1 = INCH_14;
pin10 = OneFiveVrefADC();
ADC10AE1 = 0x00;

// A15/Pin11
ADC10AE1 = 0x80;
ADC10CTL1 = INCH_15;
pin11 = OneFiveVrefADC();
ADC10AE1 = 0x00;

// A5/Pin17
ADC10AE0 = 0x20;
ADC10CTL1 = INCH_5;
pin17 = OneFiveVrefADC();
ADC10AE0 = 0x00;

ADC10CTL0 &= ~(REFON + ADC10ON);           // turn off A/D to save power

// prep temperature result
// oC = ((A10/1024)*1500mV)-986mV)*1/3.55mV = A10*423/1024 - 278
// the temperature is transmitted as an integer where 32.1 = 321
// hence 4230 instead of 423
temp = degC;
degC = ((temp - 673) * 4230) / 1024;
if( *tempOffset != 0xFFFF )
{
    degC += *tempOffset;
}

// prep voltage result
temp = volt;
volt = (temp*25)/512; // 1.25V * 10 * 2 / 1024

/* chunk message format - 9 payload bytes per chunk - can transmit 10
 * chunk0
 * -----
-----

```

```

    * | Chunk # | MisX# LB | MisX# UB | S/B Mode | BatX# LB | BatX# UB | volt
    | degC LB | degC UB |
    * -----
    -----
    *
    * chunk1
    * -----
    -----
    * | Chunk # | pin3 LB | pin3 UB | pin4 LB | pin4 UB | pin5 LB | pin5
    UB | pin6 LB | pin6 UB |
    * -----
    -----
    *
    * chunk2
    * -----
    -----
    * | Chunk # | pin7 UB | pin7 LB | pin8 LB | pin8 UB | pin9 LB | pin9
    UB | pin10 LB | pin10 UB |
    * -----
    -----
    *
    * chunk3
    * -----
    -----
    * | Chunk # | pin11 LB | pin11 UB | pin17 LB | pin17 UB |
    * -----
    -----
    */

// Prepare chunk0 for transmission
chunk0[0] = 0x00;

// PH for the management code re lost transmissions
chunk0[1] = number_failed_transmits&0xFF;
chunk0[2] = (number_failed_transmits>>8)&0xFF;

// If using Solar & not first time through, set battery as ready
if(((P3IN & 0x20) == 0x00) && (ftt_flag == 0) && (battery_ready == 0))
{
    battery_ready = 1;
}

// If battery is ready or first time through, transmit packets
if(battery_ready == 1 || ftt_flag == 1)
{
    if((P3IN & 0x20)) // If P3.5 = 1, then
    { // running on battery
        chunk0[3] = (change_mode + running_on_battery); // +100 is for GUI to
know // is on battery
        if( number_transmits_on_battery != 0)

```

```

        number_transmits_on_battery--;           // # transmit countdown
    }
    else
    {
        // else using solar cells
        chunk0[3] = change_mode;
        if(number_transmits_on_battery != xmt_count)
        {
            number_transmits_on_battery++;
            if(number_transmits_on_battery >= xmt_count) // If max # of transmits
achieved,
            {
                // Reset counter to 400.
                number_transmits_on_battery = xmt_count;
            }
        }
        if(battery_full_flag == 1) // If battery is fully charged,
        {
            // reset counter to 400
            number_transmits_on_battery = xmt_count;
        }
    }
    chunk0[4] = number_transmits_on_battery&0xFF;
    chunk0[5] = (number_transmits_on_battery>>8)&0xFF;

    // if end of battery, turn off battery
    if(number_transmits_on_battery == 0)
    {
        in_delay = 1;
        while((P3IN & 0x20)) // Continue sleeping if still on
        {
            // battery
            __bis_SR_register(LPM4_bits);
        }
        in_delay = 0;
    }

    chunk0[6] = volt;
    chunk0[7] = degC&0xFF;
    chunk0[8] = (degC>>8)&0xFF;

    // Prepare chunks 1 - 3 for transmission
    chunk1[0] = 0x01;
    chunk2[0] = 0x02;
    chunk3[0] = 0x03;

    // Package the Analog Inputs
    chunk1[1] = pin3&0xFF;
    chunk1[2] = (pin3>>8)&0xFF;
    chunk1[3] = pin4&0xFF;
    chunk1[4] = (pin4>>8)&0xFF;
    chunk1[5] = pin5&0xFF;
    chunk1[6] = (pin5>>8)&0xFF;
    chunk1[7] = pin6&0xFF;
    chunk1[8] = (pin6>>8)&0xFF;

```

```

chunk2[1] = pin7&0xFF;
chunk2[2] = (pin7>>8)&0xFF;
chunk2[3] = pin8&0xFF;
chunk2[4] = (pin8>>8)&0xFF;
chunk2[5] = pin9&0xFF;
chunk2[6] = (pin9>>8)&0xFF;
chunk2[7] = pin10&0xFF;
chunk2[8] = (pin10>>8)&0xFF;
chunk3[1] = pin11&0xFF;
chunk3[2] = (pin11>>8)&0xFF;
chunk3[3] = pin17&0xFF;
chunk3[4] = (pin17>>8)&0xFF;

// Wake radio-up
SMPL_Ioctl( IOCTL_OBJ_RADIO, IOCTL_ACT_RADIO_AWAKE, "" );

// Send chunks
if (SMPL_SUCCESS == nwk_ping(linkID1))
{
    delay(port_delay);

    SMPL_Send(linkID1, chunk0, sizeof(chunk0));
    delay(port_delay);
    SMPL_Send(linkID1, chunk1, sizeof(chunk1));
    delay(port_delay);
    SMPL_Send(linkID1, chunk2, sizeof(chunk2));
    delay(port_delay);
    SMPL_Send(linkID1, chunk3, sizeof(chunk3));
    delay(port_delay);

    // send saved chunks here
    while (number_failed_transmits>0)
    {
        int i;
        for (i=0; i < 9; i++)
        {
            chunk0[i] = saved_transmits[(36*(number_failed_transmits-
1))+i];
            chunk1[i] = saved_transmits[(36*(number_failed_transmits-
1))+9+i];
            chunk2[i] = saved_transmits[(36*(number_failed_transmits-
1))+18+i];
            chunk3[i] = saved_transmits[(36*(number_failed_transmits-
1))+27+i];
        }

        delay(port_delay);

        SMPL_Send(linkID1, chunk0, sizeof(chunk0));
        delay(port_delay);
        SMPL_Send(linkID1, chunk1, sizeof(chunk1));

```

```

        delay(port_delay);
        SMPL_Send(linkID1, chunk2, sizeof(chunk2));
        delay(port_delay);
        SMPL_Send(linkID1, chunk3, sizeof(chunk3));
        delay(port_delay);

        number_failed_transmits--;
    }

    if(P3IN & 0x20) // Using Battery, Blink Red
    {
        status_indicator(status_one, 1);
    }
    else // Using Solar & Blink Green
    {
        status_indicator(status_one, 2);
    }
}
else // Blink both LED if transmission
// failed
{
    status_indicator(status_one, 1);
    status_indicator(status_one, 2);

    // save chunks here
    if (number_failed_transmits < ((sizeof(saved_transmits))/36)) // Don't
exceed array size
    {
        int i;
        for (i=0; i < 9; i++)
        {
            saved_transmits[(36*number_failed_transmits)+i] =
chunk0[i];
            saved_transmits[(36*number_failed_transmits)+9+i] =
chunk1[i];
            saved_transmits[(36*number_failed_transmits)+18+i] =
chunk2[i];
            saved_transmits[(36*number_failed_transmits)+27+i] =
chunk3[i];
        }
    }
    number_failed_transmits++;
}
}

ftt_flag = 0; // first time thru the program flag
check_bat_full();
status = status_six;
P3REN |= 0x20; // Set /Charge pulldown resistor
SMPL_Ioctl( IOCTL_OBJ_RADIO, IOCTL_ACT_RADIO_SLEEP, "" );
transmit_time_delay(); // sleep time between transmits

```

```

}
}

/*****
* BEGHDR
*
* NAME:createRandomAddress()
*
* DESCRIPTION: generate random address
*****/
void createRandomAddress()
{
    unsigned int rand, rand2;
    char *Flash_Addr;
    Flash_Addr = (char *)0x10F0;

    do
    {
        rand = TI_getRandomIntegerFromVLO();    // first byte can not be 0x00 of 0xFF
    }
    while( (rand & 0xFF00)==0xFF00 || (rand & 0xFF00)==0x0000 );
    rand2 = TI_getRandomIntegerFromVLO();

    BCSCTL1 = CALBC1_1MHZ;                // Set DCO to 1MHz
    DCOCTL = CALDCO_1MHZ;
    FCTL2 = FWKEY + FSSEL0 + FN1;         // MCLK/3 for Flash Timing Generator
    FCTL3 = FWKEY + LOCKA;                // Clear LOCK & LOCKA bits
    FCTL1 = FWKEY + WRT;                  // Set WRT bit for write operation

    Flash_Addr[0]=(rand>>8) & 0xFF;
    Flash_Addr[1]=rand & 0xFF;
    Flash_Addr[2]=(rand2>>8) & 0xFF;
    Flash_Addr[3]=rand2 & 0xFF;

    FCTL1 = FWKEY;                        // Clear WRT bit
    FCTL3 = FWKEY + LOCKA + LOCK;         // Set LOCK & LOCKA bit
}

/*****
* BEGHDR
* Function:    void StatusBlink_led1(int BlinkCount)
* DESCRIPTION: Blinks LED 1 - Red based on specified delay
* INPUTS:     BlinkCount
* PROCESSING: Turns on and off the RED LED with specified blink time
* OUTPUTS:    VOID
*****/
void StatusBlink_led1(int BlinkCount)
{
    BSP_TURN_ON_LED1();
    delay(BlinkCount);
    BSP_TURN_OFF_LED1();
}

```

```

}

/*****
* BEGHDR
* Function: void StatusBlink_led1(int BlinkCount)
* DESCRIPTION: Blinks LED 1 - Green based on specified delay
* INPUTS: BlinkCount
* PROCESSING: Turns on and off the Green LED with specified blink time
* OUTPUTS: VOID
*****/
void StatusBlink_led2(int BlinkCount)
{
    BSP_TURN_ON_LED2();
    delay(BlinkCount);
    BSP_TURN_OFF_LED2();
}

/*****
* BEGHDR
* Function: void delay(unsigned int BlinkCount)
* DESCRIPTION: Creates a low-power delay by entering LPM3 using Timer B.
* Timer B frequency = VLO/8 = 1500 Hz.
* INPUTS: BlinkCount
* PROCESSING: Delay length of time of BlinkCount
* OUTPUTS: VOID
*****/
void delay(unsigned int BlinkCount)
{
    int TimerTemp;
    TimerTemp = TBCCR0; // Save current content of TBCCR0
    TBCCR0 = BlinkCount; // Set new TBCCR0 delay
    TBCTL |= TBCLR; // Clear TBR counter
    TBCCTL0 &= ~CCIFG; // Clear CCIFG Flag
    TBCTL |= MC_1; // Start Timer B
    __bis_SR_register(LPM3_bits + GIE); // Enter LPM3
    TBCTL &= ~(MC_1); // Stop Timer B
    TBCCR0 = TimerTemp;
}

/*****
* BEGHDR
* Function: void status_indicator(char status , int status_led)
* DESCRIPTION: This can be usefull to blink the LED to indicate where the
* program is executing for debugging purposes. It blinks the red or
* green LED the number of times in status. For example, status_five
* blinks the LED 5 times.
* INPUTS: status, status_led
* PROCESSING: Blinks the red or green led the number of times in status and the
* correct led in status_led
* OUTPUTS: VOID
*****/

```

```

void status_indicator(char status , int status_led)
{
    volatile unsigned int i = 0;
    switch (status)
    {
        case status_one:
            if (status_led == 1)
                StatusBlink_led1(15);
            if (status_led == 2)
                StatusBlink_led2(15);
            break;

        case status_two:
            if (status_led == 1)
            {
                StatusBlink_led1(15);
                delay(delay_time);
                StatusBlink_led1(15);
            }
            if (status_led==2)
            {
                StatusBlink_led2(15);
                delay(delay_time);
                StatusBlink_led2(15);
            }
            break;

        case status_three:
            if(status_led == 1)
            {
                for(i=0 ; i < (status-1) ; i++)
                {
                    StatusBlink_led1(15);
                    delay(delay_time);
                }
                StatusBlink_led1(15);
            }
            if(status_led == 2)
            {
                for(i=0 ; i < (status-1) ; i++)
                {
                    StatusBlink_led2(15);
                    delay(delay_time);
                }
                StatusBlink_led2(15);
            }
            break;

        case status_four:
            if(status_led == 1)
            {

```

```

        for(i=0 ; i < (status-1) ; i++)
        {
            StatusBlink_led1(15);
            delay(delay_time);
        }
        StatusBlink_led1(15);
    }
    if(status_led == 2)
    {
        for(i=0 ; i < (status-1) ; i++)
        {
            StatusBlink_led2(15);
            delay(delay_time);
        }
        StatusBlink_led2(15);
    }
    break;

case status_five:
    if(status_led == 1)
    {
        for(i=0 ; i < (status-1) ; i++)
        {
            StatusBlink_led1(15);
            delay(delay_time);
        }
        StatusBlink_led1(15);
    }
    if(status_led == 2)
    {
        for(i=0 ; i < (status-1) ; i++)
        {
            StatusBlink_led2(15);
            delay(delay_time);
        }
        StatusBlink_led2(15);
    }
    break;
default:
    break;
}
}

/*****
* BEGHDR
* Function:    unsigned int get_voltage(void)
* DESCRIPTION: Get battery voltage with A/D
* INPUTS:     void
* PROCESSING:  Read battery voltage from ADC10 and returns the value
* OUTPUTS:    Battery voltage from A/D
*****/

```

```

unsigned int get_voltage(void)
{
    unsigned int rt_volts;

    ADC10CTL1 = INCH_11;                // AVcc/2
    ADC10CTL0 = SREF_1 + ADC10SHT_2 + REFON + ADC10ON + ADC10IE + REF2_5V;
    __delay_cycles(250);                // delay to allow reference to settle
    ADC10CTL0 |= ENC + ADC10SC;         // Sampling and conversion start
    __bis_SR_register(LPM0_bits + GIE); // LPM0 with interrupts enabled
    rt_volts = ADC10MEM;
    ADC10CTL0 &= ~ENC;
    ADC10CTL0 &= ~(REFON + ADC10ON);    // turn off A/D to save power
    rt_volts = (rt_volts*25)/512;
    return (rt_volts);
}

/*****
* BEGHDR
* NAME:      void transmit_time_delay(void)
* DESCRIPTION: Sets timer to transmit time based on timer_state
* INPUTS:    void
* PROCESSING: Sets timer to transmit time, for 2 min and 4 min transmit times
*            loop number of 30 sec times to make 2 min and 4 min.
* OUTPUTS:   void
*****/
void transmit_time_delay(void)
{
    volatile unsigned int i = 0;
    in_delay = 1;
    switch (timer_state)
    {
        case timer_state_1:                // Timer State == 1; 5 Secs
            delay(sec5);
            in_delay = 0;
            battery_full_timer += sec5;
            break;
        case timer_state_2:                // Timer State == 2; 10 Secs
            delay(sec10);
            in_delay = 0;
            battery_full_timer += sec10;
            break;

        case timer_state_3:                // Timer State == 3; 20 Secs
            delay(sec20);
            in_delay = 0;
            battery_full_timer += sec20;
            break;

        case timer_state_4:                // Timer State == 4; 40 Secs
            delay(sec40);
            in_delay = 0;
    }
}

```

```

    battery_full_timer += sec40;
    break;

case timer_state_5:                // Timer State == 5; 2 mins
    while((i++ < 4) && (timer_state == timer_state_5))
    {
        delay(sec30_2);
        in_delay = 0;
        battery_full_timer += sec30_2;
    }
    break;

case timer_state_6:                // Timer State == 6; 4 mins
    while((i++ < 8) && (timer_state == timer_state_6))
    {
        delay(sec30_4);
        in_delay = 0;
        battery_full_timer += sec30_4;
    }
    break;
default:
    break;
}
} // void transmit_time_delay(void)

/*****
* BEGHDR
* NAME:          void display_mode(void)
* DESCRIPTION:  Sets mode time to be displayed on the GUI in the voltage stage
*               for the first display
* INPUTS:       void
* PROCESSING:   Sets change_mode number based on timer_state
* OUTPUTS:      void
*****/
void display_mode(void)
{
    switch(timer_state)
    {
        case timer_state_1:
            change_mode=5;                //~=5 sec
            break;
        case timer_state_2:
            change_mode=10;               //~=10 sec
            break;
        case timer_state_3:
            change_mode=20;               //~=20 sec
            break;
        case timer_state_4:
            change_mode=40;               //~=40 sec
            break;
        case timer_state_5:

```

```

        change_mode=2;                //~=2 min
        break;
    case timer_state_6:
        change_mode=4;                //~=4 min
        break;
    default:
        break;
}
}

/*****
* BEGHDR
* NAME:      void check_batt_full(void)
* DESCRIPTION: Check if the battery has been charging for 1 hour using
*              battery_full_timer as the counter. battery_full_timer is updated
*              after each delay inside transmit_time_delay() function.
* INPUTS:    void
* PROCESSING: If battery_full_timer has arrived, switch off batteries.
*              battery_full_flag set if charging time is matched.
* OUTPUTS:   void
*****/
void check_bat_full(void)
{
    // If /Charge is high, No Solar, turn on battery
    if(P3IN & 0x20)                // /Charge=1; battery, Blink Red
    {
        P3OUT &= ~0x10;            // turn on battery
        battery_full_flag = 0;
        battery_full_timer = 0;
    }
    else                            // /Charge=0; Solar charging,
    {                                // blink green
        if(battery_full_timer >= one_hour) // If battery has been charging for
        {                            // an hour, turn off battery
            battery_full_flag = 1;
            battery_full_timer = 0;
            P3OUT |= 0x10;          // turn off battery
        }
    }
}

/*****
*BEGHDR
*NAME:      __interrupt void ADC10_ISR(void)
*DESCRIPTION: ADC10 interrupt service routine
*INPUTS:    void
*PROCESSING: Exit from LPM after interrupt
*OUTPUTS:   void
*****/
#pragma vector=ADC10_VECTOR
__interrupt void ADC10_ISR(void)

```

```

{
__bic_SR_register_on_exit(LPM0_bits);    // Clear CPUOFF bit from 0(SR)
}

/*****
* BEGHDR
* NAME:      __interrupt void Timer_B (void)
* DESCRIPTION: Timer B0 interrupt service routine
* INPUTS:    Void
* PROCESSING: Exit from LPM after interrupt
* OUTPUTS:   Void
*****/
#pragma vector=TIMERB0_VECTOR
__interrupt void TimerB_ISR (void)
{
__bic_SR_register_on_exit(LPM3_bits);    // Clear LPM3 bit from 0(SR)
}

/*****
* BEGHDR
* NAME:      __interrupt void Port_1(void)
* DESCRIPTION: Port 1 interrupt service routine function key
* INPUTS:    void
* PROCESSING: process the push button to switch to the next time mode
* OUTPUTS:   void
*****/
#pragma vector=PORT1_VECTOR
__interrupt void Port_1(void)
{
    if((P3IN & 0x20))                // /Charge=1; battery, Blink Red
    {
        BSP_TURN_ON_LED1();
        __delay_cycles(10000);
        BSP_TURN_OFF_LED1();
    }
    else                               // /Charge=0; Solar, blink green
    {
        BSP_TURN_ON_LED2();
        __delay_cycles(10000);
        BSP_TURN_OFF_LED2();
    }

    // If successful link, change timer state.
    if(status == status_six || status == status_five)
    {
        if(timer_state >= timer_state_6)    // If transmit time is == 6,
        {                                     // Set timer_state = 1
            timer_state = timer_state_1;
            display_mode();                   // Change GUI display time
        }
        else

```

```

    {
        timer_state++;                // Change transmit time state
        display_mode();                // Change GUI display time
    }
    if(in_delay)                       // If in transmit delay, exit and
    {                                   // send a new packet with new time
        __bic_SR_register_on_exit(LPM4_bits); // Clear LPM3 bit from 0(SR)
    }
}
__delay_cycles(150000);                // Debounce software delay
while(!(P1IN & 0x04));                // Loop if button is still pressed
P1IFG &= ~0x04;                        // P1.2 IFG cleared key interrupt
}

/*****
* NAME:
* DESCRIPTION:
* INPUTS:
* PROCESSING:
* OUTPUTS:
*****/
int OneFiveVrefADC(void)
{
    int value;
    ADC10CTL0 = SREF_1 + ADC10SHT_3 + REFON + ADC10ON + ADC10IE + ADC10SR;
    __delay_cycles(350);                // room to improve here - for multiple
conversions w/o turning off the 1.5V ref, this is unnecessary
    ADC10CTL0 |= ENC + ADC10SC;
    __bis_SR_register(LPM0_bits + GIE);
    value = ADC10MEM;
    ADC10CTL0 &= ~ENC;
    return value;
}

```